Master Dissertation

Investigation of molecular conductors, the magneto-caloric effect and the binary alloy $\mathbf{FeSe}_{1-x}$

Keywords: Molecular Conductors, Magneto-caloric Effect, Superconductivity

M. Sc. Candidate: Lucas Cesar Gomes Squillante
Prof. Dr. Valdeci Pereira Mariano de Souza (Advisor)

Departamento de Física do Instituto de Geociências e Ciências Exatas da Universidade Estadual Paulista "Júlio de Mesquita Filho"
Câmpus de Rio Claro

Lucas Cesar Gomes Squillante

Investigation of molecular conductors, the magneto-caloric effect and the binary alloy $FeSe_{1-x}$

Orientador: Prof. Dr. Mariano de Souza

Dissertação de Mestrado apresentada ao Instituto de Geociências e Ciências Exatas da Universidade Estadual Paulista " Júlio de Mesquita Filho" - Campus de Rio Claro, para obtenção do título de Mestre em Física.

Rio Claro
2018

537.5 Squillante, Lucas Cesar Gomes
S773i Investigation of molecular conductors, the magneto-caloric effect / Lucas Cesar Gomes Squillante. - Rio Claro, 2018
76 f. : il., figs., gráfs., tabs., fots.

Dissertação (mestrado) - Universidade Estadual Paulista, Instituto de Geociências e Ciências Exatas
Orientador: Valdeci Pereira Mariano de Souza

1. Eletrônica. 2. Correlação eletrônica. 3. Molecular conductors. 4. Magneto-caloric effect. 5. Superconductivy. I. Título.

Ficha Catalográfica elaborada pela STATI - Biblioteca da UNESP
Campus de Rio Claro/SP - Adriana Ap. Puerta Buzzá / CRB 8/7987

Lucas Cesar Gomes Squillante

Investigation of molecular conductors, the magneto-caloric effect and the binary alloy $FeSe_{1-x}$

Dissertação de Mestrado apresentada ao Instituto de Geociências e Ciências Exatas da Universidade Estadual Paulista " Júlio de Mesquita Filho" - Campus de Rio Claro, para obtenção do título de Mestre em Física.

Comissão Examinadora

Prof. Dr. Mariano de Souza (orientador)
IGCE/UNESP - Rio Claro, SP

Prof. Dr. Ricardo Paupitz B. dos Santos
IGCE/UNESP - Rio Claro, SP

Prof. Dr. Lúcio Campos Costa
UFABC - Santo André, SP

APROVADO

Rio Claro, SP, 24 de Novembro de 2017.

Abstract

The phenomenon of superconductivity is currently one of the most relevant topics in Solid State Physics, making strongly correlated systems a very high-attractive topic due to the possibility of studying the fundamental aspects of the electron-electron interaction that are the core of superconductivity. Thus, the class of molecular conductors $(TMTTF)_2X$ (where TMTTF is tetramethyltetrathiafuvalene and X is a counter-anion) plays a systematic and fundamental role to study such correlation aspects. In this Master Thesis, the materials of interest were the $(TMTTF)_2PF_6$-H_{12} and $(TMTTF)_2PF_6$-D_{12}, where a different dielectric anomaly at the Mott-Hubbard ferroelectric transition was observed for the two salts and the relaxor behavior of the hydrogenated variant was analysed based on the mean-field theory. A review of classical and quantum phase transitions was performed aiming to study the so-called magneto-caloric effect (the magnetic Grüneisen parameter) for the Brillouin paramagnet model, which is a powerful and unique physical quantity to experimentally detect a quantum phase transition induced by magnetic field in a real system. Also, a comparative study between the δ (hexagonal) and δ' (tetragonal) phases of the binary alloy $FeSe_{1-x}$ was performed and single-crystals were synthesized employing the solid-state reaction method in order to achieve the δ phase.

Resumo

O fenômeno da supercondutividade é atualmente um dos mais relevantes tópicos na Física da Matéria Condensada, tornando os sistemas fortemente correlacionados um tópico de grande interesse devido à possibilidade de estudar os aspectos fundamentas da interação elétron-elétron, que são o âmago da supercondutividade. Desta forma, a classe de condutores moleculares $(TMTTF)_2X$ (onde TMTTF é tetrametiltetratiafuvaleno e X é um contra-ânion) desempenha um papel sistemático e fundamental no estudo de tais aspectos de correlação. Nesta tese de mestrado, os materiais de interesse foram o $(TMTTF)_2PF_6$-H_{12} e o $(TMTTF)_2PF_6$-D_{12}, onde uma anomalia na constante dielétrica diferente para os dois sais foi observada na transição ferroelétrica de Mott-Hubbard através de medidas de constante dielétrica quasi-estática no eixo c^* (contribuição iônica) e o comportamento tipo *relaxor* da variante hidrogenada foi analisado com base na teoria de campo médio. Uma revisão de transições de fase clássicas e quânticas também foi realizada com o objetivo de estudar o chamado efeito magneto-calórico para o modelo do paramagneto de Brillouin (o parâmetro de Grüneisen magnético), que é uma grandeza Física única e poderosa para detectar experimentalmente uma transição de fase quântica induzida por campo magnético em um sistema real. Ainda, um estudo comparativo entre as fases δ (hexagonal) e δ' (tetragonal) da liga binária $FeSe_{1-x}$ foi realizado e monocristais foram sintetizados utilizando o método de síntese de estado sólido visando atingir a fase δ.

Contents

Chapter 1

Introduction and motivation

In order to explore fundamental aspects of matter, it is worth to make a systematic comparison between the fundamental literature taught in the undergraduate course of Physics and the most recent investigated topics of Physics as well.

Since the discovery of the electron followed by the foundation of quantum mechanics, several years went through and the importance of the electron is only increasing regarding the so-called border science and its interaction gives rise to several exotic phenomena of matter, e.g. superconductivity.

In this regard, systems where the interaction between electrons is significant (strongly correlated electron systems) plays a fundamental role in order to unlock how such exotic phases behave. Understanding its fundamental aspects will give our scientific community the tools to manipulate it and create great scientific advances, e.g. room-temperature superconductivity.

This Master Thesis is divided into three main chapters:

- Chapter 1: A review of fundamental models of magnetism is performed regarding the paramagnetism in both metals (Pauli) and insulators (Brillouin), as well as the exact solution for the one-dimensional (1D) Ising-model. A review of classical phase transitions is discussed based on the Landau theory and also the fundamental aspects of quantum phase transitions is presented. Yet, the so-called Grüneisen parameter is presented with the focus on the magneto-caloric effect (magnetic Grüneisen parameter), which was analytically calculated for the Brillouin model.

- Chapter 2: A historical discussion regarding superconductivity is presented in details followed by a systematic description of a particular synthesis method (solid state physics reaction) employed to synthesize several superconducting alloys. Emphasis was given to the binary alloy $FeSe_{1-x}$, since its critical temperature (T_c) can be increased through hydrostatic external pressure. The focus of this chapter was to discuss the synthesis of single-crystals of the δ phase of $FeSe_{1-x}$, which is predicted to be insulating, and compare directly with its superconducting δ' phase in order to understand the suppression of superconductivity in the δ phase.

- Chapter 3: A relevant fundamental literature review is performed regarding the molecular conductors of the family $(TMTTF)_2X$, the extended Hubbard model, the dielectric constant and the Clausius-Mossoti relation and the charge-ordered phase.

The main focus of this Master Thesis was to compare the physical properties of the fully hydrogenated and the 97.5% deuterated variant of the system $(TMTTF)_2PF_6$. Electrical resistivity $\rho(T)$ and ionic dielectric constant $\varepsilon'(T, B)$ measurements were carried out in such systems exclusively in the Solid State Physics Laboratory in Rio Claro, SP − Brazil, and the data were analyzed regarding the insertion of defects into the system and the mean-field theory.

The motivation to investigate such topics is not only to characterize or describe the physical systems of interest in this Master Thesis, but to make important contributions to the scientific community in order to advance Science a little further.

Chapter 2

Introduction to magnetism, phase transitions, and the magnetic Grüneisen parameter

The discussion presented below is based on Blundell's, Nolting's and Reif's books [1–3], in which a comprehensive and detailed description of the involved quantities is reported. The physical quantities discussed in the following are of relevance for the discussion of the Physics explored in this work.

2.1 Fundamental aspects

Regarding statistical mechanics, the aim is always to analyze the average properties of a certain system by mathematically predicting the physical macroscopic behavior through analyzing the microscopic ones. A good example is the liquid-to-gas phase transition of water. Supposing that the forces between the water molecules are very well known so it can be calculated how much energy it would be necessary to break the bonding between the atoms of hydrogen (H) and oxygen (O). When such physical phenomenon occurs, the water goes from liquid to steam (observable discontinuity of its density at the transition temperature) characterizing a phase transition.

On the other hand, a proper analogy with such discontinuity on the water's density can be done with the magnetization, in a system which presents the so-called spontaneous magnetization. Suppose a one-dimensional chain of spins without applied magnetic field so they are all pointing in different directions. Increasing the magnetic field will result in starting to orientate all the spins in the direction of the applied field until a determined value is achieved that all spins are pointing in the same direction, so the system is magnetized (see Figure 2.1). Depending on the system, ferromagnetic materials for example can remain magnetized even after the field decreases to zero, this is called spontaneous magnetization.

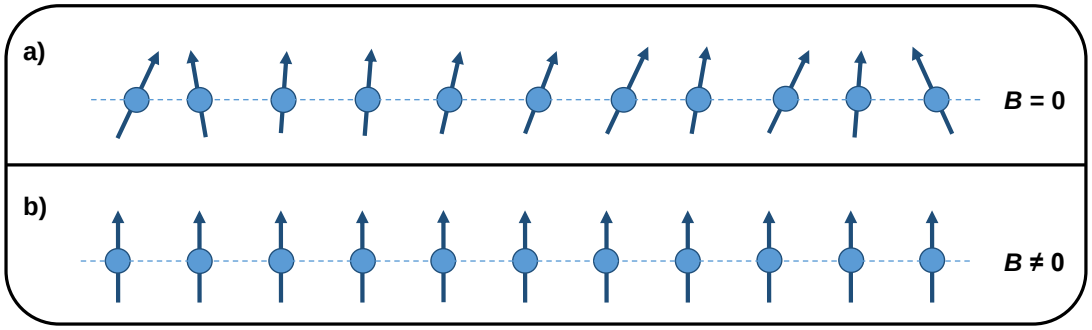

Figure 2.1: a) One dimensional spin chain without applied magnetic field so they are all non-aligned; b) after applying a magnetic field all spins align in the same direction, there are finite magnetic moment so the system is magnetized [4].

2.2 Paramagnetism in insulators – the Brillouin model

Consider a system of N atoms with no interaction between them at temperature T with the local field B acting on the atom along the $\vec{z}$ direction. The magnetic energy E of a single atom is given by:

$$E = -\vec{\mu} \cdot \vec{B}, \tag{2.1}$$

where $\vec{\mu}$ is the magnetic moment vector of one single atom and it is related to the total angular momentum by the expression:

$$\vec{\mu} = g\mu_B \vec{J}, \tag{2.2}$$

where $\vec{J}$ is the total angular momentum $\vec{J} = \vec{L} + \vec{S}$, $\vec{L}$ is the orbital angular momentum, $\vec{S}$ is the spin angular momentum, μ_B is the Bohr magneton and g is the Landé factor described as:

$$g = 1 + \frac{J(J+1) + S(S+1) - L(L+1)}{2J(J+1)}.$$

The Bohr magneton μ_B is given by:

$$\mu_B = \frac{e\hbar}{2m_e},$$

where e is the elementary charge of the electron [5], $\hbar$ is the reduced Planck's constant, namely $h/2\pi$, and m_e is the electron rest mass. Considering $e = 1.60 \times 10^{-19}\,\mathrm{C}$, $\hbar = 1.05 \times 10^{-34}\,\mathrm{J.s}$ and $m_e = 9.11 \times 10^{-31}\,\mathrm{kg}$:

$$\mu_B = \frac{(1.60 \times 10^{-19}\,\mathrm{C}).(1.05 \times 10^{-34}\,\mathrm{J.s})}{2 \cdot (9.11 \times 10^{-31}\,\mathrm{kg})} = 9.22 \times 10^{-24}\,\mathrm{J.T^{-1}}.$$

Regarding the magnetic field in Equation 2.1 it is relevant to mention that the field B is pointing in the z direction and is not quite the same as an external one since it also includes the magnetic moment contributions from all the other atoms. In the case of only a few atoms, this contribution is usually not relevant since it is very small. Replacing Equation 2.2 into 2.1:

$$E = -g\mu_B \vec{J} \cdot \vec{B} = -g\mu_B B J_z, \tag{2.3}$$

where J_z is:

$$J_z = m = -J, -J+1, -J+2, ..., J-1, J, \tag{2.4}$$

where m is all the possible values between $-J$ and J in integer steps.

Furthermore, m has $2J+1$ possible values which correspond to all the projections of the angular momentum vector along the z-axis.

Considering Equation 2.3, the magnetic energy of the atoms is given by:

$$E_m = -g\mu_B Bm. \tag{2.5}$$

The probability to encounter an atom at a state m is:

$$P_m \propto e^{-\beta E_m} = e^{\beta g\mu_B Bm}, \tag{2.6}$$

where:

$$\beta = \frac{1}{k_B T}, \tag{2.7}$$

and k_B is the Boltzmann constant.

The z component of the magnetic moment in this state is:

$$\mu_z = g\mu_B m. \tag{2.8}$$

In order to calculate the mean z component of the magnetic moment $\bar{\mu_z}$, the Maxwell-Boltzmann statistics is employed:

$$\bar{\mu_z} = \frac{\sum_{m=-J}^{J} \mu_z e^{-\beta E_m}}{Z}. \tag{2.9}$$

Considering the partition function Z as:

$$Z = \sum_{m=-J}^{J} e^{\beta g\mu_B Bm}, \tag{2.10}$$

the mean z component of the magnetic moment is given by:

$$\bar{\mu_z} = \frac{\sum_{m=-J}^{J} e^{\beta g\mu_B Bm}(g\mu_B m)}{\sum_{m=-J}^{J} e^{\beta g\mu_B Bm}}. \tag{2.11}$$

Conveniently writing:

$$\sum_{m=-J}^{J} e^{\beta g\mu_B Bm}(g\mu_B m) = \frac{1}{\beta}\frac{\partial Z}{\partial B}. \tag{2.12}$$

Inserting Equation 2.12 into 2.11:

$$\bar{\mu_z} = \frac{1}{\beta}\frac{1}{Z}\frac{\partial Z}{\partial B} = \frac{1}{\beta}\frac{\partial lnZ}{\partial B}. \tag{2.13}$$

Now consider:

$$\eta = \beta g\mu_B B = \frac{g\mu_B B}{k_B T}, \tag{2.14}$$

as a dimensionless parameter to analyze the ratio of the magnetic energy $g\mu_B B$ to the thermal energy $k_B T$. Thus, Equation 2.10 becomes:

$$Z = \sum_{m=-J}^{J} e^{\eta m} = e^{-\eta J} + e^{-\eta(J-1)} + ... + e^{\eta J}. \tag{2.15}$$

Multiplying Equation 2.15 by e^{η}:

$$Ze^{\eta} = e^{\eta} \cdot e^{-\eta J} + e^{\eta} \cdot e^{-\eta(J-1)} + ... + e^{\eta} \cdot e^{\eta J},$$

$$Ze^{\eta} = e^{-\eta(J-1)} + e^{-\eta(J-2)} + ... + e^{-\eta(J+1)}. \tag{2.16}$$

By subtracting Equations 2.15 and 2.16, the only terms left are the first one from Equation 2.15 ($e^{-\eta J}$) and the last from Equation 2.16 ($e^{\eta(J+1)}$). Thus:

$$Z - Z \cdot e^{\eta} = e^{-\eta J} - e^{\eta(J+1)},$$

$$Z(1 - e^{\eta}) = e^{-\eta J} - e^{\eta(J+1)}.$$

Therefore:

$$Z = \frac{e^{-\eta J} - e^{\eta(J+1)}}{1 - e^{\eta}}. \tag{2.17}$$

Multiplying the numerator and the denominator of Equation 2.17 by $e^{-\eta/2}$:

$$Z = \frac{e^{-\eta J - \eta/2} - e^{[\eta(J+1) - \eta/2]}}{e^{-\eta/2} - e^{\eta - \eta/2}} = \frac{e^{-\eta(J+1/2)} - e^{\eta(J+1/2)}}{e^{-\eta/2} - e^{\eta/2}}. \tag{2.18}$$

Considering that:

$$\sinh(y) = \frac{e^{y} - e^{-y}}{2},$$

Equation 2.18 becomes:

$$Z = \frac{\cancel{2} \cdot \sinh\left[\eta\left(J + 1/2\right)\right]}{\cancel{2} \cdot \sinh\left(\frac{\eta}{2}\right)}. \tag{2.19}$$

Thus,

$$Z = \frac{\sinh\left[\eta\left(J + 1/2\right)\right]}{\sinh\left(\frac{\eta}{2}\right)}. \tag{2.20}$$

Replacing Equation 2.20 into Equations 2.13 and 2.14:

$$\bar{\mu_z} = \frac{1}{\beta}\frac{\partial \ln Z}{\partial B} = \frac{1}{\beta}\frac{\partial \ln Z}{\partial \eta}\overbrace{\frac{\partial \eta}{\partial B}}^{g\mu_B\beta} = \frac{1}{\cancel{\beta}}\frac{\partial \ln Z}{\partial \eta} g\mu_B \cancel{\beta} = g\mu_B \frac{\partial \ln Z}{\partial \eta}, \tag{2.21}$$

$$\bar{\mu_z} = g\mu_B \left[\frac{(J + 1/2)\cosh[\eta(J + 1/2)]}{\sinh(J + 1/2)\eta} - \frac{(1/2)\cosh(\eta/2)}{\sinh(\eta/2)}\right], \tag{2.22}$$

$$\bar{\mu_z} = g\mu_B J B_J(\eta), \tag{2.23}$$

where $B_J(\eta)$ is the so-called Brillouin function, given by the form:

$$B_J(\eta) = \frac{1}{J}\left[\left(J + \frac{1}{2}\right)\coth\left(J + \frac{1}{2}\right)\eta - \frac{1}{2}\coth\left(\frac{\eta}{2}\right)\right]. \tag{2.24}$$

The hyperbolic cotangent can also be written by the form:

$$\cosh(y) \equiv \frac{\cosh(y)}{\sinh(y)} = \frac{e^{y} + e^{-y}}{e^{y} - e^{-y}}. \tag{2.25}$$

In the case where $y \gg 1$, the trivial result is $\coth(y) = 1$. Considering the case where $y \ll 1$, it is possible to expand Equation 2.25 in a power series by the form:

$$\coth(y) = \frac{1 + \frac{1}{2}y^2 + ...}{y + \frac{1}{6}y^2 + ...} \simeq \frac{1}{y}\left(1 + \frac{1}{2}y^2\right)\left(1 + \frac{1}{6}y^2\right)^{-1}. \tag{2.26}$$

Considering the binomial expansion:

$$(1+x)^n = 1 + nx + \frac{n(n-1)x^2}{2!} + ..., \tag{2.27}$$

it is possible to rewrite $(1+\frac{1}{6}y^2)^{-1}$ from Equation 2.26 by the form:

$$\left(1+\frac{1}{6}y^2\right)^{-1} \simeq 1 + (-1)\frac{y^2}{6} + \frac{(-1)[(-1)-1]}{2!}\left(\frac{y^2}{6}\right)^2 = 1 - \frac{y^2}{6} + \cancel{\frac{y^4}{36}} + ... \simeq \left(1 - \frac{y^2}{6}\right). \tag{2.28}$$

Since it is being considered that $y \ll 1$, the term in the expansion $y^4/36$ is close to zero and can be neglected, as well as the higher order terms of the expansion.

Thus, replacing Equation 2.28 into 2.26:

$$\coth(y) = \frac{1}{y}\left(1+\frac{1}{2}y^2\right)\left(1-\frac{1}{6}y^2\right) = \frac{1}{y}\left(1 - \frac{y^2}{6} + \frac{y^2}{2} - \cancel{\frac{y^4}{12}}\right) \simeq \left(\frac{1}{y} + \frac{y}{3}\right). \tag{2.29}$$

Analogously from Equation 2.28, the term $-y^4/12$ can be neglected since it is close to zero ($y \ll 1$).

Replacing Equation 2.29 into 2.24:

$$B_J(\eta) = \frac{1}{J}\left\{(J+1/2)\left[\frac{1}{(J+1/2)\eta} + \frac{1}{3}(J+1/2)\eta\right] - \frac{1}{2}\left[\frac{2}{\eta} + \frac{\eta}{6}\right]\right\}, \tag{2.30}$$

$$B_J(\eta) = \frac{1}{J}\left\{\cancel{\frac{1}{\eta}}\overbrace{(J+1/2)}^{1}\cancel{\frac{1}{(J+1/2)}} + \frac{1}{3}(J+1/2)^2\eta - \cancel{\frac{1}{\eta}} - \frac{\eta}{12}\right\}, \tag{2.31}$$

$$B_J(\eta) = \frac{1}{J}\left\{\frac{\eta}{3}(J^2+J+1/4) - \frac{\eta}{12}\right\}, \tag{2.32}$$

$$B_J(\eta) = \frac{1}{J}\left\{\frac{\eta}{3}\left[J^2 + J + \cancel{\frac{1}{4}} - \cancel{\frac{1}{4}}\right]\right\}, \tag{2.33}$$

$$B_J(\eta) = \frac{\eta}{3J}(J^2+J) = \frac{\eta\cancel{J}(J+1)}{3\cancel{J}} = \frac{\eta}{3}(J+1). \tag{2.34}$$

Considering N atoms per unit of volume, the mean magnetization $\bar{M}_z$ is given by:

$$\bar{M}_z = N\bar{\mu}_z = Ng\mu_B J B_J(\eta). \tag{2.35}$$

So, Equation 2.35 is:

$$\bar{M}_z = Ng\mu_B J\frac{\eta}{3}(J+1) = \underbrace{\frac{Ng^2{\mu_B}^2 J(J+1)}{3k_B}}_{C}\frac{B}{T}, \tag{2.36}$$

where C is the so-called Curie's constant.

The magnetic susceptibility χ can be defined as:

$$\chi = \frac{\bar{M}_z}{B}. \tag{2.37}$$

Thus, Equation 2.36 becomes:

$$\chi = \frac{C}{T}. \tag{2.38}$$

Equation 2.38 represents the so-called Curie's Law, describing a linear behavior of $1/\chi$ as a function of temperature for an insulating paramagnet.

2.3 Paramagnetism in Metals – Pauli paramagnetism

To describe the paramagnetism in a metal [4], i.e. itinerant electrons, consider that each electron will contribute with $-\mu_B/V$ ($g = 2$) to the magnetization density if the spin is parallel to a field B, and μ_B/V if antiparallel, where V is the volume per conduction electron.

Considering the total numbers of electrons per unit of volume $n\pm$ (where n_+ represents the number of electrons with parallel spins and n_- with antiparallel), the magnetization can be written:

$$M = -\mu_B(n_+ - n_-). \tag{2.39}$$

If only the magnetic moments of the electrons are affected, it means there will be an energy shift in each electronic level of $\pm\mu_B B$ accordingly if the spin is parallel or antiparallel to B. Such interaction can be expressed in terms of density levels.

Consider $g_\pm(\varepsilon)d\varepsilon$ the number of spins between the values of energy ε and $\varepsilon + d\varepsilon$, so it can be expressed:

$$g_\pm(\varepsilon) = \frac{1}{2}g(\varepsilon) \qquad [B = 0], \tag{2.40}$$

where $g(\varepsilon)$ is the ordinary density levels. Since the energy levels with a specified spin parallel to B is shifted up from its zero-field value by $\mu_B B$, the number of levels with energy ε in the presence of B is the same as the number with energy $(\varepsilon - \mu_B B)$ in the absence of B:

$$g_+(\varepsilon) = \frac{1}{2}g(\varepsilon - \mu_B B). \tag{2.41}$$

$$g_-(\varepsilon) = \frac{1}{2}g(\varepsilon + \mu_B B). \tag{2.42}$$

The number of electrons per unit of volume of each spin configuration is:

$$n_\pm = \int d\varepsilon g \pm (\varepsilon) f(\varepsilon), \tag{2.43}$$

where,

$$f(\varepsilon) = \frac{1}{e^{\beta(\varepsilon-\mu)} + 1}. \tag{2.44}$$

The chemical potential μ can be determined from the fact that the total electronic density is:

$$n = n_+ + n_-. \tag{2.45}$$

Thus, it is possible to use Equations 2.39 and 2.40 to determine the magnetization density as a function of n, by employing a Taylor series:

$$g_\pm(\varepsilon) = \frac{1}{2}g(\varepsilon \pm \mu_B B) = \frac{1}{2}g(\varepsilon) \pm \frac{1}{2}\mu_B B g'(\varepsilon). \tag{2.46}$$

Considering Equation 2.40:

$$n_\pm = \frac{1}{2}\int g(\varepsilon)f(\varepsilon)d\varepsilon \mp \frac{1}{2}\mu_B B \int d\varepsilon g'(\varepsilon)f(\varepsilon). \tag{2.47}$$

Thus, from Equation 2.45:

$$n = \int g(\varepsilon)f(\varepsilon)d\varepsilon. \tag{2.48}$$

Such equation is exactly the electronic density of states in the absence of a magnetic field B, so the chemical potential can be encountered in the form:

$$\mu = \varepsilon_F - \frac{\pi^2 (k_B T)^2}{6} \frac{g'(\varepsilon_F)}{g(\varepsilon_F)}, \tag{2.49}$$

where ε_F is the Fermi energy.

Since $g(\varepsilon)$ varies as $\varepsilon^{1/2}$ by the expression:

$$g(\varepsilon) = \frac{3}{2} \frac{n}{\varepsilon_F} \left(\frac{\varepsilon}{\varepsilon_F} \right)^{1/2}, \tag{2.50}$$

$$\mu = \varepsilon_F \left[1 - \frac{1}{3} \left(\frac{\pi k_B T}{2\varepsilon_F} \right)^2 \right], \tag{2.51}$$

$$\mu = \varepsilon_F \left[1 + O \left(\frac{k_B T}{\varepsilon_F} \right)^2 \right]. \tag{2.52}$$

Together with Equations 2.39 and 2.47 gives a magnetization density:

$$M = {\mu_B}^2 B \int_0^{\varepsilon_F} g'(\varepsilon) f(\varepsilon) d\varepsilon. \tag{2.53}$$

In order to properly rewrite Equation 2.53, a few mathematical steps are required. Thus, it is possible to write:

$$\frac{\partial}{\partial \varepsilon}(f \cdot g) = g \frac{\partial f}{\partial \varepsilon} + f \frac{\partial g}{\partial \varepsilon},$$

$$\int_0^{\varepsilon_F} \frac{\partial}{\partial \varepsilon}(f \cdot g) d\varepsilon = \int_0^{\varepsilon_F} g \frac{\partial f}{\partial \varepsilon} d\varepsilon + \int_0^{\varepsilon_F} f \frac{\partial g}{\partial \varepsilon} d\varepsilon,$$

$$\int_0^{\varepsilon_F} f \frac{\partial g}{\partial \varepsilon} d\varepsilon = f \cdot g \Big|_0^{\varepsilon_F} - \int_0^{\varepsilon_F} g \frac{\partial f}{\partial \varepsilon} d\varepsilon, \tag{2.54}$$

$$f \cdot g \Big|_0^{\varepsilon_F} = \frac{g(\varepsilon)}{e^{(\varepsilon-\mu)/k_B T} + 1} \Big|_0^{\varepsilon_F}.$$

Replacing $g(\varepsilon)$ from Equation 2.50:

$$f \cdot g \Big|_0^{\varepsilon_F} = \frac{g(\varepsilon)}{e^{(\varepsilon-\mu)/k_B T} + 1} \Big|_0^{\varepsilon_F} = \left(\frac{3n}{2\varepsilon_F^{3/2}} \right) \frac{\varepsilon^{1/2}}{e^{(\varepsilon-\mu)/k_B T} + 1} \Big|_0^{\varepsilon_F},$$

$$f \cdot g \Big|_0^{\varepsilon_F} = \left(\frac{3n}{2\varepsilon_F^{3/2}} \right) \left[\overbrace{\frac{\varepsilon_F^{1/2}}{e^{(\varepsilon_F-\mu)/k_B T} + 1}}^{0, \text{ since } T = 0\,\text{K at } \varepsilon_F} - \frac{0}{e^{-\mu/k_B T} + 1} \right] = 0.$$

Thus, Equation 2.54 becomes:

$$\int_0^{\varepsilon_F} f \frac{\partial g}{\partial \varepsilon} d\varepsilon = \int_0^{\varepsilon_F} g(\varepsilon) \left(-\frac{\partial f}{\partial \varepsilon} d\varepsilon \right).$$

So, Equation 2.53 becomes:

$$M = \mu_B^2 B \int_0^{\varepsilon_F} g(\varepsilon) \left(-\frac{\partial f}{\partial \varepsilon} \right) d\varepsilon. \tag{2.55}$$

Expanding the function $-\partial f / \partial \varepsilon$ in a Taylor series until the first-order term so that T^2 terms can be despised, and evaluating the result at $T = 0\,\text{K}$, it is possible to conclude that:

$$-\frac{\partial f}{\partial \varepsilon} = \delta(\varepsilon - \varepsilon_F) \tag{2.56}$$

So Equation 2.55 can be rewritten by the form:

$$M = \mu_B^2 B \overbrace{\int_0^{\varepsilon_F} g(\varepsilon)\delta(\varepsilon - \varepsilon_F)d\varepsilon}^{g(\varepsilon_F)}. \tag{2.57}$$

Thus,

$$M = \mu_B^2 B g(\varepsilon_F). \tag{2.58}$$

Since the $T \neq 0$ corrections to $-\partial f/\partial \varepsilon$ are of orders $(k_B T/\varepsilon_F)^2$, then Equation 2.58 is also valid at high temperatures. Since we are dealing with the magnetism associated with the conduction electrons, it is natural to consider that the energies associated with those entities are in the range of the Fermi ones [4].

$$\varepsilon_F = \frac{\hbar^2 {k_F}^2}{2m_e}, \tag{2.59}$$

where m_e is the electron mass. Considering that:

$$a_0 = \frac{\hbar^2}{m_e e^2}, \tag{2.60}$$

where e is the electron charge. It is possible to write Equation 2.59 in terms of the Bohr radius a_0 by the expression:

$$\varepsilon_F = \left(\frac{e^2}{2a_0}\right)(k_F a_0)^2, \tag{2.61}$$

where $(e^2/2a_0)$ is known as the Rydberg (Ry) = 13.6 eV.

The expression for k_F can be given as a function of the Bohr radius a_0 and the radius of the free electron sphere r_s, by the form:

$$k_F = \frac{3.63}{r_s/a_0}. \tag{2.62}$$

Thus, Equation 2.61 is given by:

$$\varepsilon_F = \frac{50.1\, eV}{(r_s/a_0)^2} = \frac{8.026909 \times 10^{-18}\,\mathrm{J}}{(r_s/a_0)^2}. \tag{2.63}$$

From Equation 2.63 it is possible to calculate the Fermi temperature T_F by the expression:

$$\varepsilon_F = k_B T_F \rightarrow T_F = \frac{\varepsilon_F}{k_B}, \tag{2.64}$$

$$T_F = \frac{8.026909 \times 10^{-18}}{1.38064852 \times 10^{-23}} \cdot \frac{1}{(r_s/a_0)^2}. \tag{2.65}$$

So, the Fermi temperature is given by:

$$\boxed{T_F = \frac{58.2}{(r_s/a_0)^2} \times 10^4\,\mathrm{K}.} \tag{2.66}$$

From 2.58 it is possible to write the magnetic susceptibility:

$$\chi = \left(\frac{\partial M}{\partial B}\right) = \mu_B^2 g(\varepsilon_F). \tag{2.67}$$

This is the so-called Pauli paramagnetic susceptibility. Differing from the paramagnetic behavior of the Curie's Law, the susceptibility of the conducting electrons does not depend on the temperature. Regarding the free electrons case, the density of levels is given by:

$$g(\varepsilon_F) = \frac{mk_F}{\hbar^2\pi^2}. \tag{2.68}$$

Replacing 2.68 into 2.67:

$$\chi_{Pauli} = \left(\frac{\alpha}{2\hbar}\right)^2 (a_0 k_F), \tag{2.69}$$

where:

$$\alpha = \frac{e^2}{hc} = \frac{1}{137}, \tag{2.70}$$

is the so-called fine structure constant.

Also, the Pauli susceptibility can be written as:

$$\boxed{\chi_{Pauli} = \frac{2.59}{r_s/a_0} \times 10^{-6}}. \tag{2.71}$$

Equation 2.71 express the fact that Pauli susceptibility is extremely low because the exclusion principle is much more effective than the thermal disorder in suppressing the tendency of the spin magnetic moments to align with B.

Also, Pauli paramagnetism can be compared with Curie's Law and it can be verified that Pauli susceptibility is hundreds of times smaller than the Curie one and is non-temperature dependent.

2.4 The 1D−Ising model

There are many existing phenomena that can be looked upon a one-dimensional system concomitant with nearest-neighbor interaction, see e.g. [6]. Therefore, one model of particular interest is the so-called Ising model. In this section is discussed its exact solution [7].

Considering a chain of N spins interacting only with the two nearest ones, so the one-dimensional open chain is replaced by a curved one so that the N^{th} spin interacts with the first one, not altering the thermodynamic properties of the chain.

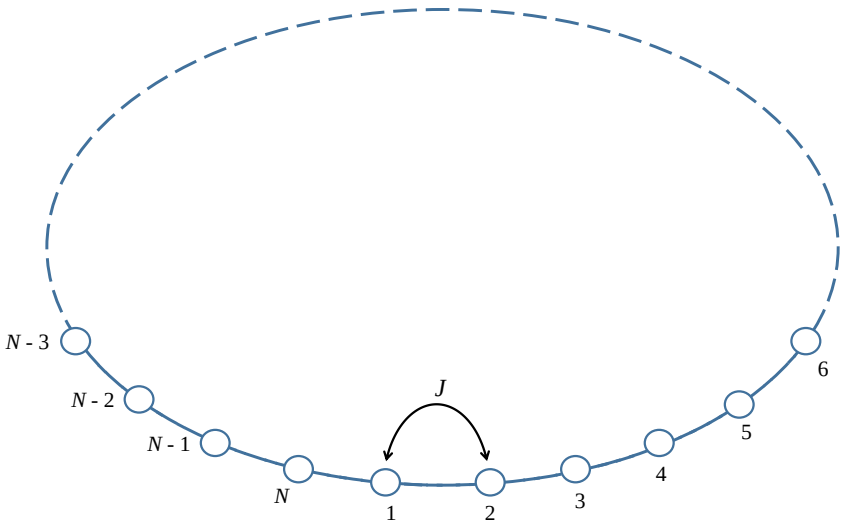

Figure 2.2: Ising closed infinite chain where each small circle represent a spin and J represents the coupling constant between the spins [7].

With such configuration the Hamiltonian of the system can be written:

$$H_N\{\sigma_i\} = -J\sum_{i=1}^{N}\sigma_i\sigma_j - \mu_B B\sum_{i=1}^{N}\sigma_i, \tag{2.72}$$

where J is the coupling term between the spins, σ_i and σ_j are the interaction between two nearest-neighbor spins. Since they are neighbors it is possible to write $\sigma_j = \sigma_{i+1}$, so the Hamiltonian:

$$H_N\{\sigma_i\} = -J\sum_{i=1}^{N}\sigma_i\sigma_{i+1} - \frac{1}{2}\mu_B B\sum_{i=1}^{N}(\sigma_i + \sigma_{i+1}). \tag{2.73}$$

From Equation 2.73 it is possible to calculate the partition function $Z_N(T, B)$:

$$Z_N(T, B) = \sum_{i=1}^{N} e^{-\beta H_N}. \tag{2.74}$$

Inserting Equation 2.73 into Equation 2.74:

$$Z_N(T, B) = \sum_{\sigma_1=\pm1} ... \sum_{\sigma_N=\pm1} \exp\left\{\beta\sum_{i=1}^{N}\left[J\sigma_i\sigma_{i+1} + 1/2\mu_B B(\sigma_i + \sigma_{i+1})\right]\right\}. \tag{2.75}$$

It is possible to rewrite Equation 2.75 by a matrix elements operator $\boldsymbol{P}$ by the form:

$$\langle\sigma_i|\boldsymbol{P}|\sigma_{i+1}\rangle = \exp\left\{\beta\left[J\sigma_i\sigma_{i+1} + 1/2\mu_B B\left(\sigma_i + \sigma_{i+1}\right)\right]\right\}. \tag{2.76}$$

So Equation 2.75 becomes:

$$Z_N(T, B) = \sum_{\sigma_1=\pm1} ... \sum_{\sigma_{N\pm1}} \langle\sigma_1|\mathbf{P}|\sigma_2\rangle\langle\sigma_2|x\mathbf{P}|\sigma_3\rangle...\langle\sigma_{N-1}|\mathbf{P}|\sigma_N\rangle\langle\sigma_N|\mathbf{P}|\sigma_1\rangle. \tag{2.77}$$

Regarding Equation 2.76, the matrix $\boldsymbol{P}$ is given by:

$$(\boldsymbol{P}) = \begin{pmatrix} \langle+1|\boldsymbol{P}|+1\rangle & \langle+1|\boldsymbol{P}|-1\rangle \\ \langle-1|\boldsymbol{P}|+1\rangle & \langle-1|\boldsymbol{P}|-1\rangle \end{pmatrix}. \tag{2.78}$$

$$\langle+1|\boldsymbol{P}|+1\rangle = e^{\beta[J\cdot(+1)\cdot(+1)+1/2\mu_B B(1+1)]} = e^{\beta[J+\mu_B B]},$$

$$\langle+1|\boldsymbol{P}|-1\rangle = e^{\beta[J\cdot(+1)\cdot(-1)+1/2\mu_B B(1-1)]} = e^{-\beta J},$$

$$\langle-1|\boldsymbol{P}|+1\rangle = e^{\beta[J\cdot(-1)\cdot(+1)+1/2\mu_B B(1-1)]} = e^{-\beta J},$$

$$\langle-1|\boldsymbol{P}|-1\rangle = e^{\beta[J\cdot(-1)\cdot(-1)+1/2\mu_B B(-1-1)]} = e^{\beta[J-\mu_B B]}.$$

So the matrix $\boldsymbol{P}$ is:

$$(\boldsymbol{P}) = \begin{pmatrix} e^{\beta[J+\mu_B B]} & e^{-\beta J} \\ e^{-\beta J} & e^{\beta[J-\mu_B B]} \end{pmatrix}. \tag{2.79}$$

So, Equation 2.77 results in:

$$Z_N(T, B) = \sum_{\sigma_1\pm1} \langle\sigma_1|\boldsymbol{P}^N|\sigma_1\rangle = \text{Tr}\ (\boldsymbol{P}^N) = {\lambda_+}^N + {\lambda_-}^N, \tag{2.80}$$

where λ_1 and λ_2 are the eigenvalues of $\boldsymbol{P}$ (that is, the eigenenergies of H_N) and can be found making:

$$\begin{vmatrix} e^{\beta(J+\mu_B B)} - \lambda & e^{-\beta J} \\ e^{-\beta J} & e^{\beta(J-\mu_B B)} - \lambda \end{vmatrix} = 0$$

$$e^{\beta(J+\mu_B B)} \cdot e^{\beta(J-\mu_B B)} - \lambda e^{\beta(J+\mu_B B)} - \lambda e^{\beta(J-\mu_B)} + \lambda^2 - e^{-2\beta J} = 0.$$

$$\lambda^2 + \overbrace{e^{2\beta J} - e^{-2\beta J}}^{2\sinh(2\beta J)} - \lambda(\underbrace{e^{\beta(J-\mu_B B)} + e^{-\beta(-J+\mu_B B)}}_{e^{\beta J}\underbrace{(e^{\mu_B B} + e^{-\mu_B B})}_{2\cosh(\beta\mu_B B)}}) = 0.$$

So,

$$\lambda^2 - \lambda \cdot 2e^{\beta J}\cosh(\beta\mu_B B) + 2\sinh(2\beta J) = 0. \tag{2.81}$$

Solving Equation 2.81 for λ:

$$\lambda_\pm = \frac{2e\beta J\cosh(\beta\mu_B B) \pm \{4e^{2\beta J}\cosh^2(\beta\mu_B B) - 8\sinh(2\beta J)\}^{1/2}}{2}. \tag{2.82}$$

$$\lambda_\pm = \frac{2e\beta J\cosh(\beta\mu_B B) \pm 2[e^{2\beta J}\overbrace{\cosh^2(\beta\mu_B B)}^{1+\sinh^2(\beta\mu_B B)} - \overbrace{2\sinh(2\beta J)}^{(e^{2\beta J} - e^{-2\beta J})}]^{1/2}}{2}.$$

$$\lambda_\pm = e^{\beta J}\cosh(\beta\mu_B B) \pm \{e^{2\beta J}[1 + \sinh^2(\beta\mu_B B)] - [e^{2\beta J} - e^{-2\beta J}]\}.$$

$$\lambda_\pm = e^{\beta J}\cosh(\beta\mu_B B) \pm \{\cancel{e^{2\beta J}} + e^{2\beta J}\sinh^2(\beta\mu_B B) - \cancel{e^{2\beta J}} + e^{-2\beta J}]\}.$$

$$\boxed{\lambda_\pm = e^{\beta J}\cosh(\beta\mu_B B) \pm \{e^{2\beta J}\sinh^2(\beta\mu_B B) + e^{-2\beta J}\}}.$$

Considering that $\lambda_+ > \lambda_-$, when $N \to \infty$ it is considered only the λ_+ eigenvalue due to the fact that λ_- is tiny when compared with λ_+ in the thermodynamic limit. Thus, the partition function from Equation 2.80 becomes:

$$Z_N(T, B) = {\lambda_+}^N. \tag{2.83}$$

$$\ln[Z_N(T, B)] = \ln(\lambda_+)^N.$$

$$\ln[Z_N(T, B)] = N\ln(\lambda_+). \tag{2.84}$$

Inserting Equation 2.84 into the Helmholtz free energy:

$$F(T, B) = -k_B T\ln[Z_N(T, B)]. \tag{2.85}$$

$$F(T, B) = -k_B TN\ln[e^{\beta J}\cosh(\beta\mu_B B) + \{e^{2\beta J}\sinh^2(\beta\mu_B B) + e^{-2\beta J}\}^{1/2}].$$

$$F(T, B) = -k_B TN\ln[e^{\beta J}\cosh(\beta\mu_B B) + \{e^{2\beta J}[\sinh^2(\beta\mu_B B) + e^{-4\beta J}]\}^{1/2}].$$

$$F(T, B) = -k_B TN\ln[e^{\beta J}\cosh(\beta\mu_B B) + e^{\beta J} \cdot \{\sinh^2(\beta\mu_B B) + e^{-4\beta J}\}^{1/2}].$$

$$F(T,B) = -k_B T N \ln\left[e^{\beta J}\cdot\left(\cosh(\beta\mu_B B) + \{\sinh^2(\beta\mu_B B) + e^{-4\beta J}\}^{1/2}\right)\right].$$

$$F(T,B) = -k_B T N\{\underbrace{\ln e^{\beta J}}_{\beta J} + \ln[\cosh(\beta\mu_B B) + \{\sinh^2(\beta\mu_B B) + e^{-4\beta J}\}^{1/2}]\}.$$

$$F(T,B) = -N\underbrace{k_B T\beta}_{1} J - N k_B T \ln[\cosh(\beta\mu_B B) + \{e^{-4\beta J} + \sinh^2(\beta\mu_B B)\}^{1/2}].$$

Thus, the free energy $F(T,B)$ is given by:

$$F(T,B) = -NJ - N k_B T \ln[\cosh(\beta\mu_B B) + \{e^{-4\beta J} + \sinh^2(\beta\mu_B B)\}^{1/2}]. \tag{2.86}$$

Thus, free energy per spin:

$$f(T,B) = \frac{F(T,B)}{N}, \tag{2.87}$$

is given by:

$$\boxed{f(T,B) = -J - k_B T \ln[\cosh(\beta\mu_B B) + \{e^{-4\beta J} + \sinh^2(\beta\mu_B B)\}^{1/2}].} \tag{2.88}$$

From Equation 2.88 it is possible to derive all the thermodynamic physical quantities, such as:

- Magnetization:
$$M(T,B) = \left(\frac{\partial f(T,B)}{\partial B}\right)_T; \tag{2.89}$$
- Entropy:
$$S(T,B) = -\left(\frac{\partial f(T,B)}{\partial T}\right)_B; \tag{2.90}$$
- Specific heat:
$$C(T,B) = -T\left(\frac{\partial^2 f(T,B)}{\partial T^2}\right)_B. \tag{2.91}$$

2.5 Phase transitions

In this section is presented the mathematical detailed discussion regarding classic phase transitions of first- and second-order, employing the Landau theory [8]. A brief discussion of quantum phase transitions is presented as well.

2.5.1 Introduction to classical phase transitions

Regarding the first-order phase transition [8], an example is a transition between a ferroelectric and a paraelectric state, where a discontinuous change of the saturation polarization can be observed at a transition temperature T_c. A transition between the normal and the superconducting state of a physical system is also a classic phase transition, but a second-order one. One theory that describes the classic phase transition of both first and second order is the Landau theory of phase transitions.

The so-called free energy is the available energy in a solid (for example) and in order to transition between two different phases, there must have free energy in the system. Considering the so-called Landau equation of the free energy density $\hat{F}$ it is possible

to mathematically describe such free energy employing the polarization P (it is worth mentioning that the Landau's theory can be applied for any order parameter, not only for the polarization P), temperature T and the electric field E as one mathematical example of it, given by:

$$\hat{F}(P,T,E) = -EP + g_0 + \frac{1}{2}g_2P^2 + \frac{1}{4}g_4P^4 + \frac{1}{6}g_6P^6 + ..., \tag{2.92}$$

where the g_n coefficients are temperature dependent.

The reason that odd coefficients are not present is due to the unpolarized crystal taking in consideration has a center of inversion symmetry, but crystals can also behave anisotropically regarding the polarization P so in such cases the odd coefficients take place in Equation 2.92. It is possible to find the minimal point of Equation 2.92 by the form:

$$\frac{\partial \hat{F}}{\partial P} = 0 = -E + g_2P + g_4P^3 + g_6P^5 + ... \tag{2.93}$$

Aiming to achieve such example of a ferroelectric phase, the coefficient in P^2 (g_2) can be defined with the condition that it passes through zero at a temperature T_0, given by the form:

$$g_2 = \gamma(T - T_0), \tag{2.94}$$

where γ is a positive constant and T_0 is a temperature near the transition temperature T_c.

2.5.2 Classical first-order phase transitions

Regarding a first order transition, the free energy is expandable until the coefficient g_6, so the free energy is:

$$\hat{F} = -EP + g_0 + \frac{1}{2}g_2P^2 + \frac{1}{4}g_4P^4 + \frac{1}{6}g_6P^6. \tag{2.95}$$

To find the minimum point of $\hat{F}$:

$$\frac{\partial \hat{F}}{\partial P} = 0. \tag{2.96}$$

So:

$$-E + g_2P + g_4P^3 + g_6P^5 = 0. \tag{2.97}$$

Dividing Equation 2.97 for P:

$$-E/P + g_2 + g_4P^2 + g_6P^4 = 0. \tag{2.98}$$

Considering no applied electrical field ($E = 0$) and $P^2 = y$, Equation 2.98 is:

$$g_6y^2 + g_4y + g_2 = 0. \tag{2.99}$$

Now solving for y^2 employing Bhaskara's formula:

$$y = \frac{-g_4 \pm \sqrt{{g_4}^2 - 4g_6g_2}}{2g_6}. \tag{2.100}$$

So, P is given by:

$$P = \left(\frac{-g_4 \pm \sqrt{{g_4}^2 - 4g_6g_2}}{2g_6}\right)^{\frac{1}{2}}. \tag{2.101}$$

Replacing the g_2 coefficient from Equation 2.94 into Equation 2.101:

$$P = \left(\frac{-g_4 \pm \sqrt{{g_4}^2 - 4g_6\gamma(T - T_0)}}{2g_6} \right)^{\frac{1}{2}}. \tag{2.102}$$

Considering $T = T_0$:

$$P = \left(\frac{-g_4 \pm \sqrt{{g_4}^2}}{2g_6} \right)^{\frac{1}{2}}. \tag{2.103}$$

The two possible solutions are:

$$P_1 = \left(\frac{-g_4 + \sqrt{{g_4}^2}}{2g_6} \right)^{\frac{1}{2}} = \left(\frac{-g_4 + g_4}{2g_6} \right)^{\frac{1}{2}} = \left(\frac{0}{2g_6} \right)^{\frac{1}{2}} = 0, \tag{2.104}$$

or

$$P_2 = \left(\frac{-g_4 - \sqrt{{g_4}^2}}{2g_6} \right)^{\frac{1}{2}} = \left(\frac{-g_4 - g_4}{2g_6} \right)^{\frac{1}{2}} = \left(\frac{-2g_4}{2g_6} \right)^{\frac{1}{2}} = \left(-\frac{g_4}{g_6} \right)^{\frac{1}{2}}. \tag{2.105}$$

In order to obtain a finite real valor, it is assumed that the coefficient g_4 is negative, so the solution is real.

Thus, Equation 2.97 is given by:

$$\gamma(T - T_0)P - |g_4|P^3 + g_6P^5 = 0. \tag{2.106}$$

Considering $T_0 = T_c$:

$$\overbrace{\gamma(T - T_c)}^{g_2} P - |g_4|P^3 + g_6P^5 = 0, \tag{2.107}$$

where P is the so-called order parameter in this equation, which is finite below the transition temperature T_c and goes to zero at $T = T_c$ for first-order phase transitions.

2.5.3 Classical second-order phase transitions

In the case of a second order phase transition, the coefficient g_4 is positive so g_6 can be neglected and the expansion goes only until g_4:

$$\frac{\partial \hat{F}}{\partial P} = 0 = -E + g_2P + g_4P^3. \tag{2.108}$$

Replacing g_2 from Equation 2.94 and $E = 0$:

$$\gamma(T - T_0)P + g_4P^3 = 0. \tag{2.109}$$

So:

$$P(\gamma(T - T_0) + g_4P^2) = 0, \tag{2.110}$$

either $P = 0$ or:

$$\gamma(T - T_0) + g_4P^2 = 0. \tag{2.111}$$

$$P^2 = -\frac{\gamma(T - T_0)}{g_4}. \tag{2.112}$$

$$\boxed{P = \sqrt{-\frac{\gamma(T - T_0)}{g_4}} = \left(\frac{\gamma}{g_4} \right)^{\frac{1}{2}} (T_0 - T)^{\frac{1}{2}}}. \tag{2.113}$$

Thus, T_0 in this particular case is the Curie temperature for this phase transition. The transition is considered second-order because the polarization goes continuously to zero at the transition temperature.

Yet, it is possible to relate Equation 2.113 with Equation 4.10 from the mean-field theory, since when the temperature T is exactly the transition temperature (T_0 or T_{co}) both the polarization P and $1/\varepsilon'$ goes to zero (in fact, $1/\varepsilon'$ never goes exactly to zero since ε' has finite values).

2.5.4 Quantum phase transitions

In the last years, quantum phase transitions have regained a wide attention especially by the Solid State Physics community regarding systems with strong correlation effects [9], e.g. the metal-insulator transition in charge-transfer salts [10–12]. The physical properties regarding non-interacting systems formed the primary basis upon which condensed matter Physics developed the view of the behavior of such systems near a quantum critical point. On the other hand, systems with strong electronic interaction play a fundamental role in the fundamental understanding of their behaviors near a quantum critical phase transition.

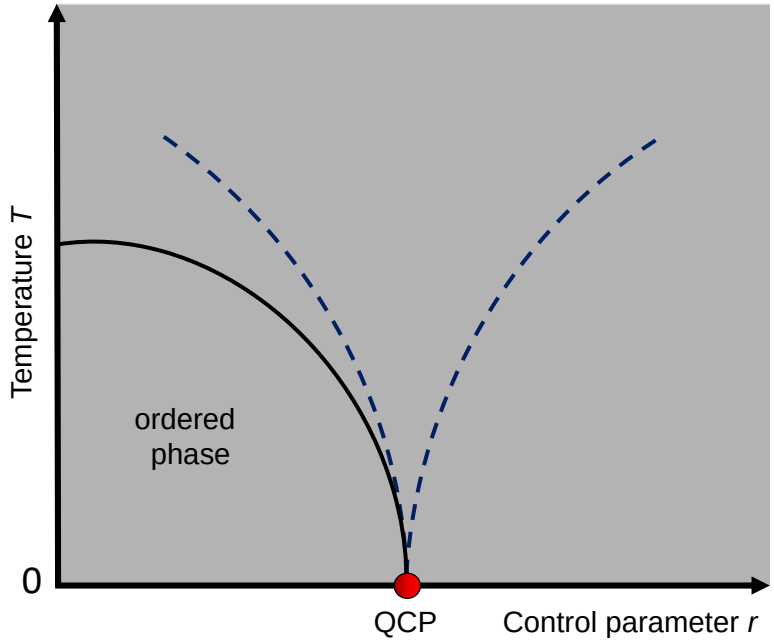

Figure 2.3: Schematic phase diagram temperature T *versus* control parameter r indicating a quantum critical point (red) at zero temperature, an ordered phase at low temperatures and the crossover temperatures represented by the dashed lines. Figure adapted from Ref. [13].

The quantum phase transitions (QPT) are non temperature-driven phase transitions and occurs at $T = 0\,\mathrm{K}$ [9], different from the classical one driven by the temperature T [14]. The so-called quantum critical point (QCP) is where the quantum phase transition takes place. The quantum phase transition is driven by the so-called control parameter r, such as pressure, external magnetic field or doping.

One way to experimentally detect a quantum phase transition is associated with the divergence of the Grüneisen parameter, namely the ratio between the thermal expansion and the specific heat [13, 15]. In a magnetic-field-induced quantum phase transition, namely the magneto-caloric effect, the magnetic Grüneisen parameter diverges, associated with a sign change of the magnetic Grüneisen parameter near a quantum critical point [16].

The fundamental aspects of the Grüneisen parameter and the magneto-caloric effect are discussed in the next sections.

2.6 The Grüneisen parameter

Regarding the volumetric thermal expansion β [17]:

$$\beta = \frac{1}{V_0}\left(\frac{\partial V}{\partial T}\right)_P, \tag{2.114}$$

where V_0 is the initial volume and V the volume at a certain temperature T. The volumetric thermal expansion is the sum of the linear thermal expansion from the a, b and c-axes, determined by the expression:

$$\beta = \alpha_a + \alpha_b + \alpha_c, \tag{2.115}$$

where α_a, α_b and α_c are the linear thermal expansion coefficient of the a, b and c-axes respectively. For the sake of completeness, the linear thermal expansion coefficient expression is recalled, given by:

$$\alpha = \frac{1}{l_0}\left(\frac{\partial l}{\partial T}\right)_P. \tag{2.116}$$

It is possible to relate the isothermal compressibility κ_T with β by the form:

$$\beta = \underbrace{-\frac{1}{V}\left(\frac{\partial V}{\partial P}\right)_T}_{\kappa_T} \cdot \left(\frac{\partial P}{\partial T}\right)_V \tag{2.117}$$

It is possible to write the expression for β by the alternative form:

$$\beta = \kappa_T \left[\frac{\partial}{\partial V}\underbrace{\left(-\frac{\partial F}{\partial T}\right)_V}_{S}\right]_T = \kappa_T \left(\frac{\partial S}{\partial V}\right)_T. \tag{2.118}$$

Also, a relation between β and the specific heat as well. The specific heat expression is given by:

$$C_V = -T\left(\frac{\partial^2 F}{\partial T^2}\right)_V = -T\left[\frac{\partial}{\partial T}\underbrace{\left(\frac{\partial F}{\partial T}\right)_V}_{-S}\right]_V = T\left(\frac{\partial S}{\partial T}\right)_V. \tag{2.119}$$

Inserting Equation 2.119 into Equation 2.118:

$$\beta = -\kappa_T \cdot \underbrace{\left(\frac{\partial S}{\partial T}\right)_V}_{C_V/T} \cdot \left(\frac{\partial T}{\partial V}\right)_S, \tag{2.120}$$

$$\beta = -\frac{\kappa_T \cdot C_V}{T} \cdot \left(\frac{\partial T}{\partial V}\right)_S. \tag{2.121}$$

Multiplying Equation 2.121 by V/V:

$$\beta = -\frac{\kappa_T \cdot C_V}{T} \cdot \left(\frac{\partial T}{\partial V}\right)_S \frac{V}{V} = -\kappa_T \cdot C_V \frac{1}{V} \underbrace{\frac{V}{T}\left(\frac{\partial T}{\partial V}\right)_S}_{\frac{\partial \ln T}{\partial \ln V}}. \tag{2.122}$$

So:

$$\beta = \underbrace{-\left(\frac{\partial \ln T}{\partial \ln V}\right)_S}_{\Gamma} \frac{1}{V} \cdot \kappa_T \cdot C_V = \frac{\kappa_T \cdot C_V}{V}\Gamma \tag{2.123}$$

where Γ is the so-called Grüneisen parameter. It can also be expressed by:

$$\Gamma = \frac{\alpha}{c_B}, \tag{2.124}$$

where c_B is the molar specific heat.

The volumetric thermal expansion microscopic contributions are the phononic, electronic and magnetic. So, it is possible to write:

$$\beta = \beta_{\text{phononic}} + \beta_{\text{electronic}} + \beta_{\text{magnetic}}, \tag{2.125}$$

where β_{phononic}, $\beta_{\text{electronic}}$ and β_{magnetic} are respectively the phononic, electronic and magnetic contributions to the volumetric thermal expansion. Comparing Equations 2.125 and 2.123 it is possible to write:

$$\beta = \frac{\kappa_T}{V}(\Gamma_{\text{phononic}} C_{\text{phononic}} + \Gamma_{\text{electronic}} C_{\text{electronic}} + \Gamma_{\text{magnetic}} C_{\text{magnetic}}), \tag{2.126}$$

where Γ_{phononic}, $\Gamma_{\text{electronic}}$ and Γ_{magnetic} are the respectively Grüneisen parameters.

In this particular Master Thesis, emphasis will be given to the magnetic Grüneisen parameter Γ_{magnetic} or the so-called magneto-caloric effect.

2.6.1 The magneto-caloric effect (the magnetic Grüneisen parameter)

The so-called magneto-caloric effect Γ_{mag} (or the magnetic Grüneisen parameter) is defined if the control parameter of a quantum phase transition is not the pressure but an external magnetic field B. In this case, the Grüneisen ratio is given by [13]:

$$\Gamma_{mag} = -\frac{(\partial M/\partial T)_B}{c_B}, \tag{2.127}$$

where M is the magnetization per mole and c_B is the molar specific heat. The molar specific heat is given by the form:

$$c = \frac{\Delta Q}{\Delta T} \quad ; \quad dQ = TdS,$$

$$c = T\left(\frac{\partial S}{\partial T}\right)_B. \tag{2.128}$$

Also, the magnetization can be given by the expression:

$$M = -\left(\frac{\partial F}{\partial B}\right)_T.$$

Deriving the magnetization over the temperature:

$$\left(\frac{\partial M}{\partial T}\right) = \frac{\partial}{\partial T}\left(-\frac{\partial F}{\partial B}\right) = \frac{\partial}{\partial B}\underbrace{\left(-\frac{\partial F}{\partial T}\right)}_{S} = \left(\frac{\partial S}{\partial B}\right)_T. \tag{2.129}$$

Replacing Equations 2.128 and 2.129 into Equation 2.127:

$$\Gamma_{mag} = -\frac{(\partial S/\partial B)_T}{T \cdot (\partial S/\partial T)_B} = -\frac{1}{T}\frac{(\partial S/\partial B)_T}{(\partial S/\partial T)_B}. \tag{2.130}$$

Equation 2.130 relates the variation of the entropy S in respect to the temperature T and the magnetic field B. This equation was employed in the next section in order to calculate the magneto-caloric effect for the Brillouin paramagnet model. Also, it is possible to rewrite Equation 2.130 by the form:

$$\Gamma_{mag} = -\frac{1}{T}\frac{(\partial S/\partial B)_T}{(\partial S/\partial T)_B} = -\frac{1}{T}\cdot\left(\frac{\partial S}{\partial B}\right)_T\cdot\left(\frac{\partial T}{\partial S}\right)_B = \boxed{\frac{1}{T}\left(\frac{\partial T}{\partial B}\right)_S}. \tag{2.131}$$

From Equation 2.131 it is clear that the magneto-caloric effect Γ_{mag} determines a change in the temperature T in response to an adiabatic (constant entropy S) change of the magnetic field B.

2.6.2 Results and discussion (Brillouin paramagnet)

Considering the Brillouin paramagnet and $J = 1/2$, it is possible to calculate the magnetocaloric effect (Γ_{mag}) by the expression [13]:

$$\Gamma_{mag} = -\frac{1}{T}.\frac{(\partial S/\partial B)_T}{(\partial S/\partial T)_B}, \tag{2.132}$$

where the entropy S is given by [1]:

$$S(T,B) = nk_B\left\{\ln\left[2\cosh\left(\frac{\mu_B B}{k_B T}\right)\right] - \frac{\mu_B B}{k_B T}\tanh\left(\frac{\mu_B B}{k_B T}\right)\right\}.$$

Deriving the entropy in respect to B:

$$\left(\frac{\partial S}{\partial B}\right)_T = nk_B\left\{\frac{1}{2\cosh\left(\frac{\mu_B B}{k_B T}\right)}\left[2\sinh\left(\frac{\mu_B B}{k_B T}\right)\frac{\mu_B}{k_B T}\right] - \left[\frac{\mu_B}{k_B T}\tanh\left(\frac{\mu_B B}{k_B T}\right) + \frac{\mu_B B}{k_B T}\frac{1}{\cosh^2\left(\frac{\mu_B B}{k_B T}\right)}\frac{\mu_B}{k_B T}\right]\right\}$$

$$\left(\frac{\partial S}{\partial B}\right)_T = nk_B\left\{\cancel{\tanh\left(\frac{\mu_B B}{k_B T}\right)\frac{\mu_B}{k_B T}} - \cancel{\tanh\left(\frac{\mu_B B}{k_B T}\right)\frac{\mu_B}{k_B T}} - \frac{{\mu_B}^2 B}{{k_B}^2 T^2\cosh^2\left(\frac{\mu_B B}{k_B T}\right)}\right\}.$$

Therefore,

$$\left(\frac{\partial S}{\partial B}\right)_T = -\frac{nB\mu_B^2}{k_B T^2\cosh^2\left(\frac{\mu_B B}{k_B T}\right)}. \tag{2.133}$$

Analogously,

$$\left(\frac{\partial S}{\partial T}\right)_B = nk_B\left\{\frac{1}{2\cosh\left(\frac{\mu_B B}{k_B T}\right)}\left[2\sinh\left(\frac{\mu_B B}{k_B T}\right)\left(-\frac{\mu_B B}{k_B T^2}\right)\right] - \left[\left(-\frac{\mu_B B}{k_B T^2}\right)\tanh\left(\frac{\mu_B B}{k_B T}\right) + \left(\frac{\mu_B B}{k_B T}\right)\frac{1}{\cosh^2\left(\frac{\mu_B B}{k_B T}\right)}\left(-\frac{\mu_B B}{k_B T^2}\right)\right]\right\}.$$

$$\left(\frac{\partial S}{\partial T}\right)_B = nk_B\left\{\cancel{-\tanh\left(\frac{\mu_B B}{k_B T}\right)\left(\frac{\mu_B B}{k_B T^2}\right)} + \cancel{\tanh\left(\frac{\mu_B B}{k_B T}\right)\left(\frac{\mu_B B}{k_B T^2}\right)} + \frac{{\mu_B}^2 B^2}{{k_B}^2 T^3\cosh^2\left(\frac{\mu_B B}{k_B T}\right)}\right\}.$$

Therefore,

$$\left(\frac{\partial S}{\partial T}\right)_B = \frac{n{\mu_B}^2 B^2}{k_B T^3\cosh^2\left(\frac{\mu_B B}{k_B T}\right)}. \tag{2.134}$$

Replacing Equations (2.133) and (2.134) into (2.132):

$$\Gamma_{mag} = -\frac{-\frac{nB{\mu_B}^2}{k_B T^2 \cosh^2\left(\frac{\mu_B B}{k_B T}\right)}}{\frac{n{\mu_B}^2 B^2}{k_B T^2 \cosh^2\left(\frac{\mu_B B}{k_B T}\right)}}.$$

Resulting:

$$\boxed{\Gamma_{mag} = \frac{1}{B}}. \tag{2.135}$$

From Equation 2.135 one can directly conclude that the Brillouin paramagnet can be considered intrinsically quantum critical to $B \to 0$. In other words, Γ_{mag} diverges as $B \to 0$, a fingerprint of a quantum phase transition [13, 15, 18].

Also, it is possible to calculate the magneto-caloric effect for general values of J. The Helmholtz free energy for n spins per unit of volume is given by:

$$F = -nk_B T \ln[Z_J(y)], \tag{2.136}$$

where $Z_J(y)$ is the partition function, given by:

$$Z_J(y) = \frac{\sinh[(2J+1)\frac{y}{2J}]}{\sinh[\frac{y}{2J}]}, \tag{2.137}$$

where $y = g_J \mu_B JB/k_B T$.

Thus, the Helmholtz free energy is:

$$F = -nk_B T \ln\left(\frac{\sinh\left[\frac{(2J+1)g_J\mu_B B}{2k_B T}\right]}{\sinh\left[\frac{g_J\mu_B B}{2k_B T}\right]}\right). \tag{2.138}$$

From Equation 2.138, the entropy S can be calculated by the form:

$$S = -\left(\frac{\partial F}{\partial T}\right)_B. \tag{2.139}$$

$$S = -\left[-nk_B \ln\overbrace{\left(\frac{\sinh\left[\frac{(2J+1)g_J\mu_B B}{2k_B T}\right]}{\sinh\left[\frac{g_J\mu_B B}{2k_B T}\right]}\right)}^{Z_J(y)}\right] - [\Theta], \tag{2.140}$$

where Θ is:

$$\Theta = -nk_B T \frac{\sinh\left[\frac{g_J\mu_B B}{2k_B T}\right]}{\sinh\left[\frac{(2J+1)g_J\mu_B B}{2k_B T}\right]} \cdot \left\{\frac{\sinh\left[\frac{g_J\mu_B B}{2k_B T}\right]\cosh\left[\frac{(2J+1)g_J\mu_B B}{2k_B T}\right]\left(-\frac{(2J+1)g_J\mu_B B}{2k_B T^2}\right) - \sinh\left[\frac{(2J+1)g_J\mu_B B}{2k_B T}\right]\cosh\left[\frac{g_J\mu_B B}{2k_B T}\right]\left(-\frac{g_J\mu_B B}{2k_B T^2}\right)}{\sinh^2\left[\frac{g_J\mu_B B}{2k_B T}\right]}\right\}.$$

$$\Theta = -nk_B T \cdot \left[\frac{\sinh\left[\frac{g_J\mu_B B}{2k_B T}\right]}{\sinh\left[\frac{(2J+1)g_J\mu_B B}{2k_B T}\right]} \cdot \frac{\cosh\left[\frac{(2J+1)g_J\mu_B B}{2k_B T}\right]}{\sinh\left[\frac{g_J\mu_B B}{2k_B T}\right]} \cdot \left(-\frac{(2J+1)g_J\mu_B B}{2k_B T^2}\right) - \frac{\sinh\left[\frac{g_J\mu_B B}{2k_B T}\right]}{\sinh\left[\frac{(2J+1)g_J\mu_B B}{2k_B T}\right]} \cdot \frac{\sinh\left[\frac{(2J+1)g_J\mu_B B}{2k_B T}\right] \cdot \cosh\left[\frac{g_J\mu_B B}{2k_B T}\right] \cdot \left(-\frac{g_J\mu_B B}{2k_B T^2}\right)}{\sinh^2\left[\frac{g_J\mu_B B}{2k_B T}\right]}\right].$$

$$\Theta = \overbrace{-nk_BT\left\{\coth\left[\frac{(2J+1)g_J\mu_BB}{2k_BT}\right]\cdot\left(-\frac{(2J+1)g_J\mu_BB}{2k_BT^2}\right)-\left(-\frac{g_J\mu_BB}{2k_BT^2}\right)\cdot\coth\left[\frac{g_J\mu_BB}{2k_BT}\right]\right\}}^{-y\cdot B_J(y)}.$$

$$\Theta = -nk_B\cdot y\overbrace{\left[\frac{(2J+1)}{2J}\coth\left[\frac{(2J+1)}{2J}\cdot y\right]-\frac{1}{2J}\cdot\left[\frac{y}{2J}\right]\right]}^{B_J(y)} = -nk_BTB_J(y)\cdot y.$$

Replacing Θ into 2.140:

$$\boxed{S(y) = nk_B\cdot[\ln Z_J(y) - yB_J(y)]}. \tag{2.141}$$

Now, it is possible to calculate:

$$\left(\frac{\partial S}{\partial B}\right)_T = \left\{\frac{\left[\frac{(2J+1)g_J\mu_B}{2k_BT}\right]^2\cdot nk_BB}{\sinh^2\left[\frac{(2J+1)g_J\mu_BB}{2k_BT}\right]} - \frac{\left[\frac{g_J\mu_B}{2T}\right]^2\cdot nk_BB}{\sinh^2\left[\frac{g_J\mu_BB}{2k_BT}\right]}\right\}. \tag{2.142}$$

and

$$\left(\frac{\partial S}{\partial T}\right)_B = \left\{\frac{\left[\frac{g_J\mu_BB}{2k_BT}\right]^2\cdot\frac{nk_B}{T}}{\sinh^2\left[\frac{g_J\mu_BB}{2k_BT}\right]} - \frac{\left[\frac{(2J+1)g_J\mu_BB}{2k_BT}\right]^2\cdot\frac{nk_B}{T}}{\sinh^2\left[\frac{(2J+1)g_J\mu_BB}{2k_BT}\right]}\right\}. \tag{2.143}$$

Replacing Equations 2.142 and 2.143 into 2.132:

$$\Gamma_{mag} = \frac{-\left\{\frac{\left[\frac{(2J+1)g_J\mu_B}{2k_BT}\right]^2\cdot nk_BB}{\sinh^2\left[\frac{(2J+1)g_J\mu_BB}{2k_BT}\right]} - \frac{\left[\frac{g_J\mu_B}{2T}\right]^2\cdot nk_BB}{\sinh^2\left[\frac{g_J\mu_B}{2k_BT}\right]}\right\}}{T\cdot\left\{\frac{\left[\frac{g_J\mu_BB}{2k_BT}\right]^2\cdot\frac{nk_B}{T}}{\sinh^2\left[\frac{g_J\mu_BB}{2k_BT}\right]} - \frac{\left[\frac{(2J+1)g_J\mu_BB}{2k_BT}\right]^2\cdot\frac{nk_B}{T}}{\sinh^2\left[\frac{(2J+1)g_J\mu_BB}{2k_BT}\right]}\right\}}. \tag{2.144}$$

$$\Gamma_{mag} = \frac{\cancel{nk_B}\cdot B\left\{\frac{\left[\frac{g_J\mu_B}{2k_BT}\right]^2}{\sinh^2\left[\frac{g_J\mu_BB}{2k_BT}\right]} - \cancel{\frac{\left[\frac{(2J+1)g_J\mu_B}{2k_BT}\right]^2}{\sinh^2\left[\frac{(2J+1)g_J\mu_BB}{2k_BT}\right]}}\right\}}{\cancel{nk_B}\cdot B^2\left\{\frac{\left[\frac{g_J\mu_B}{2k_BT}\right]^2}{\sinh^2\left[\frac{g_J\mu_BB}{2k_BT}\right]} - \cancel{\frac{\left[\frac{(2J+1)g_J\mu_B}{2k_BT}\right]^2}{\sinh^2\left[\frac{(2J+1)g_J\mu_BB}{2k_BT}\right]}}\right\}} = \frac{B}{B^2}. \tag{2.145}$$

Thus:

$$\boxed{\Gamma_{mag} = \frac{1}{B}}. \tag{2.146}$$

From Equation 2.146 it can be concluded that Γ_{mag} diverges as $B \to 0\,\mathrm{T}$, a fingerprint of a quantum phase transition [13]. Thus, although the Brillouin model is purely classical, there is an intrinsic quantum critical-like behavior at $T = 0\,\mathrm{K}$ for the particular case of $B = 0\,\mathrm{T}$. For both positive and negative infinitesimal values of B, Γ_{mag} diverges. The sign change in the magneto-caloric effect is also a fingerprint of a quantum phase transition [13, 15, 18].

Chapter 3

Superconductivity

In this chapter, current and fundamental aspects of superconductivity are presented. An analysis of the high-temperature superconductors are performed and the binary alloy $FeSe_{1-x}$ is introduced in this context.

3.1 Introduction

One of the main goals of exploring low-temperature Physics is the fact that exotic phenomena emerge when a sufficiently low temperature is achieved. One of the most investigated properties of matter in low temperatures is superconductivity, where the resistance of a determined system goes to zero at a critical temperature T_c. In other words, there is a current flow without energy dissipation by the Joule effect ($P = Ri^2$), where P is the power dissipated, R is the resistance and i the electrical current.

After several years since Kamerlingh Onnes [19] first observed superconductivity in a mercury (Hg) sample with $T_c \sim 4\,\mathrm{K}$, Meissner and Ochsenfeld [20] demonstrated experimentally the Meissner-Ochsenfeld effect, where a magnetic field is expelled from a superconductor in the so-called magnetic levitation. Such effect is crucial in defining superconductivity as a new state of matter. This phenomenon is so counter-intuitive that more than half-century passed since the BCS theory [21] was developed, which proposed the electron-electron coupling by the phonon of the lattice in the so-called Cooper pairs.

There is a technological interest into synthesizing superconducting materials with higher critical temperatures since it would boost such industry with non-dissipative materials. Most metallic elements were discovered to superconduct below 10 K and even a group of metal alloys have shown superconductivity. However, until the 80's temperatures above 30 K had not been observed, as shown in Fig 3.1. In 1986 Bednorz and Müller observed for the first time superconductivity in the so-called cuprates (alloys containing copper and oxygen) above the 30 K range [22]. Less than one year after, $YBa_2Cu_3O_{7-x}$ (YBCO) presented a critical temperature of 90 K being above the liquid N_2 range. In the last decade, superconductivity was discovered in iron-based structures, the so-called iron pnictides or iron-based superconductor (IBSC) [23]. Such discovery was unexpected for two main reasons: the magnetic ions would destroy superconductivity and the non-superconducting phases of this family are metallic, totally different from the cuprate families which were insulating.

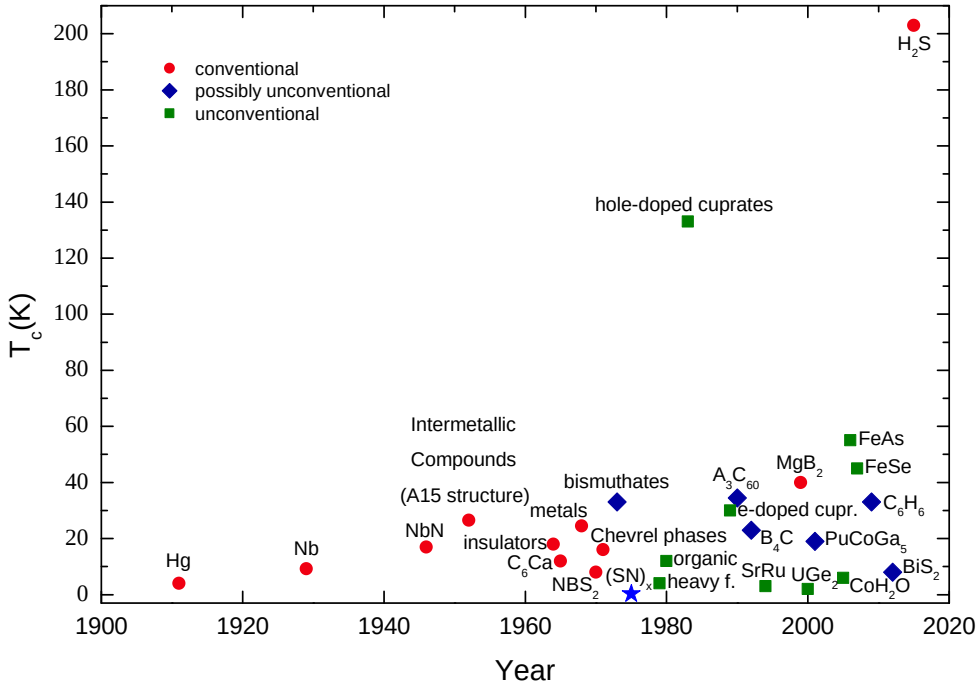

Figure 3.1: Increasing of the critical temperature T_c over the years of conventional, possibly unconventional and unconventional superconductors [24].

The idea is still in development but years of collective effort revealed that the Physics of Fe-based superconductors is way richer than foreseen and they feature a few unique properties. The discovery of IBSC has also added more degrees of freedom for theoretical work since the non-conventional superconductivity (not explained by the BCS theory) was observed just in systems with strong electrical correlation such as cuprates, heavy fermions [25] and organic conductors [26].

The BCS theory of conventional superconductors reveals how to achieve high T_c without any upper bound combining high-frequency phonons, strong electron-phonon coupling and high density of states [27]. Such conditions are satisfied for compounds dominated by hydrogen [28, 29] since it has such characteristics, predicting compounds with T_c in the range of 50−235 K for numerous hydrides [30], since the hydrogen mass is low and it would increase the angular frequency w and thus the critical temperature T_c. Yet, the hydrogen sulfide compound H_2S was discovered to be the T_c record history (203 K) under high-pressure [31].

Another fascinating discovery was that a double-stranded DNA [32] can superconduct. Regarding the electrical transport properties of DNA, it was predicted that it would be conducting [33, 34] and insulating [35, 36].

Several thousands superconductors are known in the literature and, as new systems emerge, new theories are being developed and not always are in accordance with the existent ones. Every single new theory that explains one system or a gama of systems is one step closer to the unification of them all into a single theory that could definitively explain superconductivity. Besides all discoveries regarding superconductivity, there are very much to understand how this quantum effect works and how it can be fully understood. The search for a room-temperature superconductor happens every day in all over the globe due to its magnificent application in technology that will result in a huge advance in science.

3.2 Materials of interest

Regarding electron systems, with the discovery of superconductivity in the last decades in heavy fermions systems [37], copper oxides (cuprates) [38] and organic conductors

[26], it became evident that spectacular forms of collective behavior emerge in strongly correlated electronic systems.

For example, when the Coulomb energy interaction is comparable or higher than the kinetic energy of a study system, a Mott insulator state can emerge. In such systems, the interplay between the charge degrees of freedom (spin), lattice and orbitals originates very rich phase diagrams. Stands out the emergence of a superconducting phase from a Mott insulator state [39], applying external pressure or doping, as observed in organic conductors [40] and cuprates [41], respectively.

There is a very interesting class of materials discovered by the scientific community in the last years: iron-based superconductors [42]. Even more interesting is the fact that since the discovery of superconducting cuprates, this class of materials constitutes the first generation of superconductors with critical temperatures above 50 K [43]. In particular, the binary alloy $FeSe_{1-x}$ offers unique opportunities to study superconductivity in this class of materials [44] and is the alloy focused in this Master Thesis.

3.3 The binary alloy $FeSe_{1-x}$

The observation of superconductivity in alloys containing the element iron (Fe) is counterintuitive since the description of the pairing mechanism based on the BCS [21] theory refers the formation of triplets (originated from the $3d$ electrons moment of the Fe atoms) would annihilate the Cooper pairs. In this regard, $FeSe_{1-x}$ represents an alloy of great interest, since its T_c can be raised by external applied hydrostatic pressure from 8.5 K to 36.7 K [45]. Also, thin films of $FeSe_{1-x}$ deposited in $SrTiO_3$ substrates showed superconductivity with $T_c \sim 100$ K [46]. In this context, there are two phases of interest for the $FeSe_{1-x}$ alloy: the tetragonal and hexagonal crystalline structures.

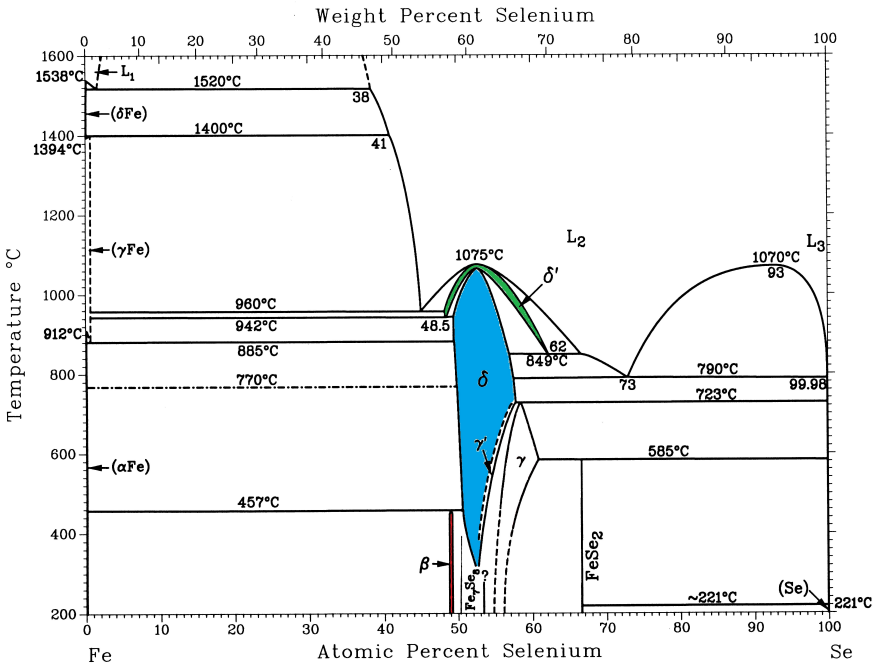

Figure 3.2: Phase diagram temperature *versus* atomic concentration for the binary alloy $FeSe_{1-x}$. It is possible to observe the various phases of FeSe including the ones of interest: δ' (green - tetragonal unit cell) and δ (blue - hexagonal unit cell) [47].

As the temperature is reduced, the electrical resistivity of the tetragonal phase sample goes to zero near T_c, i.e., it superconducts below T_c, as can be seen in Figure 3.4.

However, for the hexagonal phase, a semiconducting behavior is predicted ($\mathrm{d}R/\mathrm{d}T < 0$), as can be seen in Figure 3.5.

Also, the crystallography planes of the tetragonal phase of $FeSe_{1-x}$ are separated by the so-called van der Waals gap (Figure 3.3), which allows the material to be extremely

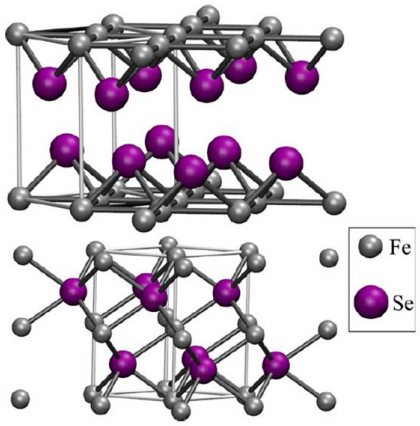

Figure 3.3: Unit cells of the tetragonal (up) and hexagonal (lower) phases of $FeSe_{1-x}$. Note that in the tetragonal unit cell there is empty space between the atoms of Se (purple) denominated as van der Waal's gap.

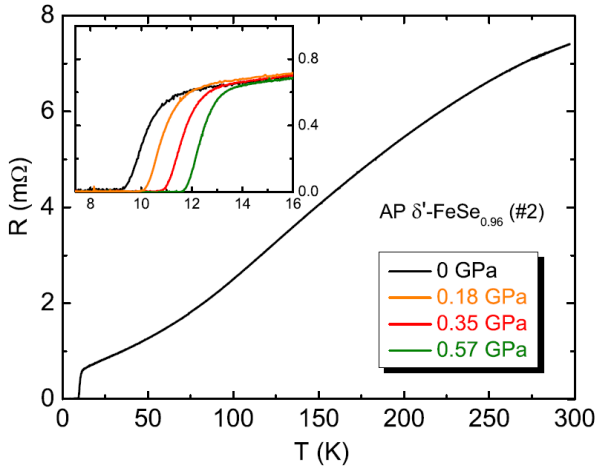

Figure 3.4: Main panel: electric resistance measurement as a function of temperature for the δ'-$FeSe_{0,96}$ with $T_c = 8.5\,K$. Inset: electric resistance measurements at low temperatures as a function of external hydrostatic pressure applied, note that there is a significantly increase of T_c with application of pressure [48].

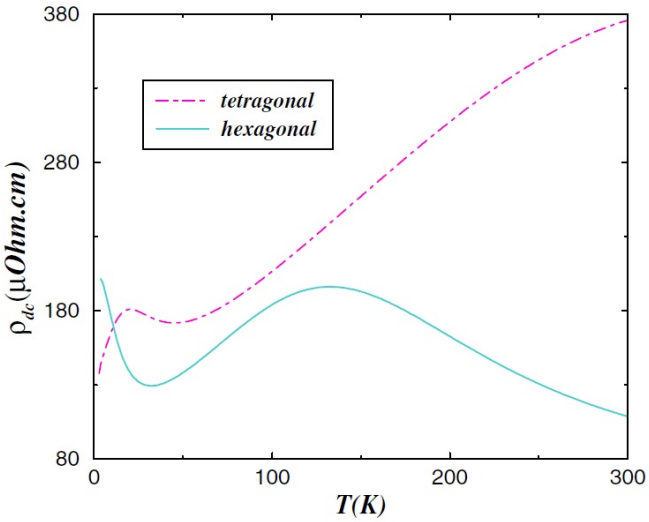

Figure 3.5: Electric resistivity as a function o temperature for the δ phase (continuous line) and for the δ' one (dotted line) of the $FeSe_{1-x}$ as theoretically predicted in Ref. [49].

compressible. Such property is strongly associated with the increase of T_c from 8.5 K to 36.7 K under hydrostatic pressure [45].

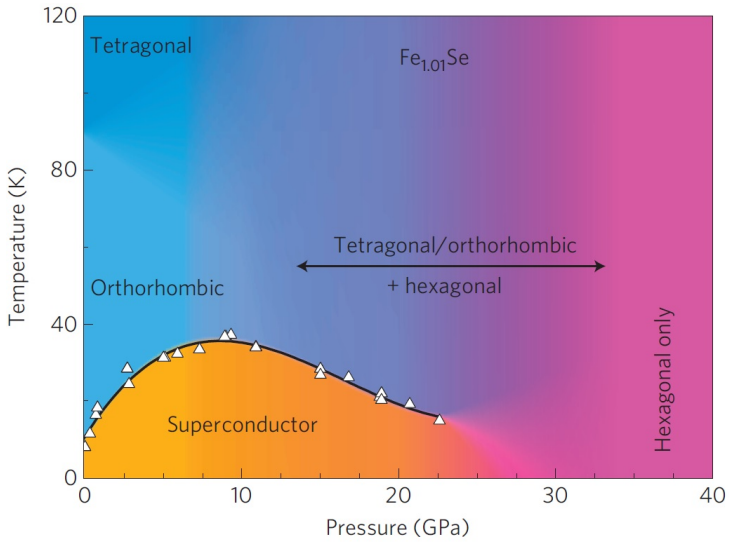

Figure 3.6: Without applied pressure, the binary alloy $FeSe_{1-x}$ is structurally distorted from orthogonal to orthorhombic at 90 K. The maximum value of T_c is observed at 36.7 K under 8.9 GPa applied pressure. At high pressures, the alloy is uniquely at the hexagonal phase and presents a semiconducting behavior [45].

3.3.1 The synthesis of $FeSe_{1-x}$

The main goal in this Master Thesis was to synthesize single-crystals of δ-$FeSe_{1-x}$ in order to perform systematic transport investigations in this phase comparing with the δ'-$FeSe_{1-x}$, which is already intensively investigated in literature, aiming to understand the fundamental concepts that annihilates superconductivity in the δ-$FeSe_{1-x}$.

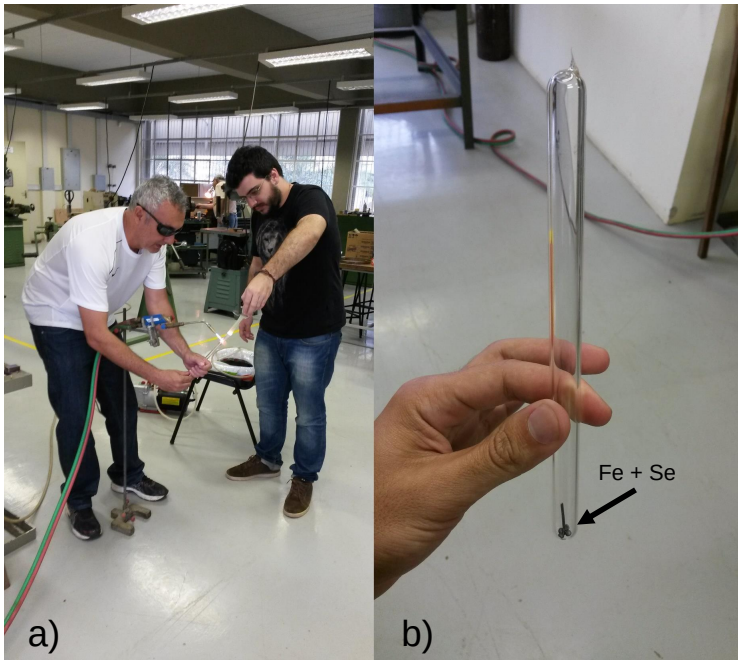

Figure 3.7: a) After the pump and purge with nitrogen, the ampoule was sealed employing a torch. Special thanks to Geraldo Aparecido de Lima Sobrinho for the technical support. b) After the sealing the ampoule is ready to be inserted into the furnace for the proper thermal treatment.

In order to synthesize single crystals of δ-$FeSe_{1-x}$, the following stoichiometry was employed regarding the phase diagram in Figure 3.2:

$$0.52\text{Fe} + 0.48\text{Se} \rightarrow 1.00\delta\text{-FeSe}_{1-x}.$$

From the molar mass of both Fe (55.84 g/mol) and Se (78.96 g/mol), it was possible to calculate the mass of the compound to be reacted. Such appropriate mixture of Fe and

Se was inserted into a glass ampoule since it can withstand temperatures until $\sim 400^{o}$C without any significant changes in their mechanical resistance. A pump and purge with nitrogen was performed in order to maintain an inert atmosphere inside the ampoule. Then, the ampoule was carefully sealed employing a torch (Figure 3.7a)).

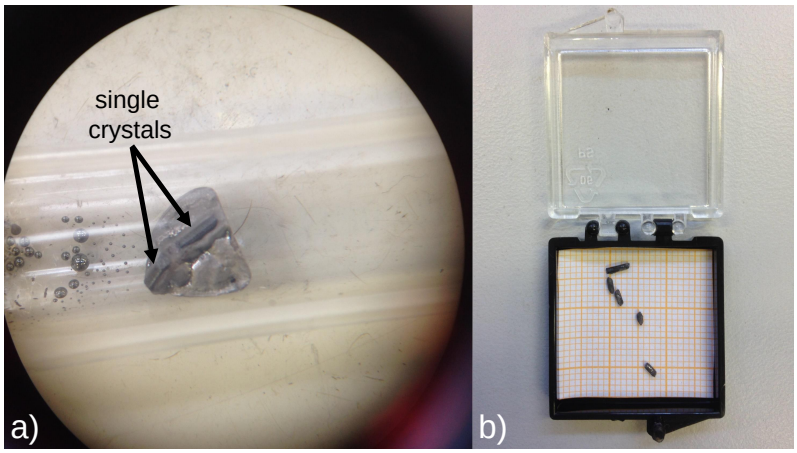

Figure 3.8: a) After the ampoule was cooled to room-temperature, it was possible to observe the formation of single crystals in the solidified mixture of Fe and Se. b) The single crystals were collected and stored properly.

The glass ampoule containing the mixture was then inserted into a horizontal furnace and the temperature is varied from room-temperature to $\sim 400^{o}$C, which remains at such temperature for a couple of hours. After this process, the ampoule was cooled to room-temperature, carefully broken and the single crystals were collected, as can be seen in Figure 3.8.

Thereon, a couple of samples were sent to x-ray measurements to determine whether or not a pure phase of δ-$FeSe_{1-x}$ was achieved. The x-ray measurements results are discussed in the next section.

3.3.2 Experimental Results

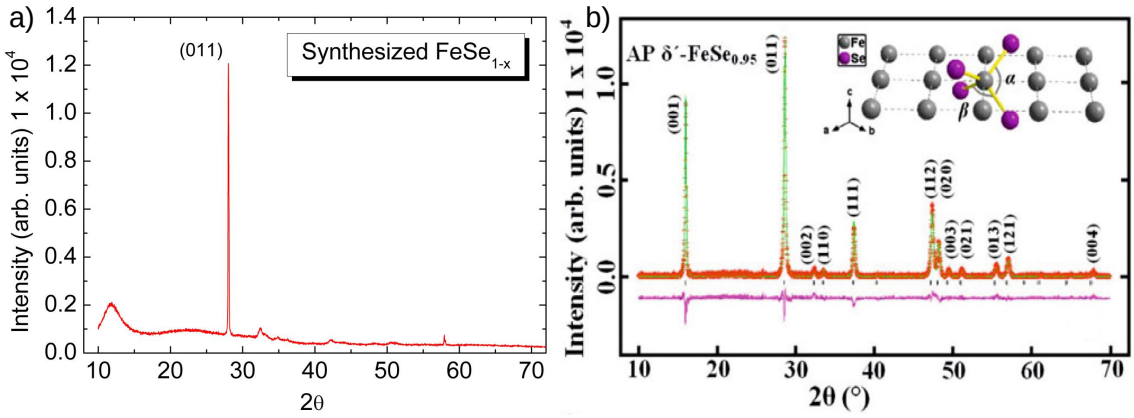

Figure 3.9: a) Room-temperature intensity *versus* 2θ for one sample synthesized, aiming to achieve an homogeneous hexagonal phase of the hexagonal phase of $FeSe_{1-x}$. One of the Miller indices (011) is shown in order to compare with X-ray results from the tetragonal structure. The X-ray experiment was carried out by M. Sc. Paulo Eduardo Menegasso Filho at the State University of Campinas; b) Room-temperature intensity *versus* 2θ for the tetragonal phase of $FeSe_{0.95}$ [48] with their respective Miller indices. The base lines are shown for comparison between the X-ray results and the calculated ones. Inset: cut of the tetragonal $FeSe_{1-x}$ crystal structures.

After employing the solid-state physics reaction in order to obtain single crystals of the hexagonal phase of $FeSe_{1-x}$, the ampoules were opened and the single crystals collected.

In order to confirm the homogeneity of the hexagonal structure, x-ray experiments were carried out in such samples.

Comparing the X-ray results from the synthesized samples with the tetragonal one already reported in literature [48], it is possible to observe the Miller indices (011) in the synthesized sample X-ray, indicating that a homogeneous phase of the hexagonal structure was not achieved since it indicates traces of the tetragonal structure into the sample.

Although a homogeneous phase of the hexagonal binary alloy $FeSe_{1-x}$ was not achieved, the understanding of both solid-state synthesis and the thermodynamics therein contributed expressively for my scientific career. Such knowledge can be extended to projects to be performed in a near future.

Chapter 4

Correlation phenomena in the $(TMTTF)_2X$ (X = PF_6-H_{12}, PF_6-D_{12}) Fabre-salts

In this section are presented the theoretical aspects of the exotic properties of the $(TMTTF)_2X$ salts, which are crucial to understanding both theoretical and experimental studies. The goal is to understand the theory, namely the extended Hubbard model, which enables the understanding of the ferroelectric Mott-Hubbard phase, which is the main topic of the experimental results in this thesis. The physical properties of the TMTTF-based molecular conductors are discussed.

4.1 Relevant fundamental literature and theoretical aspects

Nowadays, correlation phenomena are one of the most investigated topics in the scientific community, since several exotic phenomena emerge due to the interaction between electrons. Some examples relies on the Mott-insulator phase [12, 50], superconductivity [26, 51, 52] and charge-ordering [53]. In this regard, molecular systems are very crystalline materials, which enables a proper investigation of electron-electron interactions in a *clean* environment. In particular, the molecular conductors $(TMTTF)_2X$, where TMTTF is the tetramethyltetrathiafulvalene molecule and X a monovalent counter-anion since it represents one of the most appropriate playgrounds to explore correlation effects in low dimensions. Also, the high-purity and tunability of such systems represent a rich playground for the exploration of fundamental Physics.

In such system, there is one electron per two molecules of TMTTF and they are organized in chains in the a-axis (Figure 4.3), which are dimerised since the counter-anions X (e.g. X = PF_6, AsF_6, SbF_6) have a particular way to order, occasioning inequivalent charge distribution in the system.

4.2 The Extended Hubbard model

A proper physical model employed in strong correlation systems with many particles is the extended Hubbard model [56]. The hamiltonian of the physical system is expressed by the form:

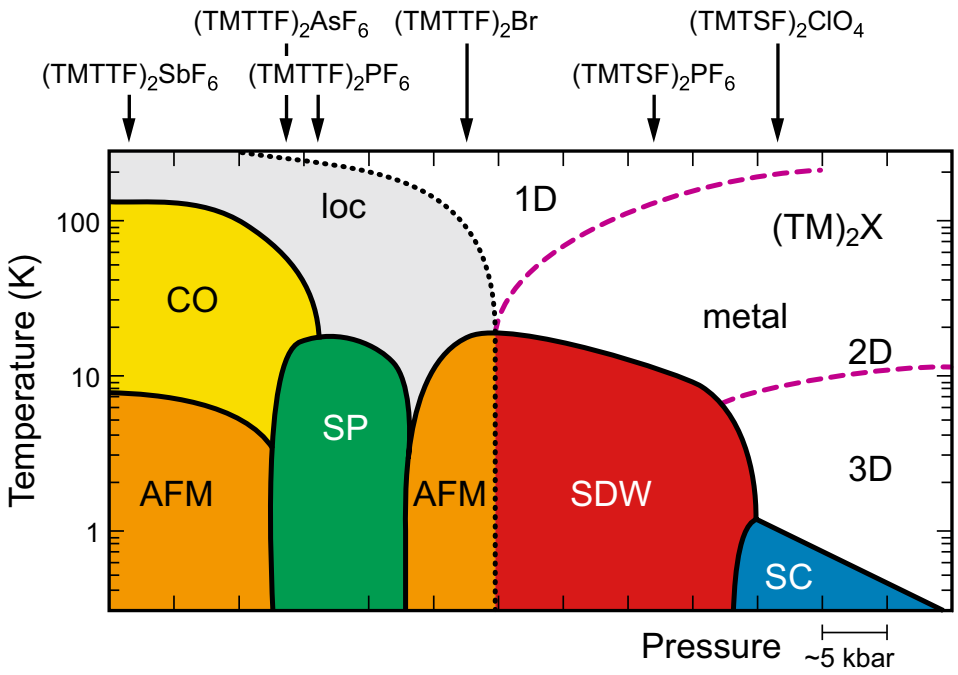

Figure 4.1: Schematic general $P - T$ phase diagram for the Fabre-Bechgaard salts. The position of the different compounds under ambient pressure are indicated above with the black arrows, such difference is directly connected with the counter-anion chemical pressure over the molecule. The phases shown are localized electrons (loc), charge-ordering (CO), antiferromagnetic (AFM), spin-Peierls (SP), spin-density wave (SP) and superconductivity (SC) [54, 55].

$$H = \sum_{i,j,\sigma} t_{i,j} c^{\dagger}_{i,\sigma} c_{j,\sigma} + U \sum_{i} n_{i,\uparrow} n_{i,\downarrow} + V \sum_{i,j} n_i n_j, \tag{4.1}$$

where $t_{i,j}$ are the transfer integrals between the crystal lattice sites' (also known as the hopping term) and are associated with the kinetic energy of the electrons, $c^{\dagger}_{i,\sigma}$ is the creation operator, which "creates" one electron with spin σ in the i site, while the $c_{j,\sigma}$ "destroys" one electron with spin σ from the j site (such operators simulate an electron "hopping" from one site j to another i and that is why the $t_{i,j}$ is called the hopping term), U is the Coulomb electronic repulsion of two electrons occupying the same site, V is the Coulomb repulsion between two electrons at neighbor sites and $n_{i,\uparrow}$ and $n_{i,\downarrow}$ represents the number operator of electrons with spin up and down, respectively.

The correlation phenomena between electrons (namely the inter-site U term) cause a splitting between the energy bands, characterizing the system as a semiconductor [54]. Such phenomenon is the so-called Mott-insulator phase or Mott metal-insulator phase transition [50].

4.3 The charge-ordered phase

Whenever the TMTTF-based molecular systems are at low temperatures (between 50−150 K) a charge-ordered phase can be achieved coexisting with a ferroelectric one [57]. Such phenomena can also be explained through the Hubbard model. In this case, when the hopping term $t_{i,j} \approx U$ the minimal energy configuration of the system is encountered by ordering the charges. However, as the V term increases, a critical value of it can be found where the minimal energy configuration is not a homogeneous charge distribution, but a charge disproportion one.

Above the charge-ordering phase temperature (T_{co}) electrons are localized without the formation of electrical dipoles, while below T_{co} there is a finite charge disproportion [58] between the molecules (above the V_c), creating electric dipoles. From such electrical

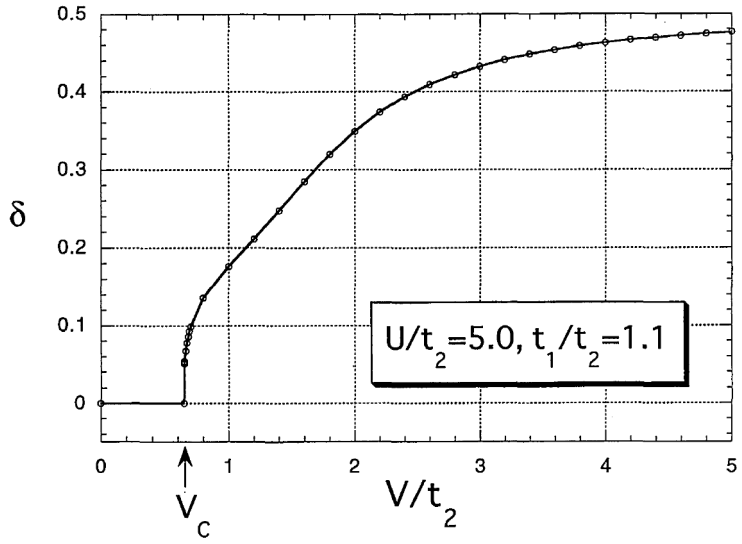

Figure 4.2: Dependence of the charge transfer σ as a function of V/t_2. After a critical inter-site value (V_c) is achieved, an inhomogeneous charge distribution takes place [56].

configuration, the ferroelectricity phase emerges, concomitant with the charge-ordering one. It is worth mentioning that a metal to Mott-insulating phase transition can be associated directly with the charge-ordering transition and can be experimentally observed in electrical resistivity measurements for several systems [53, 54, 59, 60].

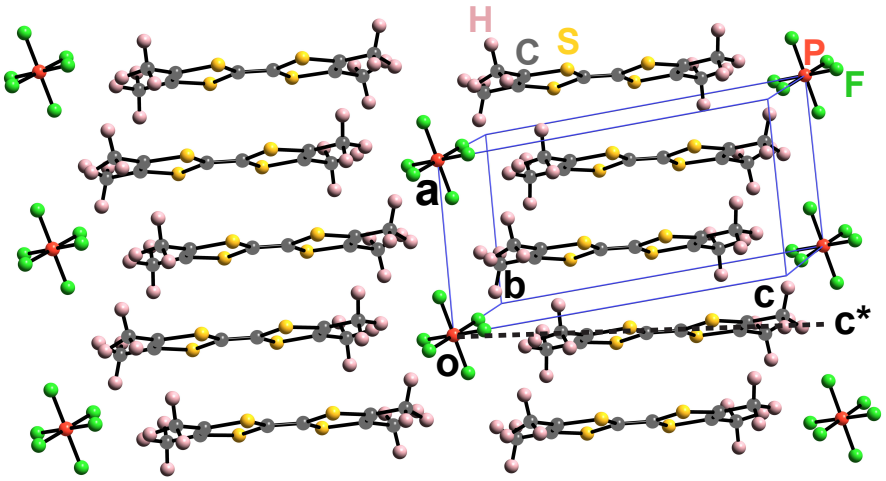

Figure 4.3: Molecular stacks structure of the $(TMTTF)_2X$, where the anion X (X = PF_6, AsF_6 or SbF_6) is represented in the octahedral structure. The triclinic unit cell is represented by the blue lines. The a, b, c and c^*-axis (dotted lines) are represented. Adapted with permission from [61].

The charge-ordering phase plays an important role in the comprehension of some exotic phenomena [62–64] and recently was recognized as well in the Physics of some molecular conductors [65, 66], such as the previously-mentioned $(TMTTF)_2X$ salts.

Another strong evidence of ferroelectricity is an anomaly (maximum) in the dimensionless dielectric constant ε' measurements for such systems, reported in the literature [57] and reproduced in this Master Thesis. Since the dielectric constant is directly associated with the polarization through the Clausius-Mossoti relation, such anomaly reveals a change in the polarization of the system, directly associated with the ferroelectric phase.

All the previously mentioned phases in this Chapter (namely, charge-ordering, and ferroelectricity) occurs simultaneously at T_{co}, in the so-called Mott-Hubbard ferroelectric phase. The exploration of this exact phase was the motivation for all the experiments carried out in this Master Thesis.

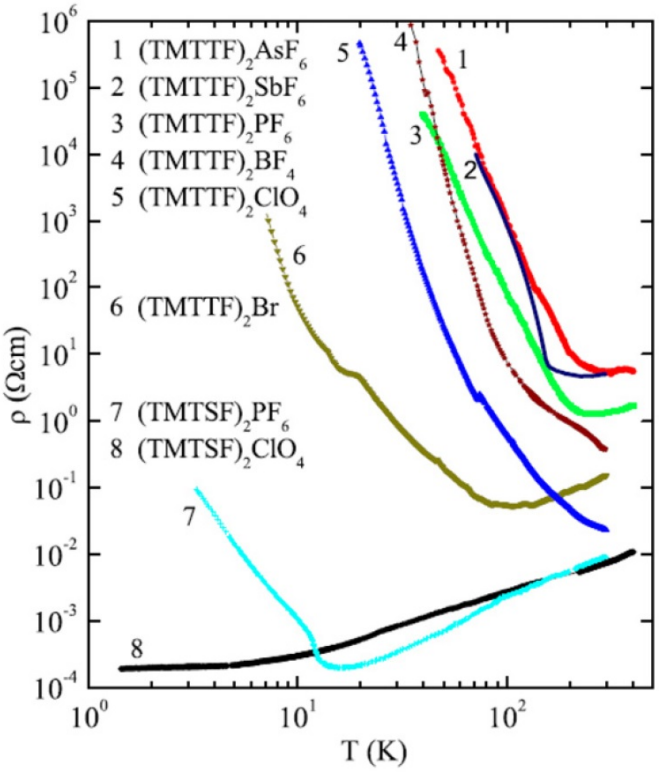

Figure 4.4: Resistivity *versus* temperature for some of the Fabre-Bechgaard salts. The change in the $d\rho/dT$ for curves 1 (AsF_6 – 102 K), 2 (SbF_6 – 157 K) and 3 (PF_6 – 67 K) is directly associated with a Mott metal-insulator transition [54].

4.4 The dielectric constant and the Clausius-Mossoti relation

The so-called dielectric constant ε relatively to vacuum is described as a function of the electrical field E by the expression [8]:

$$\varepsilon = \frac{\varepsilon_0 E + P}{\varepsilon_0 E} = 1 + \chi, \tag{4.2}$$

where ε_0 is the vacuum permittivity, P the polarization and χ the magnetic susceptibility.

The polarizability α of a single atom is directly proportional to the local dielectric field E_{local} by the form:

$$p = \alpha \cdot E_{local}, \tag{4.3}$$

where p is the electric dipole moment ($p = q \cdot l$).

The polarizability is defined in terms of a single atom and the dielectric constant defined in how such atoms are assembled to form a crystal. The polarization P of a crystal is the sum of all the atomic polarizabilities α, given by the form:

$$P = \sum_j N_j p_j = \sum_j N_j \alpha_j E_{local}(j), \tag{4.4}$$

where N_j the number of j-site atoms, α_j the polarizability of j-site atoms and $E_{local}(j)$ is the local electrical field at atoms j sites.

To relate the dielectric constant to the polarizability it is needed to relate the macroscopic electric field to the local one, by the form:

$$P = \left(\sum_j N_j \alpha_j \right) \underbrace{\left(E + \frac{P}{3\varepsilon_0} \right)}_{\text{Lorentz relation}}. \tag{4.5}$$

Solving Equation 4.5 for P:

$$P = \left(\sum_j N_j\alpha_j\right)\cdot\left(\frac{3\varepsilon_0 E + P}{3\varepsilon_0}\right),$$

$$3\varepsilon_0 P - P\left(\sum_j N_j\alpha_j\right) = 3\varepsilon_0 E\left(\sum_j N_j\alpha_j\right),$$

$$P\left[3\varepsilon_0 - \left(\sum_j N_j\alpha_j\right)\right] = 3\varepsilon_0 E\left(\sum_j N_j\alpha_j\right),$$

$$\chi = \frac{P}{\varepsilon_0 E} = \frac{3\sum_j N_j\alpha_j}{3\varepsilon_0 - (\sum_j N_j\alpha_j)} = \frac{\cancel{3}\sum_j N_j\alpha_j}{\cancel{3}[\varepsilon_0 - 1/3(\sum_j N_j\alpha_j)]}.$$

So,

$$\chi = \frac{\sum_j N_j\alpha_j}{[\varepsilon_0 - 1/3(\sum_j N_j\alpha_j)]}. \tag{4.6}$$

Combining Equations 4.6 and 4.2:

$$\varepsilon - 1 = \frac{\sum_j N_j\alpha_j}{[\varepsilon_0 - 1/3(\sum_j N_j\alpha_j)]} = \frac{3\sum_j N_j\alpha_j}{[3\varepsilon_0 - 1/3(\sum_j N_j\alpha_j)]},$$

$$(\varepsilon - 1)\left(3\varepsilon_0 - \sum_j N_j\alpha_j\right) = 3\sum_j N_j\alpha_j,$$

$$3\varepsilon_0\varepsilon - \varepsilon\sum_j N_j\alpha_j - 3\varepsilon_0 + \sum_j N_j\alpha_j = 3\sum_j N_j\alpha_j,$$

$$3\varepsilon_0(\varepsilon - 1) - \varepsilon\sum_j N_j\alpha_j = 2\sum_j N_j\alpha_j,$$

$$3\varepsilon_0(\varepsilon - 1) = (\varepsilon + 2)\sum_j N_j\alpha_j,$$

Thus:

$$\boxed{\frac{\varepsilon - 1}{\varepsilon + 2} = \frac{\sum_j N_j\alpha_j}{3\varepsilon_0}}. \tag{4.7}$$

Equation 4.7 is the so-called Clausius-Mossoti relation, connecting a macroscopic physical quantity (dielectric constant ε) with a microscopical one (polarizability α). Thus, the dielectric constant is directly proportional to the polarizability/polarization of the system. With such motivation, dielectric constant measurements were carried out, in molecular systems of the TMTTF family in order to explore the ferroelectric behavior below the charge-ordering transition temperature.

Figure 4.5: Panoramic view of the Solid State Physics laboratory showing the Teslatron PT cryostat and all the equipments employed to perform the electrical measurements.

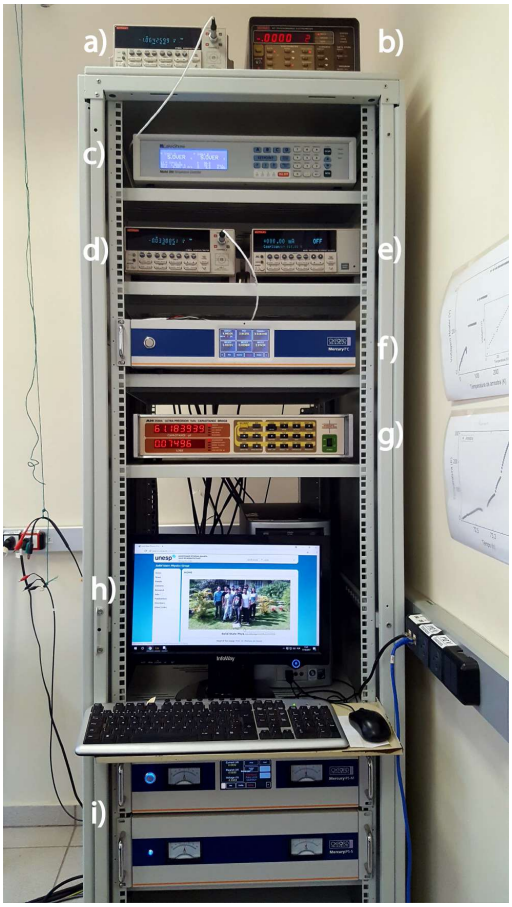

Figure 4.6: All the measuring equipments of the Solid State Physics Laboratory: a) Keithley 2182A nanovoltimeter; b) Keithley 617 programable electrometer (voltage, electrical resistance, charge and current); c) LakeShore 350 temperature controller; d) Keithley 2182A nanovoltmeter; e) Keithley 6220 precision current source (μA currents); f) Oxford MercuryiTC temperature controller; g) Andeen-Hagerling ultra-precision fixed 1 kHz capacitance bridge with resolution of 10^{-6} pF; h) Computer interfaced with all equipments for the data acquisition and i) MercuryiPS electrical current source for the superconducting magnet (up to 110 A).

4.5 The Solid State Physics laboratory in Rio Claro, SP – Brazil

The cryostat employed for the dimensionless dielectric constant and resistivity measurements was a Teslatron-PT ($1.4\,\mathrm{K} < T < 300\,\mathrm{K}$) supplied by Oxford Instruments with

^{4}He closed cycle, i.e., it operates with a fixed amount of Helium gas without the need to refill it for several periods of time.

There is a NiTi (Niobium Titanate) superconducting magnet with $T_c \approx 4.6\,\mathrm{K}$ that can apply magnetic fields up to 12 T, remaining in the so-called permanent mode [67]. Also, there is an outer vacuum chamber (OVC) of the cryostat that can reach pressures of 10^{-7} mbar, which is an excellent thermal isolation.

The ^{4}He is circulated through the system cooling the sample space through the exchange gas (also ^{4}He). Then, a compressor attached to the cryostat through $\approx 12\,\mathrm{m}$ of cryogenic lines (in order to maximize the efficiency of the thermal machine) cools back the helium (employing the expansion and compression method) and dissipates such potency ($\approx 12\,\mathrm{kVA}$) in another external water-based cooling system (Chiller). Such cycle keeps happening until the system is powered off. Yet, all the electrical signal of the laboratory is reconstructed by two no-breaks, guaranteeing that the oscillations of the power supply do not affect in any way the electrical measurements performed.

4.6 Experiments performed in the frame of this Master Thesis

A preliminary systematic investigation on the $\varepsilon'(T, B)$, $R(T, B)$ and $P(T, B)$ was performed in our research group in the frame of the Master Thesis of Paulo Menegasso [68].

All the experiments carried out in this Master Thesis in the molecular salts were performed in the c^*-axis (see Figure 4.3). Since the polarization at T_{co} occurs in the a-axis (electronic polarization), by measuring the c^*-axis the finite polarization observed indirectly by the dimensionless dielectric constant as a function of temperature was the ionic contribution for the total polarization.

It is worth mentioning that all experiments shown in this Master Thesis were performed in the Solid State Physics Laboratory in Rio Claro, SP - Brazil.

The samples were prepared using the 2-points method to accomplish all the bulk measurements described below. It starts in the choosing of the sample, aiming the ones that present the most parallel planes in the b^*-axis. Such planes are painted with a conductive paint (carbon paste in our case) to achieve an electrical configuration as close to a parallel plates capacitor. Later on, two gold wires of about $20\,\mu$m were attached in both opposite planes with carbon paste as well and then, the samples were fixed in the so-called mask (semiconducting to isolate the contact) to be attached in our system, allowing the electrical contact between them.

It is worth mention that for the $\varepsilon'(T,\, B)$ it is crucially relevant that the ratio between the sample thickness and its areas on the b^*-axis should be appropriate, otherwise the experimental results of ε' would not be possible to achieve. Also, this impacts directly in the capacitance of the prepared sample, since the capacitance depends on the area of the sample and the distance between the plates (thickness of the sample in this case), so it was able to be measured in the capacitance bridge of the laboratory. In the cases that the capacitance of the sample was too low or too noisy, a commercial capacitor was employed in series or in parallel (depending on the case) with the sample to reduce the so-called loss of the bridge and to achieve a clean measure for C x T, for example.

The parallel surfaces of the c^*-axis of the sample were revested with a thin layer of carbon paste in order to achieve a configuration similar to a parallel plates capacitor. Then, the capacitance C of the sample could be measured as a function of temperature T, aiming to obtain the dimensionless dielectric constant ε'. Such capacitance measurements were performed by employing an Andeen-Hagerling 2550A capacitance bridge with a resolution of 10^{-6} pF.

The dielectric constant ε could be determined by employing the well-known parallel plates capacitor mathematical expression, given by:

$$C = \frac{\varepsilon \cdot A}{d} \longrightarrow \varepsilon = \frac{C \cdot d}{A}, \tag{4.8}$$

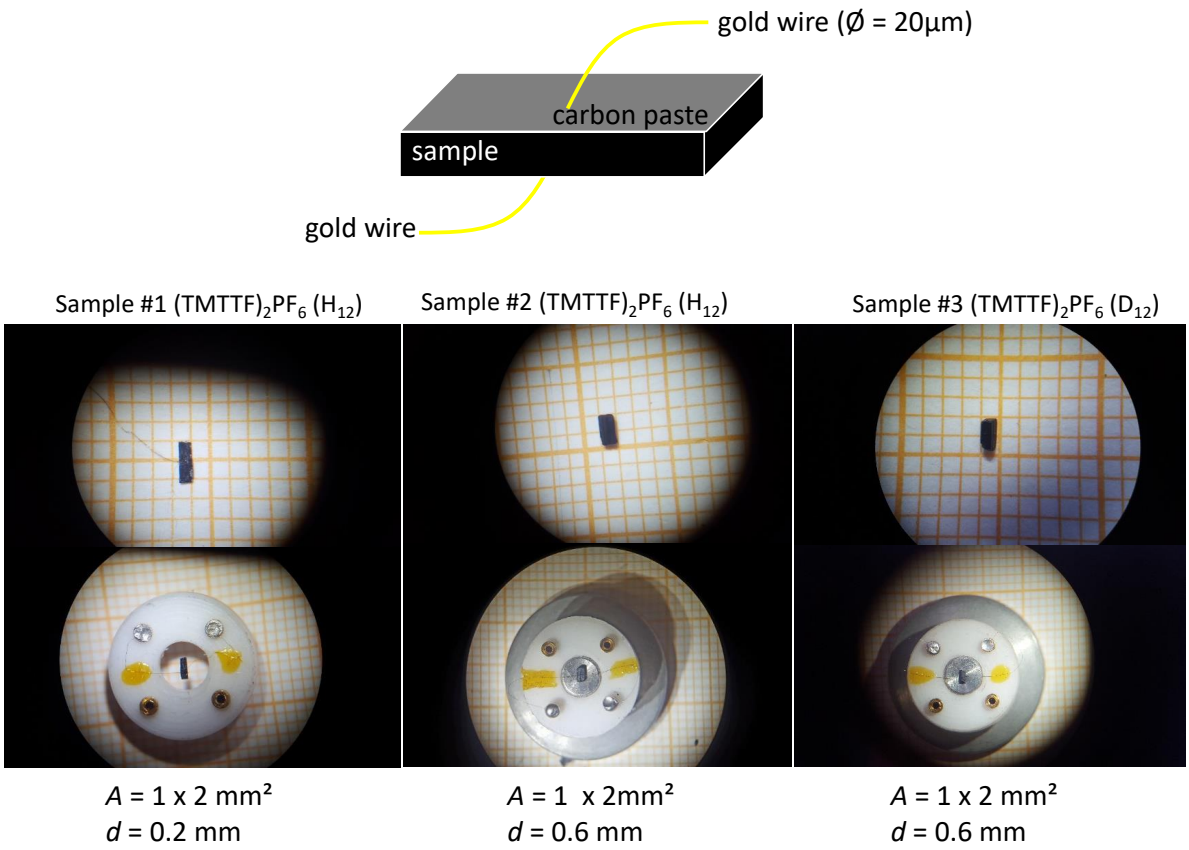

Figure 4.7: Electrical contacts employed in the c^*-axis with carbon paste (conductive) and golden wires attached in each parallel surface of the c^* axis of the samples, in order to achieve a nearly parallel capacitor plates configuration. The samples were chosen carefully in order to have the most parallels and homogeneous surfaces possible.

where C is the capacitance of the sample, A is the capacitor's plates area and d is the distance between them.

Thus, the dimentionless dielectric constant was determined by employing:

$$\varepsilon' = \frac{\varepsilon}{\varepsilon_0}, \tag{4.9}$$

where ε_0 is the electrostatic permittivity of the vacuum ($\varepsilon_0 = 8.854187817 \times 10^{-12}\,\mathrm{F/m}$) [69].

The Table 4.1 shows the samples in which experiments of resistivity and dielectric constant were carried out in this dissertation thesis.

System	Sample	Dimensions (height x length x width)	Batch
$(TMTTF)_2PF_6$ (H_{12})	#1	$1 \times 2 \times 0.2$ mm^3	EII 93 2
$(TMTTF)_2PF_6$ (H_{12})	#2	$1 \times 2 \times 0.6$ mm^3	EII 93 2
$(TMTTF)_2PF_6$ (D_{12})	#3	$1 \times 2 \times 0.6$ mm^3	IIE 107

Table 4.1: Samples employed in the experiments of this thesis with their proper dimensions. The batches were provided by the French collaborators Dr. Jean-Paul Pouget and Dr. Pascale Foury-Leylekian (*Laboratoire de Physique des Solides*, *Université Paris Sud*, CNRS UMR 8502, Orsay, France).

It is worth mentioning that the dielectric constant measurements in molecular salts already reported in literature [57] were not properly reproduced with such resolution as showed in this Master Thesis. Also, all the experiments carried out were performed employing a fixed frequency of 1 kHz. In what follows, electric resistivity $R(T)$ and

dielectric constant $\varepsilon'(T, B)$ were performed for both the fully hydrogenated and the 97.5% deuterated variant of the system $(TMTTF)_2PF_6$. The results are discussed below.

4.6.1 $(TMTTF)_2PF_6$ (H_{12})

The dielectric constant was measured employing the method described in the last section. The voltage applied by the capacitance bridge, in order to measure the capacitance of the sample, was obtained to achieve an electrical field ($E = U/d$) of 50 mV/cm. However, specifically with Sample #1, the dielectric constant was measured employing an electrical field of 150 mV/cm.

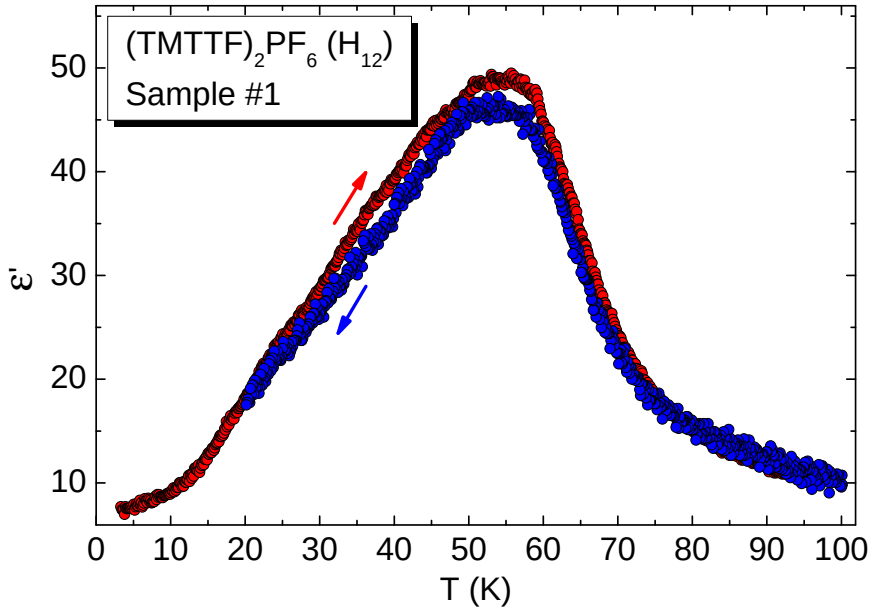

Figure 4.8: Dielectric constant *versus* temperature for the fully hydrogenated $(TMTTF)_2PF_6$ showing a broad maximum behavior at $T_{co} \sim 57$ K, indicating a finite polarization of the molecular salt below such temperature. A hysteretic behavior in the dielectric constant is observed upon heating and cooling. The data were measured employing a rate of ± 6 K/h and applied electric field of 150 mV/cm. The red and blue arrows indicate that the dielectric constant was measured upon heating and cooling, respectively.

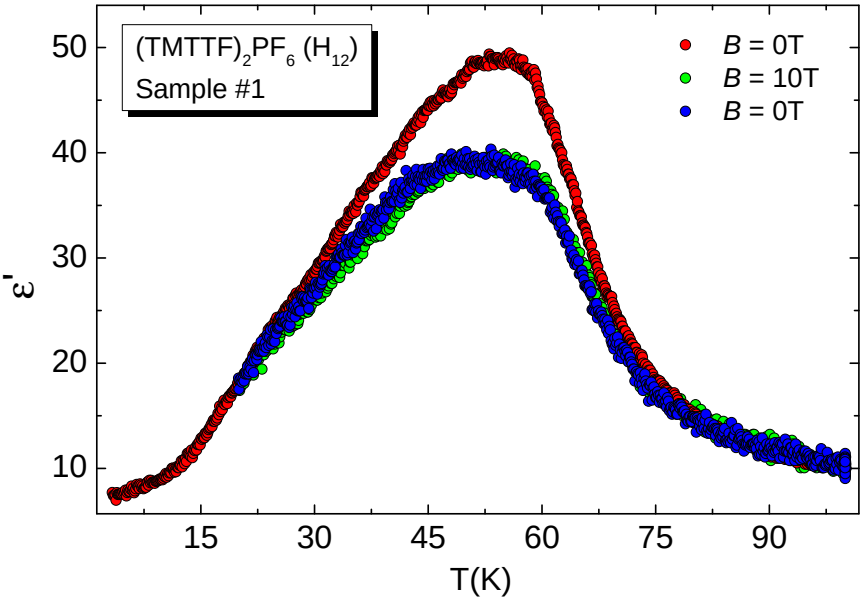

Figure 4.9: Dielectric constant *versus* temperature for the fully hydrogenated $(TMTTF)_2PF_6$. After 10 T of applied magnetic field, the dielectric constant was attenuated. However, upon removing the magnetic field the dielectric constant did not return to its original configuration. Such effect is associated with permanent disorder inserted by the magnetic field in the methyl groups. The data were measured employing a rate of $+6$ K/h and applied electric field of 150 mV/cm.

Such anomaly is associated with a finite polarization of the system below T_{co}, where

a charge disproportion occurs and a ferroelectric phase takes place. The maximum in the dielectric constant is associated with a finite polarization of the system at T_{co} and also to the maximum variation of the free-energy. A multiferroic behavior was not observed in this system. Instead, permanent disorder inflicted in the methyl groups due to the magnetic field permanently attenuated the dielectric constant.

The same investigation was carried out in another sample for the fully hydrogenated system of $(TMTTF)_2PF_6$. Resistivity measurements as a function of temperature were carried out employing the 2-points method since dielectric constant measurements were planned as well.

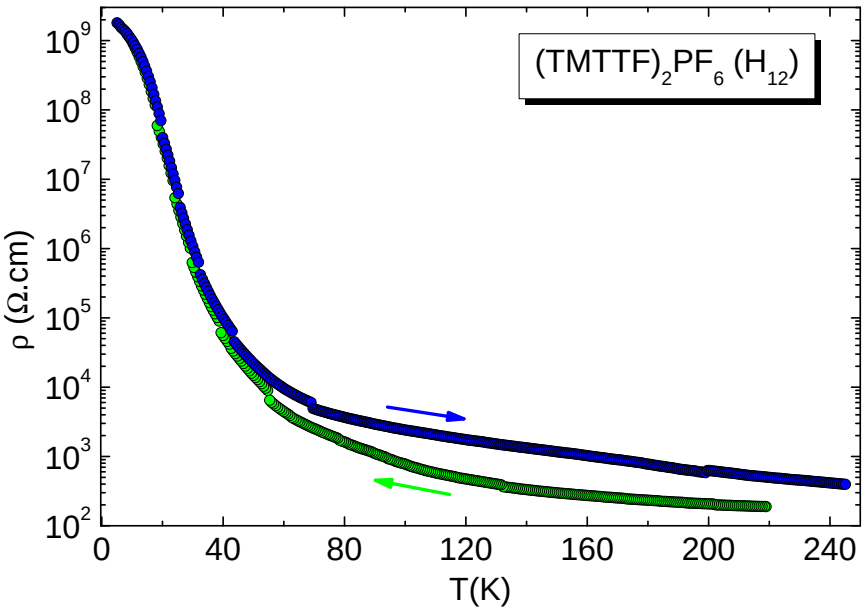

Figure 4.10: Electrical resistivity *versus* temperature for the fully hydrogenated $(TMTTF)_2PF_6$ showing and insulating behavior ($d\rho/dT < 0$) both upon heating and cooling with an employed rate of $\pm 10\,K/h$. A hysteretic behavior is observed upon cooling and heating. The resistivity measurements were carried out employing the two-points method.

Since the system is very metallic, there is an expressive difficulty in measuring the dielectric constant. In order to be able to measure the sample's capacitance, an auxiliary capacitor of $\sim 200\,pF$ was employed in parallel with the sample.

In order to investigate a possible multiferroic [70] character of the system, an external magnetic field of 10 T was applied aiming to investigate the effect of the magnetic field in the charge-ordered phase.

In this system, discontinuities in the dielectric constant were associated with ferroelectric clusters being thermally activated in different critical temperatures. Such clusters provide a broader dielectric response for the fully-hydrogenated salt. Also, the permanent disorder was inserted into the system by applying external magnetic field and a successive attenuation of the dielectric constant was observed, characterizing the fully hydrogenated $(TMTTF)_2PF_6$ as a relaxor ferroelectric, i.e., a ferroelectric system with disorder.

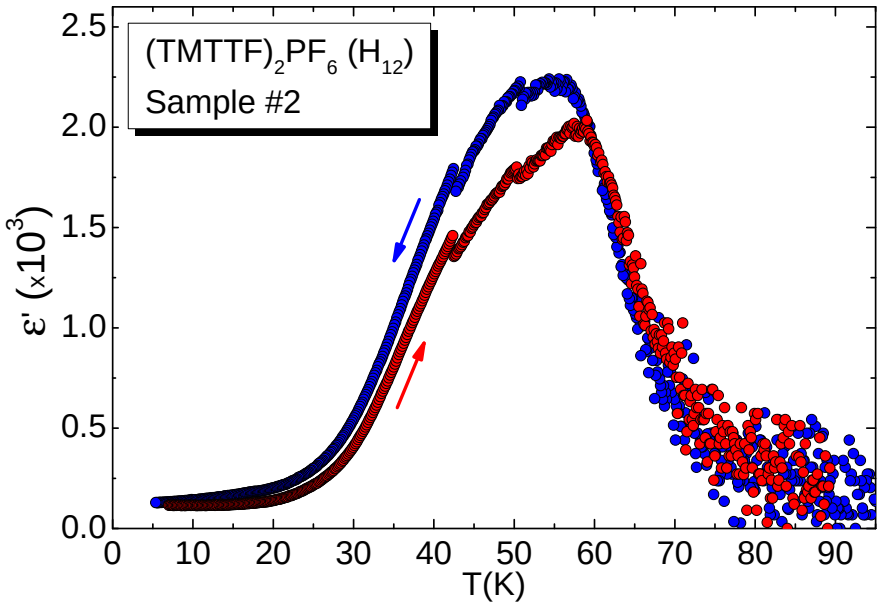

Figure 4.11: Dielectric constant *versus* temperature for the fully hydrogenated $(TMTTF)_2PF_6$ showing a broad anomaly at $T_{co} = \approx 57\,\mathrm{K}$. The difference between the heating and cooling is due to an hysteretic behavior in the dielectric constant. The discontinuities observed below T_{co} are due to thermally activated ferroelectric clusters. The noise above 65 K is due to the relatively low resistivity of the system. The data were measured employing a temperature rate of $\pm 7\,\mathrm{K/h}$ and an electric field of $50\,\mathrm{mV/cm}$.

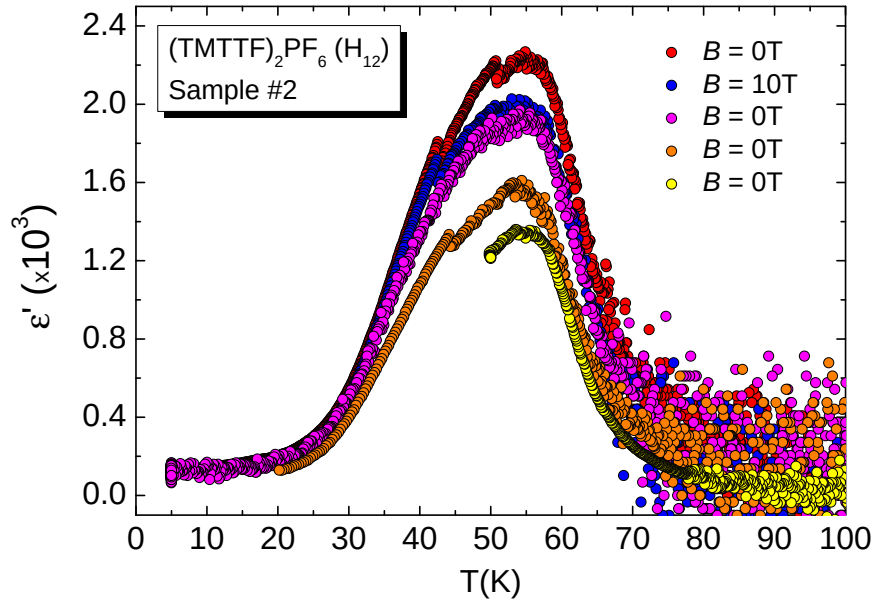

Figure 4.12: Dielectric constant *versus* temperature for the fully hydrogenated $(TMTTF)_2PF_6$ showing a broad maximum anomaly at $T_{co} \sim 57\,\mathrm{K}$. The red data set was measured employing a rate of $-7\,\mathrm{K/h}$, while it was employed a rate of $-10\,\mathrm{K/h}$ for the others datasets and an electric field of $50\,\mathrm{mV/cm}$ was applied. With an applied magnetic field of 10 T the dielectric constant was attenuated. By removing the magnetic field, the dielectric constant did no return to its original configuration and subsequent attenuations were observed in the successive thermal cycles. Such effect is due to permanent disorder inserted in the methyl groups by applying the magnetic field.

4.6.2 $(TMTTF)_2PF_6$ (D_{12})

In order to perform a systematic investigation, a 97.5 % deuterated sample was measured in order to compare with the fully hydrogenated one. This is the very first-time dielectric constant measurements for the 97.5 % deuterated variant of $(TMTTF)_2PF_6$ were carried out.

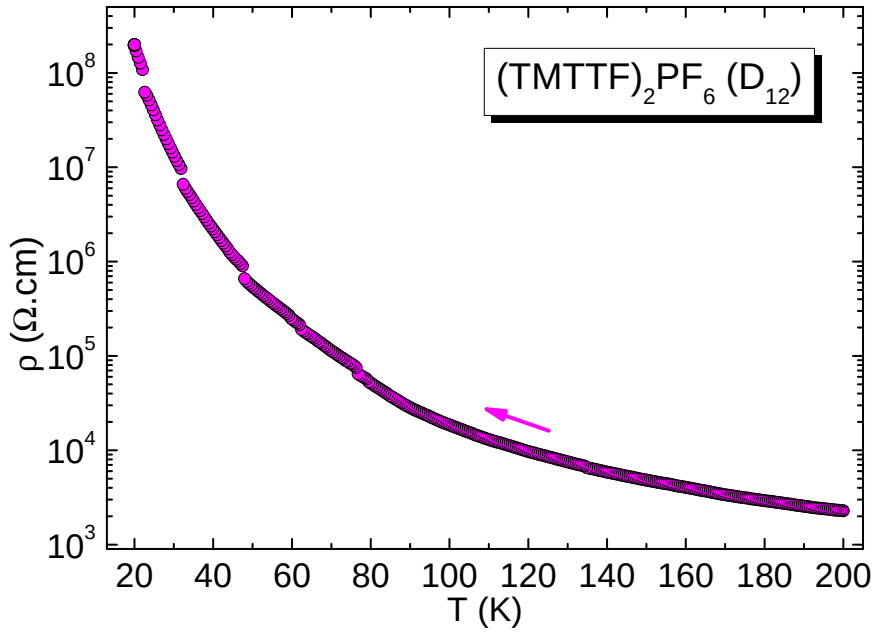

Figure 4.13: Electric resistivity *versus* temperature for the 97.5 % deuterated variant of $(TMTTF)_2PF_6$, showing an insulating behavior. The data were measured employing a rate of +9 K/h.

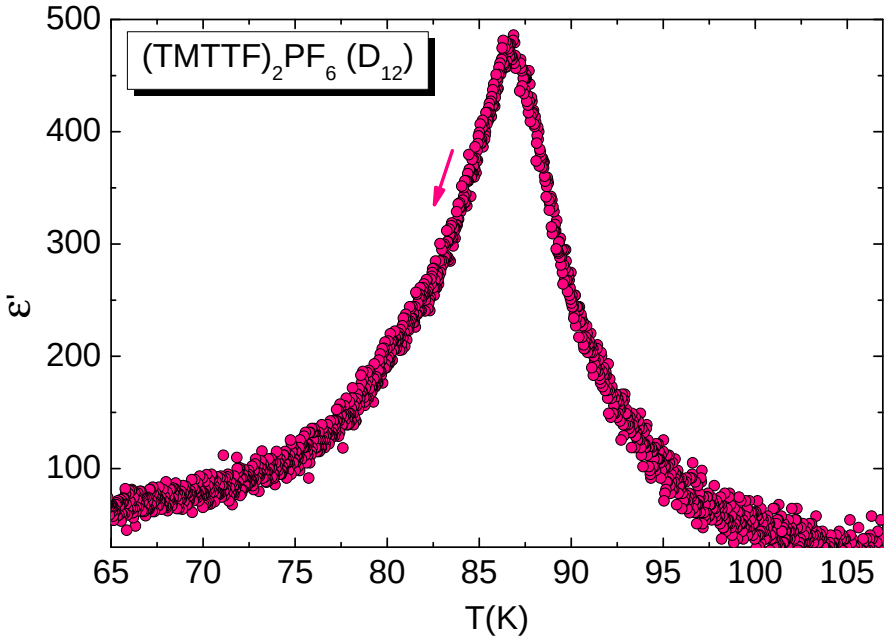

Figure 4.14: Dielectric constant *versus* temperature for the 97.5 % deuterated variant of $(TMTTF)_2PF_6$ showing a peak-like anomaly at $T_{co} \sim 87$ K. The anomaly differs from the fully hydrogenated salt (bump-like). The data were measured employing a rate of −12 K/h with 50 mV/cm of applied electric field.

A hysteretic behavior was also observed upon heating and cooling. In order to also explore the possible multiferroic character of this system, a magnetic field of 4 T was applied. This is also due to the inserted disorder in the methyl groups by the magnetic

field. A capacitor of $\sim 120\,pF$ in parallel with the sample was employed in order to measure the capacitance of this sample due to its relatively low electrical resistance.

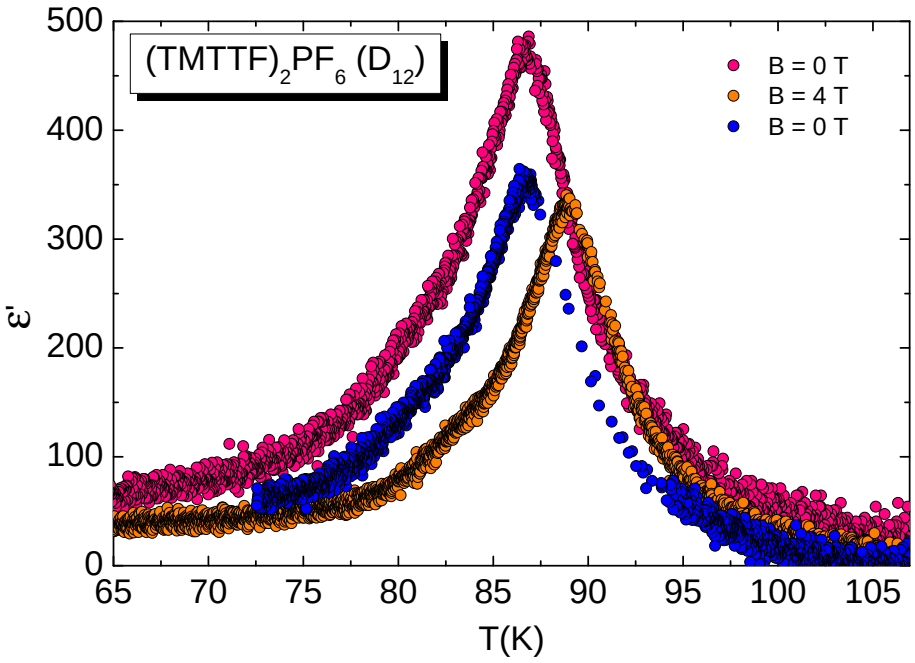

Figure 4.15: Dielectric constant *versus* temperature for the 97.5 % deuterated variant of $(TMTTF)_2PF_6$ showing a peak-like anomaly at $T_{co} \sim 87\,K$. A hysteretic behavior was observed upon heating (pink data set) and cooling (orange). The dielectric constant measured upon heating (blue) was permanently attenuated by the magnetic field, due to inserted disorder in the methyl groups. The data were measured with a rate of $\pm 12\,K/h$ and $50\,mV/cm$ of applied electric field.

A permanent attenuation of the dielectric constant was also observed due to the applied magnetic field. The 97.5 % deuterated variant $(TMTTF)_2PF_6$ show a peak-like anomaly at T_{co} instead of a broad-like one for the fully hydrogenated one.

4.6.3 The mean-field theory

Regarding the permanently inserted defects in the methyl groups, an analysis in the so-called mean-field theory can be performed. In this regard, it is possible to plot the dielectric constant in the so-called Curie-Weiss behavior. The Curie-Weiss behavior is given by the expression:

$$\frac{1}{\varepsilon'} = A_{\pm} \cdot |T - T_{co}|, \tag{4.10}$$

where $A_{\pm}$ are the expected slopes for such behavior and the relation between them is given by:

$$\frac{A_-}{A_+} = 2. \tag{4.11}$$

From Equation 4.11 it is clear a factor 2 between the slopes of the solid lines ($\theta = 2\theta$). In this context, the Curie-Weiss behavior was analyzed for the fully hydrogenated and the 97.5% deuterated $(TMTTF)_2PF_6$, in order to compare the measured dielectric constants in the scope of the mean-field theory. The solid lines in Figure 4.16 represent the expected behavior of the data accordingly to the mean-field theory. The more the data diverges from the mean-field behavior ($\theta \neq 2\theta$), the greater the number of intrinsic defects in the system. In this context, the fully hydrogenated salt diverges expressively from the mean-field behavior indicating the presence of intrinsic defects in the system. As shown in Figure 4.12, the dielectric constant was permanently attenuated due to external magnetic field and a successive attenuation of it was observed. Such results indicate

that not only the fully hydrogenated salt present intrinsic defects in its structure (relaxor ferroelectric [71]), but such defects can be inserted by the application of external magnetic field and/or thermal cycling.

Following discussion with Prof. Roberto E. Lagos Monaco during the qualify exam, it is worth mentioning that the mean-field approach does not work for low-dimension systems. Hence, the deviation from the mean-field theory observed in the present investigations for the TMTTF salts (Figure 4.16) could not only be associated with defects/disorder, but also with the low-dimension character of such systems.

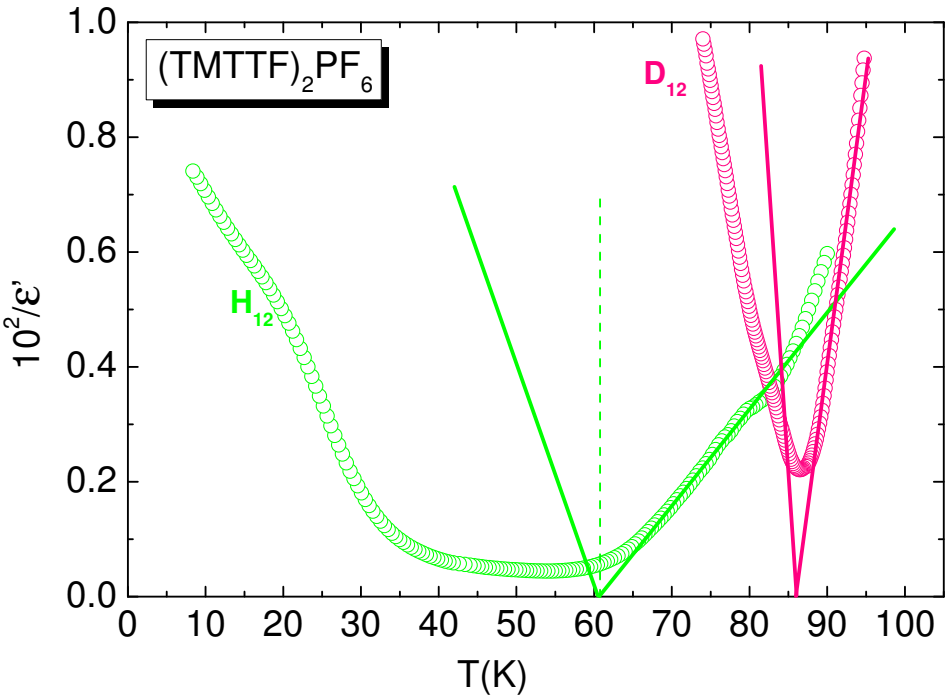

Figure 4.16: Curie-Weiss plots for the fully hydrogenated and 97.5% deuterated $(TMTTF)_2PF_6$. The solid lines represent the expected behavior for the data by the mean-field theory and the dotted line represents the smoothed data for both salts to show the factor two between the left and right slopes. For an aesthetic question, the dashed line was suppressed for the 97.5% deuterated salt data. It is clear that the fully hydrogenated salt diverges expressively from the theory, indicating the presence of intrinsic defects in this system, being considered as a relaxor ferroelectric, i.e. a ferroelectric with disorder [71].

Recently, it was shown that there is a predominance of valence electrons almost exclusively in the methyl groups of the TMTTF molecule [72], as shown in Figure 4.17.

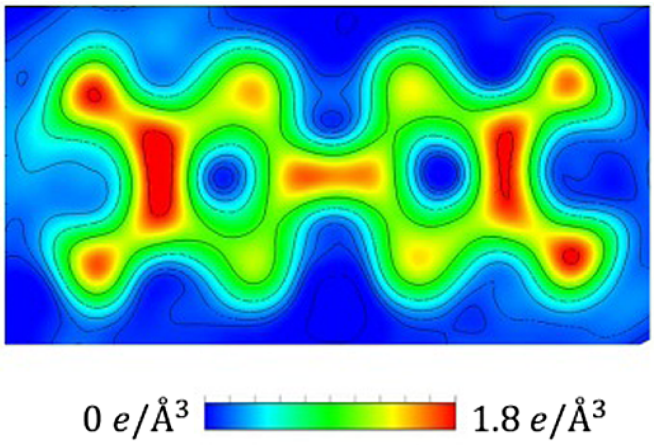

Figure 4.17: Valence electrons distribution in the TMTTF molecule, the red regions denote more valence electrons. Note there is a significant higher distribution of the valence electrons in the methyl groups [72].

Since the counter-anions are located in the cavity formed by the methyl groups and there is a significant density of valence electrons in it, by applying external magnetic field it is possible to change the methyl's groups degrees of freedom and thus the position of the counter-anion. Therefore, the result shown in Figure 4.17 are totally in line with the experimental results shown in Figure 4.12, since disorder is inserted by application of external magnetic field in the methyl groups and it can be observed by the fact that the dielectric constant was attenuated by the magnetic field and subsequent thermal cycling.

It is worth mentioning that Prof. Dr. Ricardo Paupitz (UNESP, Rio Claro, SP − Brazil) also performed DFT calculations in the hydrogenated variant of $(TMTTF)_2PF_6$ and obtained a similar result from Figure 4.17 by observing a more expressive concentration of magnetic moments in the methyl groups of the TMTTF molecule.

During the final period of my master degree, I had the opportunity to perform *ab initio* DFT calculations, with support from Prof. Dr. Ricardo Paupitz and my advisor Prof. Dr. Mariano de Souza, in the hydrogenated variant by optimizing both the molecular structure of the system and the unit cell, in order to find the configuration of minimal energy at $T = 0\,\mathrm{K}$. Some perspectives lies on performing systematic DFT calculations in order to investigate the electronic density in the TMTTF molecule and the effects of rotating the methyl groups with the total energy of the system, in order to corroborate the experimental results shown in this Master Thesis, since magnetic field can change the degrees of freedom of such groups and insert disorder into the system.

Chapter 5

Summary and Conclusions

In order to make a more clear and comprehensive summary and conclusions, the three main chapters of this Master Thesis were divided to provide a better understanding of the fundamental aspects here discussed. Thus, it follows:

The magnetocaloric effect (the magnetic Grüneisen parameter): the classical magnetic model Brillouin and the 1D−Ising were solved in details following discussions presented in classical textbooks. Next, a discussion regarding the Grüneisen parameter was performed to demonstrate its importance as being the only mathematical tool to determine experimentally a quantum critical point (divergence of the Grüneisen parameter indicates a QPT). In this regard, the Grüneisen parameter was calculated for the Brillouin model considering both $J = 1/2$ and arbitrary J. The Grüneisen parameter for such model diverges at $T = 0\,\mathrm{K}$ and $B = 0\,\mathrm{T}$. This indicates that even that the Brillouin model is purely classic (it does not incorporate quantum mechanics) it does show a quantum critical behavior intrinsically at $T = 0\,\mathrm{K}$. Such results are part of a published manuscript in the journal Physical Review B (see file in the end of this Master Thesis)

The binary alloy $FeSe_{1-x}$: a detailed discussion of the evolution of superconductivity over the years was performed followed by the characterization of the physical properties of the binary alloy $FeSe_{1-x}$. The synthesis method was described and several samples were obtained (aiming the hexagonal phase). X-ray measurements were performed in the synthesized samples and concluded that we did not have a homogeneous phase of the hexagonal one. Further systematic investigations will be carried out to synthesize such phase and completely characterize it (as well as the tetragonal one already is) in order to connect such properties with the theoretical model of the $3d$ orbitals of Fe, proposed by L. Craco and Leoni.

Correlation phenomena in the $(TMTTF)_2X$ ($X = PF_6$-H_{12}, PF_6-D_{12}) Fabre-salts: a proper description of all the relevant fundamental literature was performed aiming to focus on the Mott-insulator, charge-ordering and ferroelectric phases, in order to connect directly such theoretical aspects with the experiments carried out in this Master Thesis. The systems investigated were the hydrogenated $(TMTTF)_2PF_6$ and the 97.5% deuterated variant of $(TMTTF)_2PF_6$. Regarding the hydrogenated variant, measurements of electrical resistivity and dielectric constant were performed. The dielectric behavior was found to have a maximum at T_{co} indicating a finite polarization of the system at this temperature. Several "jumps" were observed in the dielectric constant of one sample of this system. Such behavior is directly connected with the presence of ferroelectric clusters

being thermally activated upon varying the temperature, explaining the broad dielectric response in this system. Regarding the 97.5% deuterated variant, it was observed a peak-like anomaly in the dielectric constant measurements and such results are not yet published in literature. Both systems were measured under external magnetic field and an attenuation of the dielectric constant was observed, such result is connected with both magnetoelectricity and insertion of defects into the systems due to thermal cycling or magnetic field. Yet, the deviation between the Curie-Weiss plots and the mean-field theory provided crucial physical information regarding intrinsic defects present in the hydrogenated system. Part of the experimental results in this Master Thesis contributed to a manuscript published in Physical Review B (see file in the end of this Master Thesis).

Chapter 6

Perspectives and Outlook

Further systematic investigations regarding this Master Thesis includes new synthesis methods (as well as a more systematic investigation of the electrochemical growth method) aiming not only to learn how the methods work, but to synthesize samples of systems of interest in order to continue such studies, specially regarding the $FeSe_{1-x}$ hexagonal phase and the theoretical proposal to understand the difference between the two phases of interest.

Also, our group can perform thermal expansion measurements via dilatometric cell with ultra-high resolution ($\Delta l \sim 0.05{-}0.1$ Å), which I got acquainted during my Master's degree. Thermal expansion measurements of the investigated molecular conductors in this Master Thesis, as a function of temperature and magnetic field (magnetostriction as well), are to be performed in a near future aiming to connect such results with the dielectric ones reported here. Such investigation will provide crucial information regarding the influence of the magnetic field on the ferroelectric Mott-Hubbard phase and will contribute to its fundamental understanding.

References

[1] Stephen Blundell, Magnetism in Condensed Matter Physics, Oxford University Press (2001).

[2] Wolfgang Nolting and Anupuru Ramakanth, Quantum Theory of Magnetism, Springer (2009).

[3] F. Reif, Fundamentals of Statistical and Thermal Physics, Secondth Edition, Waveland Press (2009).

[4] N. W. Ashcroft and N. David Mermin, Solid State Physics, Saunders College Publishing (1976).

[5] Robert Andrews Millikan, Physical Review (Series I) **32**, 349 (1911).

[6] A. W. Kinross, M. Fu, T. J. Munsie, H. A. Dabkowska, G. M. Luke, Subir Sachdev, and T. Imai, Phys. Rev. X **4**, 031008 (2014).

[7] R. K. Pathria, Statistical Mechanics − Second Edition, Butterworth-Heinemann (1996).

[8] Charles Kittel, Introduction to Solid State Physics - Eighth Edition, John Wiley & Sons (2005).

[9] S. Sachdev, Quantum Phase Transitions, Cambridge University Press (2001).

[10] Lorenz Bartosch, Mariano de Souza, and Michael Lang, Physical Review Letters **104**, 245701 (2010).

[11] M. de Souza, A. Brühl, Ch. Strack, B. Wolf, D. Schweitzer, and M. Lang, Physical Review Letters **99**, 037003 (2007).

[12] M. de Souza and L. Bartosch, Journal of Physics: Condensed Matter **27**, 053203 (2015).

[13] Lijun Zhu, Markus Garst, Achim Rosch and Qimiao Si, Physical Review Letters **91**, 066404 (2003).

[14] Kerson Huang, Statistical Mechanics, John Wiley & Sons (1963).

[15] R. Küchler *et al.*, Physical Review Letters **91**, 066405 (2003).

[16] Markus Garst and Achim Rosch, Physical Review B **72**, 205129 (2005).

[17] T. H. K. Barron and G. K. White, Heat Capacity and Thermal Expansion at Low Temperatures, Springer (1999).

[18] A. Steppke *et al.*, Science **339**, 933 (2013).

[19] H. K. Onnes, Commun. Phys. Lab. Univ. Leiden **12**, (1911).

[20] W. Meissner and R. Ochsenfeld, *Naturwissenschaften* **21**, 787 (1933).

[21] J. Bardeen, L. N. Cooper, and J. R. Schriefer, Physical Review **108**, 1175 (1957).

[22] J. Bednorz and K. Müller, *Zeitschrift für Physik B* **64**, 189 (1986).

[23] Y. Kamihara *et al.*, Journal of the American Chemical Society **128**, 31 (2006).

[24] J. E. Hirsch, M. B. Maple, F. Marsiglio, Physica C: Superconductivity and Its Applications **514**, 1 (2015).

[25] F. Steglich *et al.*, Physical Review Letters **43**, 1892 (1979).

[26] D. Jérome, A. Mazaud, M. Ribault, K. Bechgaard, Journal Physique Letters **41**, L95 (1980).

[27] V. L. Ginzburg, Contemporary Physics **33**, 15 (1992).

[28] N. W. Ashcroft, Physical Review Letters **21**, 1748 (1968).

[29] N. W. Ashcroft, Physical Review Letters **92**, 187002 (2004).

[30] Y. Wang and Y. Ma, The Journal of Chemical Physics **140**, 040901 (2014).

[31] A. P. Drozdov *et al.*, Nature **525**, 73 (2015).

[32] A. Y. Kasumov *et al.*, Science **291**, 280 (2001).

[33] Y. Okahata, T. Kobayashi, H. Nakayama and K. Tanaka, Supramolecular Science **5**, 317 (1998).

[34] H. W. Fink and C. Schöenenberger, Nature **398**, 407 (1999).

[35] E. Braun, Y. Eichen, U. Sivan and G. Ben-Yoseph, Nature **391**, 775 (1998).

[36] D. Porath, A. Bezryadin, S. de Vries and C. Dekker, Nature **403**, 635 (2000).

[37] F. Steglich *et al.*, Physical Review Letters **43**, 1892 (1979).

[38] J. G. Bednorz and K. A. Müller, *Zeitschrift für Physik* B **64**, 189 (1986).

[39] N. F. Mott, Review of Modern Physics **40**, 677 (1968).

[40] K. Kanoda, Hyperfine Interactions **104**, 235 (1997).

[41] C. Varma, Nature **468**, 184 (2010).

[42] D. C. Johnston, Advance in Physics **59**, 803 (2010); K. Ishida, Y. Nakai, and H. Hosono, Journal of the Physical Society of Japan **78**, 062001 (2009).

[43] C. Wang *et al.*, Superconductivity Science and Technology **23**, 055002 (2010).

[44] M. Burrard-Lucas *et al.*, Nature Materials **12**, 15 (2012).

[45] S. Medvedev *et al.*, Nature Materials **8**, 576 (2009).

[46] Jian-Feng Ge *et al.*, Nature Materials **14**, 285 (2015).

[47] B. Massalski, H. Okamoto *et al.*, Binary Alloy Phase Diagrams – Second Edition, ASM International (1990).

[48] Mariano de Souza, Amir-Abbas Haghighirad, Urich Tutsch, Wolf Assmus, and Michael Lang, European Physical Journal B **77**, 101 (2010).

[49] L. Craco and S. Leoni, Europhysics Letters **92**, 67003 (2010).

[50] N. F. Mott, Metal-Insulator Transitions – Second Edition, Taylor and Francis (1990).

[51] S. S. P. Parkin, M. Ribaut, D. Jérome and K. Bechgaard, Journal of Physics C: Solid State Physics **14**, 5305 (1981).

[52] W. A. Little, Physical Review A **134**, 1416 (1964).

[53] M. de Souza and J.-P. Pouget, Journal of Physics: Condensed Matter **25**, 343201 (2013).

[54] M. Dressel, *Naturwissenschaften* **94**, 527 (2007).

[55] D. Jérome, A. Mazaud, M. Ribault and K. Bechgaard, Journal of Physical Letters **41**, L95 (1980).

[56] H. Seo and H. Fukuyama, Journal of the Physical Society of Japan **66**, 1249 (1997).

[57] F. Nad and P. Monceau, Journal of the Physical Society of Japan **75**, 051005 (2006).

[58] M. Dressel, M. Dumm, T. Knoblauch, and M. Masino, Crystals **2**, 528 (2012).

[59] M. de Souza, P. Foury-Leylekian, A. Moradpour, J.-P. Pouget, and M. Lang, Physical Review Letters **101**, 216403 (2008).

[60] B. Köhler, E. Rose, M. Dumm, G. Untereiner, and M. Dressel, Physical Review B **84**, 035124 (2011).

[61] de Souza M 2008 *PhD Thesis* University of Frankfurt (`http://publikationen.ub.uni-frankfurt.de/volltexte/2009/6240/`).

[62] M. Imada, A. Fujimori, and Y.Tokura, Review of Modern Physics **70**, 1039 (1998).

[63] M. Mostovoy, Physical Review Letters **96**, 067601 (2006).

[64] H. Katsura, N. Nagaosa, and A. V. Balatsky, Physical Review Letters **95**, 057205 (2005).

[65] J. Kondo and K. Yamaji, Journal of the Physical Society of Japan **43**, 424 (1977).

[66] J.-P. Pouget, Physica B **407**, 1762 (2012).

[67] Stephen Blundell, Superconductivity: A Very Short Introduction, Oxford University Press (2009).

[68] Paulo Eduardo Menegasso Filho and Mariano de Souza (Advisor), Investigation of the transport properties of ferroelectric Mott-Hubbard phase in molecular conductors (2016).

[69] Peter J. Mohr, Barry N. Taylor, and David B. Newell, Review of Modern Physics **80**, 633 (2008).

[70] Gianluca Giovanetti, Reza Nourafkan, Gabriel Kotliar, and Massimo Capone, Physical Review B **91**, 125130 (2015).

[71] G. A. Samara, Journal of Physics: Condensed Matter **15**, R367 (2003).

[72] Shunsuke Kitou *et al.*, Physical Review Letters **119**, 065701 (2017).

Appendix 1: ICAM-I2CAM Junior Exchange Program - National High Magnetic Field Laboratory

As a part of this Master Thesis, with high support from my advisor Prof. Dr. Mariano de Souza, I was granted an exchange program for 3 weeks in the National High Magnetic Field Laboratory (NHMFL), Tallahassee, FL − U.S.A., being fully financed (up to US$4,000) by the ICAM (Institute for Complex Adaptive Matter). The main focus was to study fundamental aspects of the synthesis of molecular conductors via the electrochemical method. The final report is included in the following.

Final Report – Junior Short Award Application

Synthesis and Exploration of the Physical Properties of Molecular Conductors

Applicant: Lucas Cesar Gomes Squillante (M.Sc. in progress)
Advisor: Dr. Valdeci Pereira Mariano de Souza
Host scientist in the USA: Dr. John Schlueter
Co-host scientist in the USA: Dr. Theo Siegrist

1 Introduction

Molecular conductors have been intensively investigated in the last decades, since they are proper playgrounds to study correlation phenomena [1–3]. Nowadays, it is known that such correlation effects in molecular systems can lead to exotic phenomena of matter, such as Mott-insulator [2], superconductivity [3–5] and charge-ordering [1], just to mention a few examples. The systems are very crystalline, which enables possibilities of investigating electron-electron interactions in a *clean* environment.

In this regard, the molecular systems $(TMTTF)_2X$ (TMTTF is tetramethyltetrathiafulvalene, X denotes a monovalent counter-anion) and κ-$(BEDT\text{-}TTF)_2Z$ (BEDT-TTF is bis(ethylenedithio)-tetrathiafulvalene and Z refers to the counter-anion) were of particular interest in this exchange program.

2 Electrochemical growth

One way of synthesizing molecular compounds of interest is the well-known electrochemical growth [6, 7]. Such crystal-growth method (Fig. 1), enables the synthesis of very high-crystalline molecular compounds. The main goal of this exchange program was to study both theoretical and experimental aspects of the electrochemical synthesis.

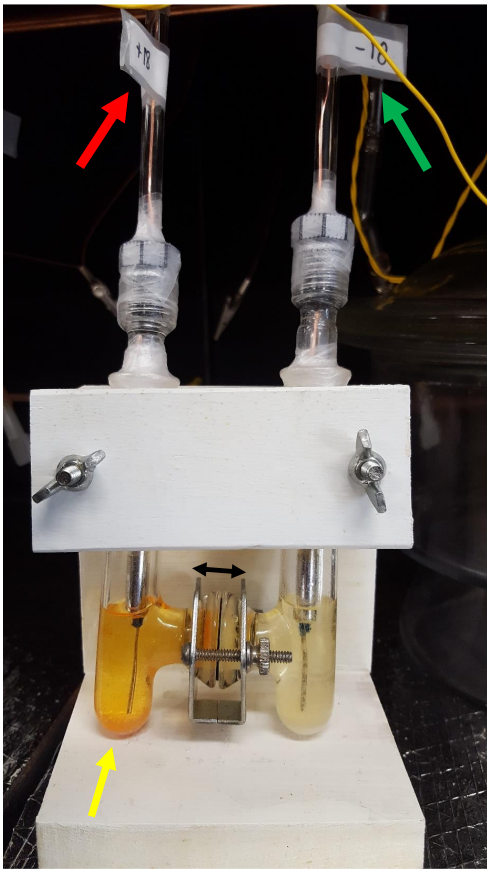

Figure 1: Electrochemical cell with an on-progress growth of the system κ-$(BEDT\text{-}TTF)_2Cu[N(CN)_2]I$. It is observed a cathode (+ red arrow) and an anode (− green arrow) and the crystals should begin to grow in the cathode (yellow arrow) in an estimate time of about 2−4 weeks. A current density of $0.5\,\mu A$ was applied following the already reported data from the literature [8]. The black arrows in the junction represent a very small flux between the solutions of $(BEDT\text{-}TTF)_2$ (left) and $PPh_4N(CN)_2$ + CuI (right), both sides are dissolved in 1,1,2−Trichloroethane (TCE).

During the period (05/01/2017 to 05/21/2017) of my stay in the National High Magnetic Field Laboratory (NHMFL), two electrochemical synthesis were initiated aiming to achieve the correct phase of the molecular compound κ-(BEDT-TTF)$_2$Cu[N(CN)$_2$]I. The motivation in growing this system is to continue previous investigations with focus on the exploration of the P *versus* T phase diagram [9], where it is proposed magnetism driven by electron-dipole [10]. Our plan is to perform dielectric constant and high-resolution thermal expansion measurements as a function of the temperature T and the magnetic field B in our lab in Brazil to probe possible ferroelectricity/multiferroicity upon entering the long-range AF ordering. Also, we could compare such results with those already published for the κ-(BEDT-TTF)$_2$Cu[N(CN)$_2$]Cl [10].

Regarding the TMTTF salt also included in the one-page proposal, the system of interest was the (TMTTF)$_2$Br also to explore its ferroelectric/multiferroic character. Due to the extremely high prices on acquiring the TMTTF compound for the crystal growth, the synthesis of such system could not be performed.

3 Correlated phenomena in molecular metals

Following previous investigations in the last decade, see e.g. Refs. [1, 2], we are interested in the investigation of a few physical questions overlooked so far. More specifically, in regard to the physical properties of molecular conductors (see Fig. 2), some of the topics proposed by my advisor (Dr. Mariano de Souza) to Dr. John Schlueter are as follows:

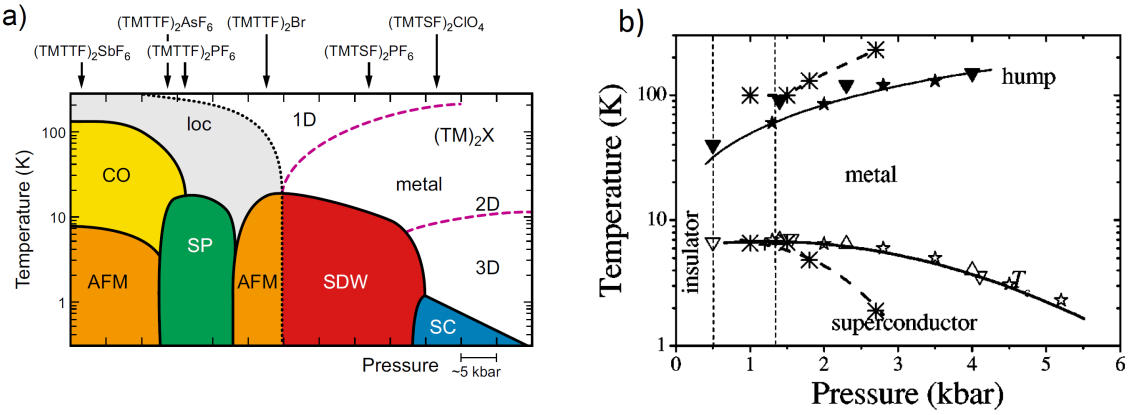

Figure 2: **a)** P *versus* T phase diagram [11] for the TMTTF and TMTSF salts. The phases shown are localization (loc), charge-ordering (CO), spin-Peierls (SP), antiferromagnet (AFM), spin-density-wave (SDW) and superconductor (SC). The straight lines represent actual phase transitions while the dashed ones are characterized as crossovers. The black arrows represents the ambient-pressure position of each salts (chemical pressure in the counter-anions). **b)** P *versus* T phase diagram [9] of κ-(BEDT-TTF)$_2$Cu[N(CN)$_2$]I obtained from resistance measurements. The crossed with dashed lines represent the so-called old samples, while the solid lines represent the new ones. The different symbols also represent different samples.

- Synthesis of the κ-(BEDT-TTF)$_2$Cu[N(CN)$_2$]I salt in order to continue previous investigations with focus on the exploration of the P versus T phase diagram [9]. Here we plan to perform systematic dielectric constant, thermal expansion and standard characterization measurements (varying T and B) to probe possible ferroelectricity/multiferroicity upon entering the long-range AF ordering domain. Also, a comparison with results already published for the κ-(BEDT-TTF)$_2$Cu[N(CN)$_2$]Cl [10] is planned;

- Synthesis of TMTTF-based salts focusing in the $(TMTTF)_2Br$, since a charge-ordering phase is predicted at $T \approx 34\,K$ [12];
- $(TMTTF)_2X$, where $X = PF_6$, SbF_6, AsF_6 partially deuterated to explore the isotope effect in the physical properties of these salts, focusing on the charge-ordering phase;
- TTF-TCNQ, TTF-Cl and TTF-Br: here also we are interested in exploring possible ferroelectric/multiferroic character of theses salts;
- $(BEDT\text{-}TTF)_2F(C_4H_6)CH_2SO_3$: to finish the project my advisor and Dr. J. Schlueter started a couple of years ago in cooperation with Prof. Dr. Ricardo Urbano and M. Sc. Paulo Menegasso;
- α/β-$(BEDT\text{-}TTF)_2IBr_2$: systematic thermal expansion measurements (Dr. John Schlueter suggested during his stay in Brazil some years ago);
- Variants of picene in order to look for higher-T_c.

4 Scientific cooperation in the frame of this exchange project

After this exchange program we were able to initiate a cooperation between the MagLab and the São Paulo State University (UNESP). Dr. John Schlueter and Dr. Theo Siegrist provided us samples grown at the MagLab of the κ-$(ET)_2Hg(SCN)_2Br$ system. Also here we are interested in performing dielectric constant and high-resolution thermal expansion both as a function of the temperature T and the magnetic field B in our lab in Brazil, since a metal-insulator transition is driven at $\sim 140\,K$ [13]. Furthermore, Alyssa Henderson, a Ph.D. student in Dr. Theo's group, is currently applying for the American Physical Society (APS) short exchange program between USA and Brazil to visit our group. The proposal includes crystal-growth at the MagLab of compounds of interest, concomitant with their physical properties characterization in our lab here in Brazil.

The well-established cooperation between Mariano de Souza and John Schlueter [10, 14–19], was reinforced after this exchange program, since an additional collaboration channel was opened with the group of Dr. Theo Siegrist.

5 Acknowledgements

I would like to acknowledge my advisor Dr. Mariano de Souza, without which this project would not be possible, the Institute for Complex Adaptive Matter (ICAM) and The Gordon and Betty Moore Foundations for the financial support, Dr. John Schlueter and Dr. Theo Siegrist for supporting this project and hosting me at the MagLab, Arshad Javed for all the bureaucratic support, M.Sc. Alyssa Henderson and Dr. Tiglet Besara for all the support at the MagLab, x-ray measurements and crystal-growth experiments.

References

[1] M. de Souza, J.-P. Pouget, Journal of Physics: Condensed Matter **25**, 343201 (2013).

[2] M. de Souza and L. Bartosch, Journal of Physics: Condensed Matter **27**, 053203 (2015).

[3] S. S. P. Parkin, M. Ribaut, D. Jérome and K. Bechgaard, Journal of Physics C: Solid State Physics **14**, 5305 (1981).

[4] W. A. Little, Physical Review A **134**, 1416 (1964).

[5] D. Jerome, A. Mazaud, M. Ribault and K. Bechgaard, Journal of Physics Letters **41**, L95 (1980).

[6] S. Curreli, P. Deplano, M. L. Mercuri, L. Pilia, A. Serpe, John A. Schlueter, Michael A. Whited, Urs Geiser, E. Coronado, C. J. Goémez-García, and E. Canadell, Inorganic Chemistry **43**, 2049 (2004).

[7] S. K. Pal, M. E. Itkis, R. W. Reed, R. T. Oakley, A. W. Cordes, F. S. Tham, T. Siegrist, and R. C. Haddon, Journal of the American Chemical Society **126**, 1478 (2004).

[8] N. D. Kushch, M. A. Tanatar, E. B. Yagubskii, and T. Ishiguro, Journal of Applied and Theoretical Physics Letters **73**, 429 (2001).

[9] M. A. Tanatar *et al.*, Physical Review B **65**, 064516 (2002).

[10] P. Lunkenheimer, J. Müller, S. Krohns, F. Schrettle, A. Loidl, Be. Hartmann, R. Rommel, M. de Souza, C. Hotta, J. A. Schlueter and M. Lang, Nature Materials **11**, 755 (2012).

[11] M. Dressel, Naturwissenschaften **94**, 527 (2007).

[12] F. Nad, P. Monceau and J. M. Fabre, European Physical Journal B **3**, 301 (1998).

[13] S. V. Konovalikhin, G. V. Shiiov, O. A. D'yachenko, M. Z. Aldoshina, R. N. Lyubovskaya, and R. B. Lyubovskii, Russian Chemical Bulletin **41**, 1819 (1992).

[14] R. S. Manna, M. de Souza, A. Brühl, J. A. Schlueter, and M. Lang, Physical Review Letters **104**, 016403 (2010).

[15] H. O. Jeschke, M. de Souza, R. Valentí, R. S. Manna, M. Lang, and J. A. Schlueter, Physical Review B **85**, 035125 (2012).

[16] J. A. Schlueter, L. Wiehl, H. Park, M. de Souza, M. Lang, H.-J. Koo, M.-H. Whangbo, Journal of American Physical Society **132**, 16308 (2010).

[17] M. Lang, R. S. Manna, M. De Souza, A. Brühl, J. A. Schlueter, Physica B: Condensed Matter **405**, S182 (2010).

[18] M. Lang, M. de Souza, A. Brühl, C. Strack, B. Wolf, J. A. Schlueter, J. Müller, D. Schweitzer, Physica C: Superconductivity and its Applications **460**, 129 (2007).

[19] R. S. Manna, M. de Souza, J. A. Schlueter, M. Lang, Physica Status Solidi C **9**, 1180 (2012).

Participation in scientific events

- Frontiers of Quantum Matter Workshop - Rio de Janeiro, RJ - Brazil (2013);
- I2CAM/FAPERJ Spring School - New Perspectives in Quantum Matter - Rio de Janeiro, RJ - Brazil (2013);
- XXXVII National Meeting of Solid State Physics - Costa do Sauípe, BA - Brazil (2014);
- XIV Brazilian Electronic Structure School - Fortaleza, CE - Brazil (2015);
- School of Magnetism and Superconductivity, UNICAMP - Campinas, SP - Brazil (2015);
- Summer School of Physics - UFF - Niterói, RJ - Brazil (2016);
- Experimental School of Physics - UFRJ - Rio de Janeiro, RJ - Brazil (2016);
- Mag Lab User Summer School - NHMFL - Tallahassee, FL - USA (2017);
- XL National Meeting of Solid State Physics - Búzios, RJ - Brazil (2017).
- School of Physics - UFF - Niterói, RJ - Brazil (2017).

Awards, Grants & Honours

- Best poster award at the XXXVII National Meeting of Solid State Physics in the section "Strongly Correlated Systems" with the poster entitled "*Investigation of the physical properties of the binary alloy* $FeSe_{1-x}$", Brazilian Physical Society (2014);
- Best poster award at the XIV Brazilian Electronic Structure School with the poster entitled "*A Comparative Study of the Various Phases of* $FeSe_{1-x}$", Brazilian Physical Society (2014);
- ICAM (Institute for Complex Adaptive Matter) Sponsored QuantEmX Scientist Exchange Award - National High Magnetic Field Laboratory - Tallahassee, FL - USA (2017);
- Best poster award at the XL National Meeting of Solid State Physics in the section "Metal-Insulator and Other Correlated Phase Transitions" with the poster entitled "*Investigation of the Charge-Ordered Phase in Molecular Conductors*", Brazilian Physical Society (2017);
- Best oral presentation award with the presentation entitled "Investigation of the Mott-Hubbard Phase in Molecular Conductors" at the School of Physics with − UFF − Niterói, RJ − Brazil.

Teaching activities (Tutor)

- Physics I (FSI2181) - First and second terms of 2013 (UNESP scholarship);
- Physics I (FSI2181) - First and second terms of 2014 (UNESP scholarship);
- General Physics II (FSI2107) - First term of 2016 (voluntary);
- Advanced Physics II Laboratory (FSI2190) - Second term of 2016 (M. Sc. scholarship);
- General Physics II (FSI2107) - First term of 2017 (voluntary);
- General Physics II (FSI1982) - Second term of 2017 (voluntary).

Publications

- M. de Souza, L. Squillante, C. Sônego, P. Menegasso, P. F.-Leylekian, J.-P. Pouget, Physical Review B **97**, 045122 (2018);
- Ciência Hoje Magazine - "*A ordem que emerge da desordem*" (accepted);
- Unesp Ciência Magazine - "*120 anos da partícula que é a 'onda' da ciência*" (published).

Fundamental literature

- Patrik Fazekas, Lecture Notes on Electron Correlation and Magnetism (1999);
- R. J. Baxter, Exactly Solved Models in Statistical Mechanics (1982);
- R. K. Pathria, Statistical Mechanics (1996);
- John R. Reitz, Frederick J. Milford, Robert W. Christy, Fundaments of the Electromagnetic Theory (1982);
- Charles Kittel, Introduction to Solid State Physics - eighth edition (2005);
- Neil W. Ashcroft, N. David Mermin, Solid State Physics (1976);
- M. E. Lines, A. M. Glass, Principles and Applications of Ferroelectrics and Related Materials (1977);
- Stephen Blundell, Magnetism in Condensed Matter (2001);
- Wolfgang Nolting, Anupuru Ramakanth, Quantum Theory of Magnetism (2009);
- Kerson Huang, Statistical Mechanics (1963).

Acknowledgements

I would like to acknowledge my advisor Prof. Dr. Mariano de Souza for supporting me since my undergraduate studies in Physics, for always believing in my scientific potential and for making one of my biggest dreams come true: leaving the country for the first time in order to study Physics. I have no words to describe how all the discussions and his support were important to me. I have no doubts his advising played a crucial role in my scientific career. I would like to acknowledge for all the philosophical discussions and the emotional support, which I consider to be unique and crucial. Yet, I would want to mention that I never met anyone with the sensibility, character and his World vision in my entire life, and I feel very honored to be his student.

It is always important to discuss Physics daily in order to increasingly learn. So, I would especially like to thank Prof. Dr. Ricardo Paupitz B. dos Santos for the Physics discussions, the recommendation letters and for providing me the opportunity to learn *ab initio* DFT calculations in his laboratory, having the huge patience to teach me all the basic concepts and making himself available practically 24/7. I would like to express my enormous gratitude to Prof. Dr. Roberto E. Lagos Mônaco for all the humorous Physics discussions, the countless recommendation letters for the schools of Physics and Ph. D. applications and for all the huge support since I was an undergraduate student. I would like also to specially thanks Prof. Dr. Francisco José dos Santos for all the support and for kindly providing full access to his laboratory in order to perform the solid state synthesis of this Master Thesis.

This Master Thesis would not be the same without the support from my friends from our Solid State Physics laboratory group (Paulo Menegasso, Adriano Roman, Cesar Sônego, Renan Andrade, Gabriel Gomes, Carlos Cassani and Isys Mello). Special thanks to Cesar Augusto Sônego for always being extremely helpful and supporting me all the time in the experiments, writing and as a friend. Special thanks also to Adriano Roman, which helped me study and understand meticulously several Physics topics from this Master Thesis and provided me with several pieces of advice in order to make this work even better.

I cannot forget to acknowledge my girlfriend and best friend Úrsula Virgínia Pereira, for taking my dreams as hers and supporting me in all the nights I was awake studying and for coming with me to the laboratory several times for company and support. It makes a huge difference to love and be loved in a period of intense studies and writings. I am very grateful for having her by my side.

I would like to acknowledge my mother Lindalva Gomes and my sister Isis Gomes Marques for supporting me hugely in this period and always believing in me and in my dreams. Special thanks to my mother Lindalva Gomes, which always supported me and provided me with the best education a mother could. If it weren't for her signing me in English classes when I was a kid, I wouldn't be writing this Master Thesis in English.

Special thanks also to the great friends life gave me: Fábio Carneiro, André Ferrazzo, Felipe Teodoro, Paulo Galvão and Carlos Aleixo, which, directly or indirectly, contributed to this Master Thesis and supported me in the development of all my dreams.

Probing the ionic dielectric constant contribution in the ferroelectric phase of the Fabre salts

Mariano de Souza,[1,*] Lucas Squillante,[1] Cesar Sônego,[1] Paulo Menegasso,[1] Pascale Foury-Leylekian,[2] and Jean-Paul Pouget[2]
[1]*São Paulo State University (UNESP), IGCE, Departamento de Física, Rio Claro, SP, Brazil*
[2]*Laboratoire de Physique des Solides, CNRS UMR 8502, Univers. Paris Sud, Université Paris Saclay, Orsay, France*

(Received 15 June 2017; revised manuscript received 21 November 2017; published 16 January 2018)

In strongly correlated organic materials it has been pointed out that charge ordering could also achieve electronic ferroelectricity at the same critical temperature T_{co}. A prototype of such phenomenon are the quasi-one-dimensional $(TMTTF)_2X$ Fabre salts. However, the stabilization of a long-range ferroelectric ground state below T_{co} requires the break of inversion symmetry, which should be accompanied by a lattice deformation. In this paper we investigate the role of the monovalent counteranion X in such mechanism. For this purpose, we measured the quasistatic dielectric constant along the c^*-axis direction, where layers formed by donors and anions alternate. Our findings show that the ionic charge contribution is three orders of magnitude lower than the intrastack electronic response. The c^* dielectric constant (ϵ'_{c^*}) probes directly the charge response of the monovalent anion X, since the anion mobility in the structure should help to stabilize the ferroelectric ground state. Furthermore, our ϵ'_{c^*} measurements show that the dielectric response is thermally broaden below T_{co} if the ferroelectric transition occurs in the temperature range where the anion movement begin to freeze in their methyl groups cavity. In the extreme case of the PF_6-H_{12} salt, where T_{co} occurs at the freezing point, a relaxor-type ferroelectricity is observed. Also, because of the slow kinetics of the anion sublattice, global hysteresis effects and reduction of the charge response upon successive cycling are observed. In this context, we propose that anions control the order-disorder or relaxation character of the ferroelectric transition of the Fabre salts. Yet, our results show that x-ray irradiation damages change the well-defined ferroelectric response of the AsF_6 pristine salt into a relaxor.

DOI: 10.1103/PhysRevB.97.045122

I. INTRODUCTION

Currently, there is a considerable interest both for fundamental and application purposes in the study of electronic systems exhibiting strong electron-electron interactions. Electronic correlations lead to subtle interplay between charge, lattice, and spin degrees of freedom, whose most illustrative examples can be found among organic metals [1]. As a consequence, the phase diagram of such organic metals exhibits a subtle competition between spin or charge modulated ground states and superconductivity [1–3]. Among the various charge modulated ground states, a ferroelectric phase has been recently discovered in several families of organic materials [4–6]. This discovery has boosted the study of ferroelectric materials because the origin of ferroelectricity in the organics is basically electronic [7–9], in contrast to the ionic origin in conventional ferroelectric systems studied for decades.

Among the organic materials a special attention has been devoted to the Fabre salts $(TMTTF)_2X$, whose structure is shown in Fig. 1 and where electronic ferroelectricity has been first observed [10] (TMTTF is tetramethyltetrathiafulvalene and X a monovalent counteranion such as PF_6, AsF_6, and SbF_6). Fabre salts are composed of well decoupled donor stacks sizeably dimerized in regard of the anions (see Fig. 1) [11]. In these one-dimensional (1D) electronic systems, ferroelectricity follows a 1D charge-ordering (CO) transition, revealed by the detection of a charge disproportion ($\pm\delta$) between successive donors in the stack direction [12,13], occurring at the same temperature as the dielectric constant diverges (below it is noted the common critical temperature T_{co}). Both phenomena are driven by electronic correlation effects, which are particularly enhanced in the 1D quarter-filled organic materials built with the TMTTF donor molecule [14–16]. As the TMTTF stack is made of TMTTF dimers (outlined in Figs. 1 and 2), the charge disproportion breaks all the inversion symmetry of the stack, which bears an electronic polarization [P_{el} in Fig. 2(a)]. Since at T_{co} all the stack polarizations are in phase, the material should be a ferroelectric. The detection of a strong dielectric response at T_{co}, when the electric field is applied along the stack direction a, $\epsilon'_a \sim 10^5$–10^6 in the regime of low frequencies [17,18] is taken as a good indication that ferroelectricity comes primarily from the electronic subsystem [8,9]. Note that the CO/ferroelectric transition breaks also the symmetry of the magnetic degrees of freedom forming localized $S = 1/2$ magnetic chains [19].

However, since the first detection of a conductivity anomaly at T_{co} [20], it is found that T_{co} strongly depends upon the nature of the anion X (from ~60 K, 100 K, and 155 K for $X = PF_6$, AsF_6, and SbF_6 salts, respectively). This clearly indicates that structural effects has to be incorporated in the CO/ferroelectricity mechanism (for a recent review see, e.g., Ref. [21]). Also by their easy shift from the inversion centers of the methyl group cavities, anion degrees of freedom are an important ingredient to choose and to stabilize the 3D long-range order formed below T_{co} [8,9]. Such assertion

*mariano@rc.unesp.br

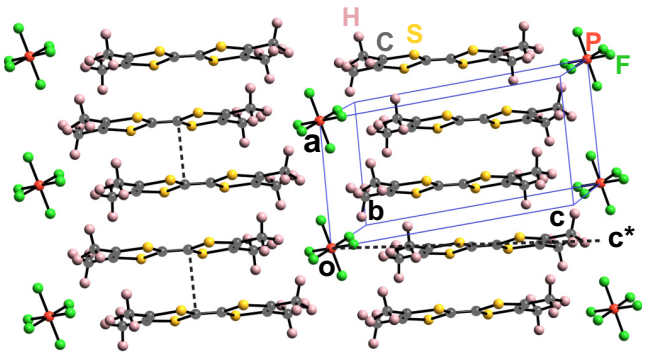

FIG. 1. Projection of the structure of $(TMTTF)_2X$ with octahedral counter-anion X in the (a, c) plane. Donors and anions alternate along the c^* direction perpendicular to a. Dimers are indicated by the dotted vertical segments in the left stack. Details in the main text.

was recently verified by various spectroscopic investigations showing a strengthened interaction of the anion SbF_6 [22] and AsF_6 [23] with the hole-rich donor molecule TMTTF below T_{co}. Nevertheless, evidence for a lattice deformation below T_{co} was only recently obtained by neutron [24] and x-ray diffraction [25] studies of deuterated and hydrogenated $(TMTTF)_2PF_6$ (labeled PF_6-D_{12} and PF_6-H_{12} hereafter, respectively). In particular, the x-ray study was able to prove the break of inversion symmetry, to determine the amount of charge disproportion between donors and to reveal asymmetric

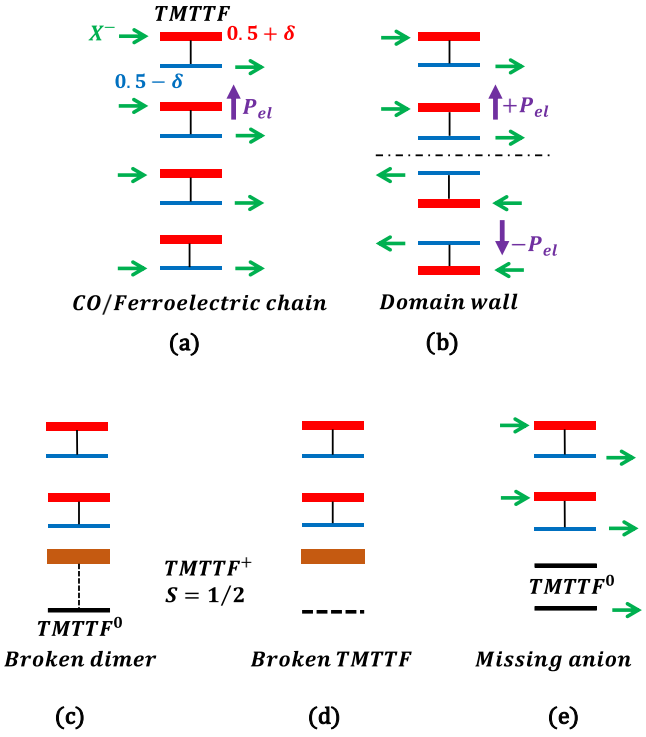

FIG. 2. Scheme of the CO/ferroelectric of (a) the TMTTF chain and (b)–(e) its various types of disorder. Green arrows represent the anion shift and the vertical black segments the dimer. Charge-rich (poor) donors are in red (blue). $TMTTF^+$ is in brown, $TMTTF^0$ is in black, and the horizontal black dotted segment represents a broken TMTTF.

interactions between anions and methyl groups of charge-rich and charge-poor donors [schematically represented by green arrows in Fig. 2(a)].

The pertinence of anion translation and rotation degrees of freedom is assessed by uniaxial lattice thermal expansion measurements exhibiting a sizable singularity at T_{co}, which is more particularly revealed for measurements performed along the interlayer c^* direction [3,26] (defined in Fig. 1). The counteranions should also control the kinetic of the transition and lead, if T_{co} is low enough, to an incomplete ferroelectric order exhibiting the typical charge response of a relaxor, as observed for the PF_6-H_{12} [27]. The frequency dependence of the longitudinal dielectric constant ϵ'_a exhibits a smoothing of its divergence together with a shift of its maximum above T_{co} when the frequency of measurement is increased, proving that the pretransitional dynamics has an intrinsic relaxation character [5]. Also, as expected for a typical order-disorder transition, there is a slowing down of the mean-relaxation time at the ferroelectric transition T_{co} [18]. In this work, we provide evidence that the anion sublattice is responsible for such behavior. In this framework the order-disorder-type transition can be simply rationalized if it is assumed that each anion is localized in a double-well potential where each minima corresponds to the anion position to form H bonds with its methyl group environment [21]. In presence of such a potential kinetics and dynamics are controlled by the ability of the anion to thermally overcome the double-well potential barrier height in order to change its direction of displacement. Also, anions should be also an intrinsic source of disorder limiting the long-range development of ferroelectricity, which should give rise to a relaxor dielectric response if T_{co} is low enough.

In order to complete previous dielectric measurements performed along the stack direction a, we present the first measurements of the dielectric constant (ϵ'_{c^*}) in the transverse inter-layer c^* direction, which is also the direction of contact between anions and the methyl groups of donors. Furthermore, our 1 kHz low-frequency measurements allows to probe the quasistatic dielectric constant. Thus, ϵ'_{c^*} measurements allow to investigate directly the charge response of the monovalent counteranions at the difference of ϵ'_a measurements, which should mix electronic and ionic contributions. In addition, we have investigated the effect of controlled disorder on the dielectric charge response by investigating well-characterized [28,29] x-ray irradiated samples.

II. EXPERIMENTAL ASPECTS

Single crystals of pristine hydrogenated Fabre salts with the monovalent anions $X = PF_6$, AsF_6 and SbF_6 were recently synthesized by Moradpour in the Laboratoire de Physique des Solides (Orsay) employing the standard procedure. Such samples are from the same batches as those investigated in the electron spin resonance (ESR) of Ref. [28]. The 97.5% deuterated Fabre salts with $X = PF_6$ have been also synthesized in Orsay according to the procedure described in Ref. [30]. They are of the same batch as those investigated in the microwave dielectric and ESR studies of Refs. [28,30], respectively. The samples have a needlelike shape with typical dimensions of $(2\times1\times0.5)$ mm^3 respectively along the a, b' [perpendicular to the a axis in the (a,b) layer] and c^* directions.

Two samples of AsF_6-H_{12}, three samples of SbF_6-H_{12}, and PF_6-H_{12} and one sample of PF_6-D_{12} were measured. One 12 h and one three days irradiated AsF_6-H_{12} samples corresponding to the ones probed by ESR in Ref. [28] were also studied.

The x-ray irradiation procedure and the determination of the number of irradiation defects by counting the number of localized spin $S = 1/2$ [see Figs. 2(c) and 2(d)] created as a function of the irradiation time are given in Ref. [29]. Following the notation used in Ref. [29], the number of irradiation defects is expressed in % of localized spin $S = 1/2$ per mole of TMTTF, a quantity denoted mol% of irradiation defects. The calibration performed in Ref. [29] indicates that the 12 h irradiated AsF_6 sample contains 0.035 mol% defect, while the three days irradiated AsF_6 sample contains 0.2 mol% defect.

In order to perform dielectric measurement along the c^* axis, the (a, b) surfaces of each single crystal were covered with carbon paste supplied by SPI supplies. Tempered gold wires provided by Cryogenic with 0.02 mm diameter were attached on the surface of the single crystals already covered with carbon paste.

The capacitance C of the investigated single crystals was then measured along the c^* axis using the standard two-points probe method employing an Andeen-Hagerling 2550 A capacitance bridge with resolution of 10^{-6} pF, operating in the fixed frequency of 1 kHz. The quasistatic dielectric constant ϵ' could be determined by employing the parallel plates capacitor textbook expression, namely $\epsilon = Cd/A$, where C is the capacitance of the sample, A is the capacitor's plates area and d is the distance between them. Hence, the dimensionless dielectric constant $\epsilon' = \epsilon/\epsilon_0$ was obtained, where ϵ_0 is the vacuum permittivity. A Teslatron-PT cryostat supplied by Oxford Instruments was employed in all experiments in the Solid State Physics Lab (Rio Claro).

Before dielectric measurements, the samples were characterized by conductivity measurements along the c^* axis. The c^* resistivity is found to be activated over the whole temperature range. Its thermal dependence, as well as the magnitude of the c^* resistivity, agrees with previous c^* dc resistivity measurements reported in Ref. [31].

Dielectric constant measurements were performed both upon warming and cooling with a temperature rate variation between ± 6 and ± 12 K/h and with an applied electric field between 50 and 150 mV/cm. Note that our 1 kHz dielectric measurements provide a good estimate of the quasistatic dielectric constant.

III. RESULTS AND ANALYSIS OF THE DATA

A. Pristine salts

Figure 3 shows the thermal dependence of the c^* dielectric constant for the SbF_6-H_{12}, AsF_6-H_{12}, PF_6-D_{12}, and PF_6-H_{12} salts measured upon cooling. For all investigated salts, ϵ'_{c^*} exhibits a well-defined peaklike anomaly at the ferroelectric transition T_{co} of the Fabre salts, as previously observed for the dielectric constant measured in the stack direction [17]. As can be directly determined from the data set shown in Fig. 3, the maximum of ϵ'_{c^*} occurs at $T_{co} = 160$ K, 105 K, 86.6 K, and 57 K for the SbF_6-H_{12}, AsF_6-H_{12}, PF_6-D_{12}, and PF_6-H_{12} salts, respectively. The T_{co} values of SbF_6-H_{12} and

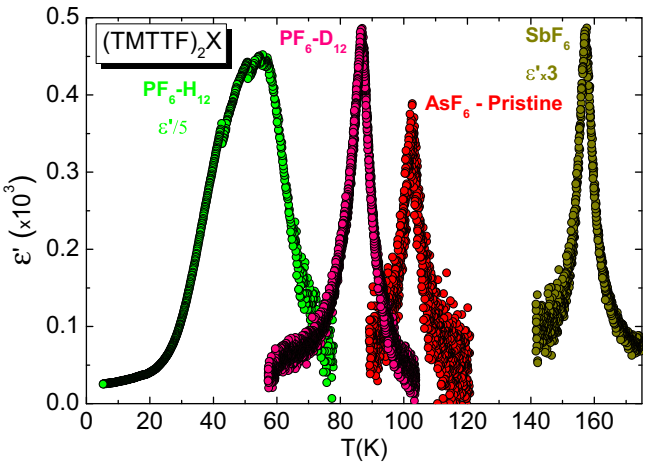

FIG. 3. Temperature dependence of the real part of the c^* dielectric constant ϵ'_{c^*} of the AsF_6-H_{12}, SbF_6-H_{12}, PF_6-D_{12}, and PF_6-H_{12} Sample No. 2 salts measured at fixed 1 kHz upon cooling. For a proper comparison between the various salts, the data for the PF_6-H_{12} was divided by a factor of 5 and the SbF_6 multiplied by a factor of 3.

AsF_6-H_{12} are in good agreement with those reported by previous dielectric constant ϵ'_a [17,18,27] and local spectroscopic measurements [12,32,33]. Also SbF_6-H_{12} T_{co} coincides with a net change of slope in the thermal dependence of the c^* resistivity measured on the same sample. The ϵ'_{c^*} dielectric measurements on PF_6-D_{12} complete an earlier microwave dielectric measurement of ϵ'_a performed in samples of the same batch [30]. The T_{co} value for the PF_6-D_{12} salt ($T_{co} = 86.6$ K) is close to $T_{co} = 84$ K obtained from microwave ϵ'_a and agrees with $T_{co} = (84 \pm 3)$ K obtained for the onset of the lattice deformation transition accompanying the CO and detected in an earlier neutron scattering investigation for PF_6-D_{12} [24]. In PF_6-D_{12} of the same batch, an enhancement of the gap of charge is detected at 85 K by ESR measurements [28]. In the PF_6-H_{12}, the maximum of ϵ'_{c^*} observed at 57 K in Fig. 3 is significantly lower than the T_{co} of 67 K reported in the literature from local measurements techniques [12,33]. Note that the thermal dependence of the 1 kHz dielectric constant ϵ'_a exhibits a maximum at ~50 K [27].

The amplitude of the maximum of ϵ'_{c^*} at T_{co} was found to be strongly sample dependent. The ϵ'_{c^*} maximum was found to be at: −50, 350, and 150 in the three SbF_6-H_{12} samples investigated, −350 and 150 in the two AsF_6-H_{12} samples investigated, −400 in the PF_6-D_{12} sample investigated.

Unlike the others salts, where a well-defined sharp peak anomaly is observed at T_{co}, a broad rounded dielectric response is observed for the PF_6-H_{12} salt. For Sample No. 2 [Fig. 4(a)] a sizable dielectric response was measured with a main peaklike response up to 2000 at ~57 K followed by two secondary peak-like responses at 40 K and 52 K before the vanishing of ϵ'_{c^*} below ~25 K. For Sample No. 1 [Fig. 4(b)] an even broader dielectric response reaching a much weaker intensity of 50 around 55 K was observed. Below its broad maximum the response continuously decreases until ~10 K. A behavior similar to the one of Sample No. 1 is exhibited by a third sample (not shown here) where ϵ'_{c^*} exhibits a broad maximum of 90. Note that a somewhat similar broad response, strongly

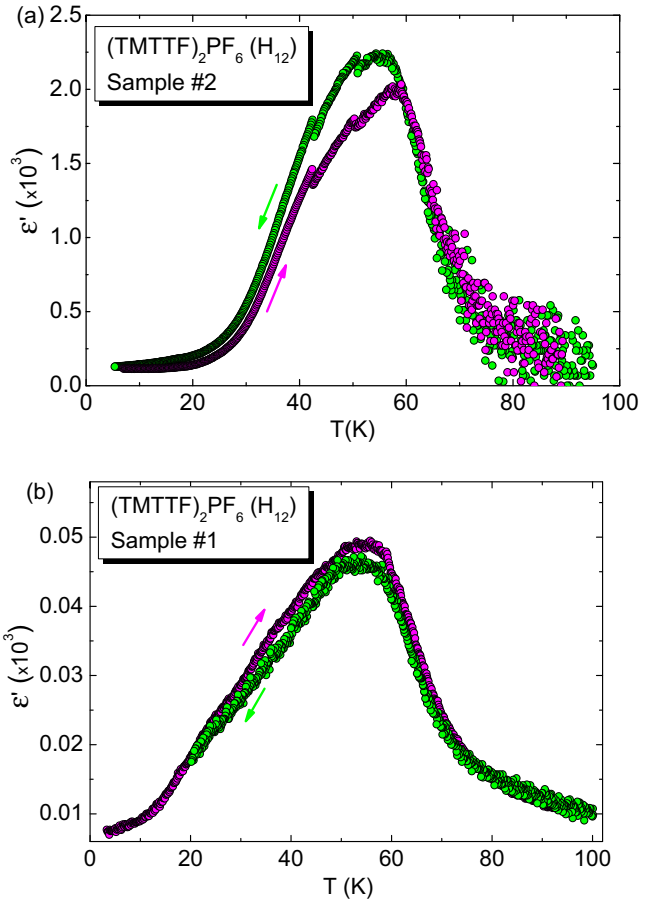

FIG. 4. (a) Dielectric constant as a function of temperature for the fully hydrogenated $(TMTTF)_2PF_6$ salt (Sample No. 2) showing a maximum dielectric response at about 57 K both in the heating and cooling processes with employed rate of ± 7 K/h and 50 mV/cm of applied electric field. Also, the various observed jumps indicate the formation of ferroelectric clusters, details in the main text. (b) Dielectric constant as a function of temperature for the fully hydrogenated $(TMTTF)_2PF_6$ salt (Sample No. 1) showing a broad maximum of dielectric response around 55 K in both heating and cooling measurements with an employed rate of ± 6 K/h and 150 mV/cm of applied electric field.

frequency dependent, is exhibited by the longitudinal dielectric constant ϵ'_a of PF_6-H_{12} investigated in Ref. [27].

Figure 4 shows also that there is a significant global hysteresis between ϵ'_{c^*} of PF_6-H_{12} measured upon heating and cooling. Also ϵ'_{c^*} decreases upon successive thermal cycling (Fig. 5).

B. Irradiated AsF_6-H_{12} salts

Figure 6 depicts the thermal dependence of ϵ'_{c^*}, normalized to T_{co} of pristine AsF_6-H_{12} and for two AsF_6-H_{12} samples irradiated for 12 h and three days. The dielectric response of the irradiated samples broadens pronouncedly in temperature and shifts to lower temperatures. A comparison between the thermal dependence of pristine and 12 h irradiated AsF_6-H_{12} show that the broadening is basically due to the enhancement of the dielectric response below T_{co}. An extreme situation occurs for the three days irradiated AsF_6-H_{12} with the growth of a

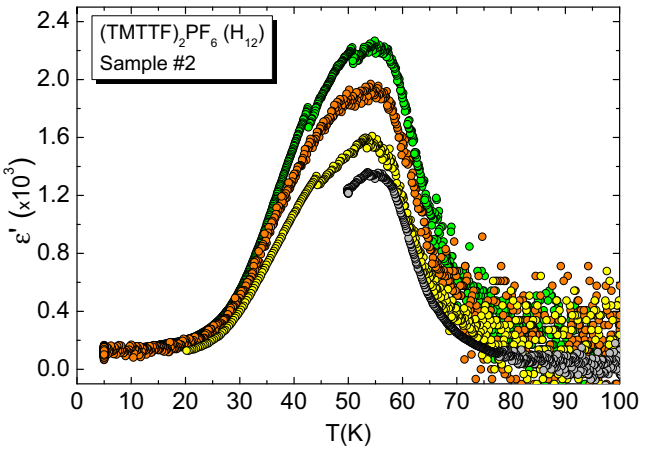

FIG. 5. Dielectric constant of PF_6-H_{12} (Sample No. 2) measured during four successive cooling runs. The green data set was measured employing a rate of -7 K/h, while for the orange, yellow and gray data sets a rate of -10 K/h was employed.

very broad and nonsymmetric dielectric response. The latter grows slowly below T_{co}, presenting a broad maxima centered at ~40 K, vanishing rapidly below 20 K.

The T_{co} peak anomaly of pristine AsF_6-H_{12} rounds and clearly shifts under irradiation. For the 12 h irradiated AsF_6-H_{12} containing 0.035 mol% defect T_{co} was shifted by ~3.7 K. This gives a 1 K shift of T_{co} for 0.01 mol% defect. The sensitivity of the CO transition to irradiation defect is similar to that found in the SbF_6 and ReO_4 salts, where a 1 K shift of T_{co} occurs between 0.017 mol% defect and 0.007 mol% defect, respectively [29].

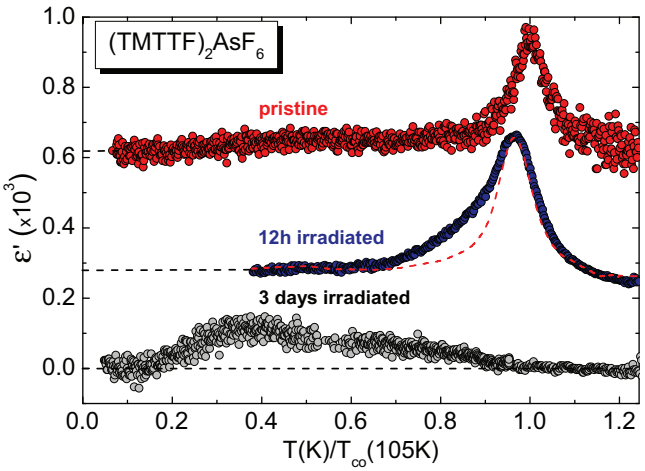

FIG. 6. Dielectric constant (ϵ') as a function of temperature for the pristine $(TMTTF)_2AsF_6$ system (red data set), 12 h irradiated (blue) and three days irradiated (gray). The red dashed line, which refers to the smooth data of the pristine variant, was multiplied by a factor of 1.4 for a proper comparison with the 12 h irradiated variant. The measurements were carried out in warming up employing a rate of $+12$ K/h and with 50 mV/cm of applied electric field. The temperature scale T/T_{co} is expressed in a fraction of the ferroelectric critical temperature of our pristine AsF_6 sample ($T_{co} = 105$ K). For clarity the data have been shifted vertically (the base line of each shifted data is indicated on the left side of the figure).

ϵ'_{c^*} measurements clearly show that irradiation damages change the well-defined peak anomaly of the 1 kHz (i.e., quasistatic) dielectric constant of the pristine salt into a typical broad one of a dielectric relaxor. However, frequency measurements were not performed in order to probe the dynamics of the dielectric response.

IV. DISCUSSION OF THE RESULTS

A. Anisotropy of the dielectric constant

All the c^* dielectric measurements presented in Sec. III show that the transverse dielectric constant ϵ'_{c^*} is lower by several orders of magnitude than the longitudinal dielectric constant ϵ'_a. This proves, as expected for a 1D electronic system, that the charge response is very anisotropic. More quantitatively, if one compares the average transverse ϵ'_{c^*} measured at 1 kHz with the longitudinal ϵ'_a measured at 10 kHz in Ref. [18] for the AsF_6-H_{12}, one obtains a $\epsilon'_a/\epsilon'_{c^*}$ ratio of 400 at T_{co}. A similar $\epsilon'_a/\epsilon'_{c^*}$ ratio of $\sim 10^3$ at T_{co} is obtained in PF_6-H_{12} from the ratio of the 1 kHz longitudinal dielectric constant of Ref. [27] to the average transverse dielectric constant. In these salts the anisotropy of ϵ' is comparable to the anisotropy of electrical conductivity between a and c^* directions at T_{co} [31].

Among the ionic species a special attention must be devoted to the anions, which are the most mobile charged constituents of the Fabre salts and thus should exhibit a strong dielectric response [5]. ^{19}F NMR probe of SbF_6-H_{12} and SbF_6-D_{12} salts shows that the anion begins to rotate in their methyl group cavity above ~75–80 K [32] and undergoes successive reorientation with thermally activated jump movements above 135 and 210 K [34]. In addition, rotation and translational degrees of freedom of the anions are taken as responsible for the negative thermal expansion of lattice parameters detected above ~100 K, this onset temperature being slightly dependent on the nature of the anion, see Refs. [3,26]. Such anomalous behavior is found to be the strongest in the c^* direction, along which the donors and anions layers alternate. Hence, dielectric measurements performed in the c^* direction should mostly probe the anion contribution at the dielectric response. The detection of a critical divergence of ϵ'_{c^*} at T_{co}, which will be more quantitatively analyzed in the next section, means that anions collectively participate at the onset of the ferroelectric ground-state. In particular, its displacement from the inversion centers of the high-temperature lattice is essential to break the inversion lattice symmetry and to stabilize the 3D electronic charge pattern below T_{co}.

Note that it is also expected, due to the isotropic nature of the anion cavity, an ionic contribution at ϵ'_a, which should be of the same order of magnitude as ϵ'_{c^*}. Nevertheless, if the ionic contribution scales with the anion mobility giving rise to the anomalous thermal dependence of the lattice expansion coefficient above ~100 K [3,26], one expects a larger ionic contribution for ϵ'_{c^*}.

B. Thermal dependence of the dielectric response

Figure 3 clearly shows that the thermal broadening of the quasistatic dielectric response ϵ'_{c^*} of the different Fabre salts increases upon decreasing T_{co}. More quantitatively, if one defines ΔT as the full-width at half-maximum temperature range of the dielectric response, one gets $\Delta T/T_{co}$ of 3%, 5.5%, and 8% for the SbF_6-H_{12}, AsF_6-H_{12}, and PF_6-D_{12} salts, respectively. Much larger $\Delta T/T_{co}$ values of 0.47 and of 0.66 are obtained for PF_6-H_{12} Samples No. 2 and No. 1, cf. Figs. 4(a) and 4(b), respectively.

Except for the PF_6-H_{12}, this systematic broadening effect is less apparent in ϵ'_a measured at higher frequency for the various Fabre salts investigated in Ref. [17]. This observation indicates that ϵ'_{c^*}, which mostly probes the anion response, is more sensitive to the structural disorder. Such observation is not surprising as the anions themselves are the source of the disorder. In order to test this assertion, the dielectric response of irradiated AsF_6-H_{12} was similarly analyzed. Figure 6 shows that their dielectric response significantly broadens upon increasing irradiation. More quantitatively, one obtains $\Delta T/T_{co}$ of 0.15 and 1.25 for AsF_6-H_{12} irradiated 12 h (0.035 mol% defect) and three days (0.2 mol% defect), respectively.

If one assumes that the $\Delta T/T_{co}$ broadening is roughly proportional to the amount of defect, one estimates that PF_6-H_{12} intrinsically contains the equivalent of ~0.1 mol% defect. This is five times larger than the estimated amount of intrinsic defects in PF_6-D_{12}, which should contain the equivalent of ~0.02 mol% defect.

The thermal divergence of ϵ'_{c^*} at T_{co} can be quantitatively analyzed by the Curie-Weiss plots of $1/\epsilon'_{c^*}$ as a function of T [Figs. 7(a) and 7(b)]. In the mean-field approximation it is predicted that in both sides of T_{co}:

$$1/\epsilon'_{c^*} = A_{\pm}|T - T_{co}|,$$

with a slope ratio A_-/A_+ of 2. The criteria employed for the Curie-Weiss analysis, depicted in Figs. 7(a) and 7(b), was to fix the right solid line, obtained from a mean-least-square fit of the raw data above T_{co}, and draw the left solid line in accordance with the slope ratio in the mean-field approximation ($A_-/A_+ = 2$), as shown in Ref. [18]. This mean-field dependence is only observed for $1/\epsilon'_{c^*}$ of the SbF_6-H_{12}. In the other Fabre salts one observes a deviation from the linear dependence below T_{co}, which increases upon going from AsF_6-H_{12}, PF_6-D_{12} to PF_6-H_{12}. In contrast, this linear behavior is found in both sides of T_{co} for $1/\epsilon'_a$ reported in Refs. [10,27] in SbF_6-H_{12}, AsF_6-H_{12}, and PF_6-H_{12}. However, a deviation of the linear dependence of $1/\epsilon'_a$ below T_{co}, similar to the one exhibited by $1/\epsilon'_{c^*}$ in Fig. 7, is found in a recent reinvestigation of ϵ'_a of AsF_6-H_{12} [18].

Figure 7 shows that the deviation from the linear dependence of $1/\epsilon'_{c^*}$ below T_{co} is dramatically enhanced in the 12 h irradiated AsF_6-H_{12} sample. Such a behavior is also visible in the ϵ'_{c^*} measurements shown in Fig. 6. Based on such observation, one can thus ascribes the deviation from the mean-field divergence of the dielectric constant to the formation of structural disorders, regardless of their origin. A similar conclusion was achieved from the study of ϵ'_a in AsF_6-H_{12} [18].

C. Sources of disorder

Figures 2(b)–2(e) give schematic illustrations of the various sources of disorder, which can be present in the Fabre salts. As a matter of fact, recent Raman scattering investigations have

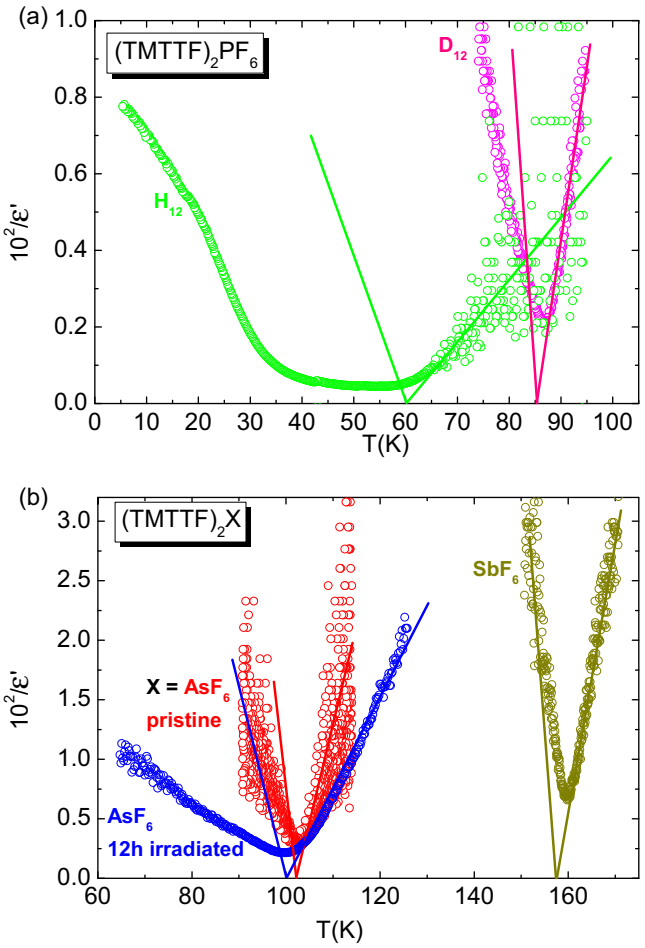

FIG. 7. Curie-Weiss plot, i.e., $1/\epsilon'$ as a function of T upon cooling for: (a) H_{12} Sample No. 2 (green) and D_{12} (pink) PF_6; (b) the pristine $(TMTTF)_2AsF_6$ system (red data set), 12 h irradiated (blue), SbF_6 (dark yellow), cf. label. The solid lines indicate the expected slopes in the frame of the mean-field approximation. The solid lines above T_{co} are obtained from a mean-square fit of the raw data for the various salts. Details in the main text.

detected ionized $TMTTF^+$ and neutral $TMTTF^0$ species in pristine SbF_6-H_{12}, AsF_6-H_{12}, and PF_6-H_{12} [35], which were assigned to ferroelectric domain walls. Since in a dimer the average charged donor is $TMTTF^{+0.5}$, neutral and ionized species indicates the existence of broken dimers [Fig. 2(c)]. It is known that the photoinduced local chemistry caused by x-ray irradiation leads to the break of both donor and anion species [29]. This also induces molecular displacements in the surroundings of a defect. The break of a donor molecule should prevent the pairing of donors into dimers, leading to the formation of $TMTTF^+$ species [Fig. 2(d)]. The break of an anion in turn will prevent the transfer of one electron from the TMTTF stack to the anion. This will provide $TMTTF^0$ species instead of two $TMTTF^{+0.5}$, which usually pair into a dimer [in Fig. 2(e) there are two $TMTTF^0$].

Another important source of disorder arises from the reversal direction of displacement of the anions. As shown in Fig. 2(b), this will interchange the position of charge-rich and charge-poor donors along the stack direction. Such interchange can be viewed as the introduction of a phase shift of π in the CO stack modulation [7]. This phase shift changes the direction of the electronic polarization, introducing a ferroelectric domain wall. As the transverse displacement of the anions fixes the longitudinal direction of the electronic polarization, and vice versa, such defects should affect both ϵ'_{c^*} and ϵ'_a.

Except for the irradiated samples, where $TMTTF^+$ and $TMTTF^0$ defects [Figs. 2(d) and 2(e)] are directly created by the x-ray irradiation local chemistry, it appears that a change of direction in the uniform anion shift should be easily achieved in the pristine Fabre salts. The presence of such defects is most likely frequent, since the anions are less mobile and begin to freeze in the methyl group cavities when the temperature is decreased. For the SbF_6-H_{12} ($T_{co} = 160$ K), the ferroelectric transition occurs in the temperature range, where the presence of mobile anions is assessed by NMR [32,34] together with a c^* negative lattice thermal expansion above $\sim$80 K [3]. Thus, SbF_6-H_{12} is not expected to exhibit important disorder effects, modifying the Curie-Weiss dependence of the dielectric constant. This is not the case for the AsF_6-H_{12} ($T_{co} = 105$ K) because the ferroelectric transition occurs when the anions just begin to freeze with the saturation of the c^* negative lattice thermal expansion regime around 125 K [3,16]. Compared to the SbF_6-H_{12} salt, a longer tail of the dielectric response develops below T_{co} in the AsF_6-H_{12} salt. A somewhat similar observation can be done for the PF_6-D_{12} salt ($T_{co} = 86.6$ K). A very drastic effect occurs in the PF_6-H_{12} salt, since T_{co} occurs below the temperature $\sim$75 K at which the anion movements freeze, according to the c^* thermal expansion measurements reported in Refs. [3,26].

The thermally broadened dielectric response of PF_6-H_{12} exhibits clear characteristics of a ferroelectric relaxor [36]. First, the dielectric response is broad and does not exhibit a clear peaklike anomaly at a well-defined T_{co}. Second, the maxima of ϵ' depends on the frequency of the measurement [27]. In the low-frequency regime, i.e., in quasistatic conditions, the maxima of ϵ'_a occurs at $\sim$50 K [27] and the maxima of ϵ'_{c^*} occurs around 55 K and 57 K for the two samples measured in Fig. 4. All the T_{co} values obtained from the maximum of ϵ' are significantly lower than $T_{co} = 67$ K obtained from local detection, i.e., from spectroscopic techniques [12,33]. Our ϵ'_{c^*} measurements show also that the charge response is sample dependent. A broad response with a low value of ϵ'_{c^*} is observed in Sample No. 1 [Fig. 4(b)], while a narrower response of a larger ϵ'_{c^*} accompanied by several secondary peaks is observed in Sample No. 2 [Fig. 4(a)]. This behavior suggests that Sample No. 2 is composed of ferroelectric clusters with different T_{co}. Third, one observe a global hysteresis between the heating and cooling curves (Fig. 4), and a reduction of ϵ'_{c^*} upon successive cycling (Fig. 5). The global hysteresis point out the presence of disorder, which pins ferroelectric domains and prevents their thermal evolution. Each cycle creates defects, which limit the extent of ferroelectric domains in the subsequent cooling processes because they are not completely resorbed after the heating cycle above T_{co}.

In agreement with the observation of a slowing down of the mean-relaxation time at T_{co} [18], it takes a long time to establish the long-range thermodynamic ferroelectric order. Thus, the slow kinetics associated with the anion displacement

process limit the ferroelectric ordering process. Then, the difficulties to achieve the long-range uniform anion shift should be taken as responsible for the fragmentation of the ferroelectric order into domains. If one assumes that PF_6-H_{12} contains 0.1 mol% defect, there is one defect every 1000 TMTTF molecules or every 500 unit cells (there are two TMTTF per unit cell). If one defect pins one ferroelectric domain, the average volume of the domain should be of (3.5×10^5) Å^3. This volume is close to the average volume of the CO domain, namely (8.7×10^5) Å^3, estimated for irradiated $(TMTTF)_2X$ [29] from the defect concentration at which the singular decay of conductivity at the CO transition vanishes. If the ferroelectric domains pinned on defects are isotropic, its average size is about 70 Å.

V. CONCLUSION

We have measured the quasistatic transverse dielectric constant of the Fabre salts allowing us to probe the ionic charge response, which is the lattice counterpart of the electronic ferroelectricity associated with the CO transition. Measurements along the c^* direction give direct access to the counteranion response, which is a key ingredient to choose and to stabilize the 3D long-range order below T_{co}. Our ϵ'_{c^*} measurements, conjugated with earlier investigations of the lattice thermal expansion, show that the dielectric response is thermally broadened below T_{co} if the transition occurs in the temperature range where the anion movement begins to freeze in the methyl group cavities. In the case of PF_6-H_{12}, where T_{co} occurs in the freezing regime, a relaxor-type ferroelectricity is observed. For the latter, because of the slow kinetics of the anion sublattice, global hysteresis effects and reduction of the charge response upon successive thermal cycling is observed. Finally, ϵ'_{c^*} measurements of x-ray irradiated AsF_6-H_{12} show that irradiations damages change the well-defined dielectric response of the pristine salts into a relaxor one. In this context, we have proposed that anions control the order-disorder or relaxation character of the ferroelectric transition of the Fabre salts.

ACKNOWLEDGMENTS

M.de-S. acknowledges financial support from the São Paulo Research Foundation–Fapesp (Fundação de Amparo à Pesquisa do Estado de São Paulo) (Grant No. 2011/22050-4), National Council of Technological and Scientific Development-CNPq (Conselho Nacional de Desenvolvimento Científico e Tecnológico) (Grant No. 305472/2014-3) and CAPES (Coordenação de Aperfeiçoamento de Pessoal de Nível Superior) for support via scholarships for L.S. and C.S.

[1] *Physics of Organic Conductors and Superconductors*, edited by A. G. Lebed, Springer Series in Materials Sciences (Springer-Verlag, Berlin, 2008), Vol. 110.
[2] M. Dressel, Naturwissenschaften **94**, 527 (2007).
[3] M. de Souza and J.-P. Pouget, J. Phys.: Condens. Matter **25**, 343201 (2013).
[4] S. Tomic and M. Dressel, Rep. Prog. Phys. **78**, 096501 (2015).
[5] P. Lunkenheimer and A. Loidl, J. Phys.: Condens. Matter **27**, 373001 (2015).
[6] S. Ishihara, J. Phys.: Condens. Matter **26**, 493201 (2014).
[7] S. Brazovskii in Ref. [1], p. 313.
[8] S. Brazovskii, J. Phys. IV France **12**, Pr9 (2002).
[9] S. Brazovskii, Synth. Metals **133–134**, 301 (2003).
[10] P. Monceau, F. Y. Nad, and S. Brazovskii, Phys. Rev. Lett. **86**, 4080 (2001).
[11] J.-P. Pouget and S. Ravy, J. Phys. I France **6**, 1501 (1996).
[12] D. S. Chow, F. Zamborszky, B. Alavi, D. J. Tantillo, A. Baur, C. A. Merlic, and S. E. Brown, Phys. Rev. Lett. **85**, 1698 (2000).
[13] M. Dumm, B. Salameh, M. Abaker, L. K. Montgomery, and M. Dressel, J. Phys. IV (France) **114**, 57 (2004).
[14] C. Bourbonnais and D. Jérome in Ref. [1], p. 357.
[15] J.-P. Pouget, Physica B **407**, 1762 (2012).
[16] J.-P. Pouget, Physica B **460**, 45 (2015).
[17] F. Nad and P. Monceau, J. Phys. Soc. Jpn. **75**, 051005 (2006).
[18] D. Starešinić, K. Biljaković, P. Lunkenheimer, and A. Loidl, Solid State Commun. **137**, 241 (2006).
[19] S. Yasin, B. Salameh, E. Rose, M. Dumm, H.-A. Krug von Nidda, A. Loidl, M. Ozerov, G. Untereiner, L. Montgomery, and M. Dressel, Phys. Rev. B **85**, 144428 (2012).
[20] R. Laversanne, C. Coulon, B. Gallois, J. P. Pouget, and R. Moret, J. Phys. (Paris) Lett. **45**, L393 (1984).
[21] J.-P. Pouget, Crystals **2**, 466 (2012).
[22] K. Medjanik, M. de Souza, D. Kutnyakhov, A. Gloskovskii, J. Muller, M. Lang, J.-P. Pouget, P. Foury-Leylekian, A. Moradpour, H.-J. Elmers *et al.*, Eur. Phys. J. B **87**, 256 (2014).
[23] K. Medjanik, A. Chernenkaya, S. A. Nepijko, G. Ohrwall, P. Foury-Leylekian, P. Alemany, E. Canadell, G. Schonhense, and J.-P. Pouget, Phys. Chem. Chem. Phys. **17**, 19202 (2015).
[24] P. Foury-Leylekian, S. Petit, G. Andre, A. Moradpour, and J.-P. Pouget, Physica B **405**, S95 (2010).
[25] S. Kitou, T. Fujii, T. Kawamoto, N. Katayama, S. Maki, E. Nishibori, K. Sugimoto, M. Takata, T. Nakamura, and H. Sawa, Phys. Rev. Lett. **119**, 065701 (2017).
[26] M. de Souza, P. Foury-Leylekian, A. Moradpour, J.-P. Pouget, and M. Lang, Phys. Rev. Lett. **101**, 216403 (2008).
[27] F. Nad, P. Monceau, C. Carcel, and J. M. Fabre, Phys. Rev. B **62**, 1753 (2000).
[28] C. Coulon, G. Lalet, J.-P. Pouget, P. Foury-Leylekian, A. Moradpour, and J. M. Fabre, Phys. Rev. B **76**, 085126 (2007).
[29] C. Coulon, P. Foury-Leylekian, J. M. Fabre, and J.-P. Pouget, Eur. Phys. J. B **88**, 85 (2015).
[30] A. Langlois, M. Poirier, C. Bourbonnais, P. Foury-Leylekian, A. Moradpour, and J.-P. Pouget, Phys. Rev. B **81**, 125101 (2010).
[31] B. Köhler, E. Rose, M. Dumm, G. Untereiner, and M. Dressel, Phys. Rev. B **84**, 035124 (2011).
[32] W. Yu, F. Zhang, F. Zamborszky, B. Alavi, A. Baur, C. A. Merlic, and S. E. Brown, Phys. Rev. B **70**, 121101(R) (2004).
[33] M. Dressel, M. Dumm, T. Knoblauch, and M. Masino, Crystals **2**, 528 (2012).
[34] K. Furukawa, T. Hara, and T. Nakamura, J. Phys. Soc. Jpn. **74**, 3288 (2005).
[35] R. Świetlik, B. Barszcz, A. Pustogow, and M. Dressel, Phys. Rev. B **95**, 085205 (2017).
[36] G. A. Samara, J. Phys.: Condens. Matter **15**, R367 (2003).